Multi-Port RF MEMS Switches and Switch Matrices

by

Mojgan Daneshmand

A thesis
presented to the University of Waterloo
in fulfillment of the
thesis requirement for the degree of
Doctor of Philosophy
in
Electrical and Computer Engineering

Waterloo, Ontario, Canada, 2006

I hereby declare that I am the sole author of this thesis. This is a true copy of the thesis, including any required final revisions, as accepted by my examiners.

I understand that my thesis may be made electronically available to the public.

Abstract

Microwave switch matrices are essential components in satellite payloads. These matrices enhance satellite capacity by providing full and flexible interconnectivity between the received and transmitted signals and facilitate optimum utilization of system bandwidth. Waveguide and semiconductor technology are two prominent candidates for realizing such types of switch matrices. Waveguide switches are dominant in high frequency applications (100 – 200 GHz) and in high power satellite communication. However, their heavy and bulky profile reinforces the need for a replacement. While, semiconductor switches are miniature alternatives to mechanical waveguide switches, they exhibit poor RF performance and low power handling.

RF MEMS technology is a good candidate to replace the conventional switches. The technology has a great potential to offer highly miniature switches with superior RF performance. Over the past five years, numerous research studies have been devoted to develop RF MEMS switches. However, they are mostly concentrated on Single-Pole Single-Throw (SPST) configurations and a very limited work has been reported on multi-port switches and switch matrices. Hence, the focus of this thesis is on the development of multi-port RF MEMS switches and switch matrices. To explore the topic, three development tasks are considered: planar (2D) multi-port RF MEMS switches, three dimensional (3D) multi-port RF MEMS switches, and RF MEMS switch matrix integration.

One key objective of this thesis is to investigate novel configurations for planar multi-port (SPNT), C-type, and R-type switches. Such switches represent the basic building blocks of switch matrices operating at microwave frequencies. Theoretical and experimental results are presented for the proposed novel multi-port switch configurations. In addition, an in house monolithic fabrication process dedicated to electrostatic multi-port RF MEMS switches is developed and fine tuned.

For the first time, a new category of 3D RF MEMS switches is introduced to the RF MEMS community. These switches are not only extremely useful for high power applications but also have a great potential for millimetre-wave applications (30GHz -100GHz). The idea is based on the integration of vertically actuated MEMS actuators inside 3D transmission lines such as waveguides and coaxial lines. SPST and C-type switches based on the integration of rotary thermal and electrostatic actuators are designed and realized. The concept is experimentally verified for frequencies up to 30GHz. A high power test analysis and measurement data indicates no major change in RF performance as high as 13W.

The monolithic integration of the RF MEMS switch matrix involves the design and optimization of a unique interconnect network which is amenable to the MEMS fabrication process. While the switches and interconnect lines are fabricated on the front side, taking advantage of the back side patterning provides a high isolation for cross over junctions. Two different techniques are adopted to optimize the interconnect network. They are based on vertical three-via interconnects and electromagnetically coupled junctions. The measured results demonstrate that the monolithic switch matrix exhibits an isolation of better than 40dB up to 30GHz. This technique not only eliminates the need for expensive multilayer manufacturing process such as Low Temperature Co-fired Ceramics (LTCC) but also provides a unique approach to fabricate the entire switch matrix monolithically.

Acknowledgment

I wish to express my sincere appreciation and gratefulness to my advisor Professor Raafat R. Mansour for his knowledge, insight, valuable guidance, and continuous encouragement throughout this research. He is always there when I need help. Indeed, my gratitude to him can not be expressed in a few words and it is my honor to be his student.

I would like also to thank Professor G. Rebeiz, Professor P. Nieva, Professor S. Chaudhuri, and Professor S. S. Safavi-Naeini for serving on my committee and for their constructive criticisms and suggestions in the preparation of the final report.

Financial support during this study was provided by the Natural Science and Engineering Research Council of Canada (NSERC) and COMDEV. Their contribution is greatly appreciated.

Many thanks to CIRFE group members for their invaluable support and help especially during the last year of my study. I am really indebted to Roger Grant and Stella Chang who taught me how to work in the clean room and be patient, to Bill Jolley who spent hours on the assembly of my switches, to Tania Ooagarah who made long hours of working in the clean room feel short and enjoyable, to Louise Green who was there when ever I had mixed up with my paper works, and to Winter Yan and Rui Zhang with their friendly smiles even though my telephone calls would distract them several time in a row.

Extended thanks go to my Mom and Dad for their support, patience, and sacrifice during my education life. They taught me how to start with A,B,C and finish with a Ph.D dissertation. I will never forget their endless support and kindness. Last but not the least, a world of thanks goes to my friend and coleague, my love and my husband, Pedram Mousavi. I am really grateful to his collaboration, enthusiasm and support. Without his hopeful vision on the down days of my research and encouragements on the up days, this work would be far from completion. I would also like to welcome to my daughter Daria

who truly wanted to be present at my defense day. She made this day one of the most pleasant days of my life. This work is dedicated to them.

Table of Contents:

List of Figures

List of Tables

Chapter 1

Introduction

1.1. Motivation

Currently, the common microwave switches employed in the satellite communication are mechanical switches (coaxial and waveguide) and semiconductor switches (PIN diode and FET). Mechanical coaxial and waveguide switches offer the benefits of low insertion loss, large off-state isolation, and high power handling capabilities. However, they are bulky, heavy, and slow. On the other hand, semiconductor switches such as PIN diodes and FETs provide a much faster switching speed and are smaller in size and weight; however, they are inferior in insertion loss, DC power consumption, isolation, and power handling capabilities than their mechanical counterparts. MEMS switches promise to combine the advantageous properties of both mechanical and semiconductor switches. They offer the high RF performance and low DC power consumption of mechanical switches but with small size, weight and low cost features of semiconductor switches.

There are two principle applications which reflect the opposite extremes of the switch market. First, there is the satellite application which requires the use of large switch matrices that demand the highest switching performance. Secondly, there are wireless handheld phones and Bluetooth applications that employ low cost individual semiconductor switches. Over the past five years, most of the research efforts reported in

the literature have been directed toward the development of a Single-Pole Single-Throw (SPST) switch for wireless applications. The SPST switch is a two-port device, which acts as a simple RF relay.

In satellite systems, switches are typically used in the form of switch matrices either for redundancy or for signal routing. The basic building block of such matrices can be Single-Port N-throw (SPNT), C- type switches or R-Type switches. These switches are multi-port devices with a much more complicated function than simple SPST switches. In spite of many applications of switch matrices, very limited work has been reported on this topic.

1.2. Objectives

The purpose of this thesis is to present unique configurations and techniques to develop novel RF MEMS multi-port switches and switch matrices. Thin film MEMS process is adopted to fabricate the structures either monolithically or in hybrid form. The subject is divided into three tasks:

i) **Development of novel configurations for planar (2D) multi port (SPNT), C-Type and R-Type MEMS Switches:** Such switches represent the basic building blocks of switch matrices operating at microwave frequencies. Monolithic fabrication as well as the hybrid integration of this type of switches is studied and experimented.

ii) **Introducing a new category of three dimensional (3D) multi-port RF MEMS switches**: SPST, SP2T, and C-type switch configurations based on integrating MEMS actuators in waveguide and coaxial waveguides are explored and the results are detailed. These switches are capable of handling high power levels and promise to be useful in millimetre-wave frequencies.

iii) **RF MEMS Switch Matrix Integration**: An interconnect network amenable to MEMS technology is developed and monolithically integrated with multi-port RF MEMS switches to construct a switch matrix on a single chip.

1.3. Structure of the Thesis

The motivation and the research objectives are outlined in this chapter. A review of existing switches, including mechanical and solid state switches as well as MEMS switches are addressed in Chapter 2. In addition, a brief review of high density interconnect lines is presented.

In Chapter 3, several novel planar multi-port RF MEMS switches are reported. The list includes SP2T, SP3T, C-type and R-type switches. The monolithic and hybrid fabrication of the structures, along with measured data, are presented.

A new category of 3D MEMS switches are introduced to the MEMS community in Chapter 4. Theoretical and measured results ar presented for SPST and C-type MEMS-based waveguide and coaxial switches.

Chapter 5 deals with the development efforts of monolithic RF MEMS switch matrix. Novel types of low cost interconnect networks that are compatible with the thin film MEMS fabrication processes, are proposed. Details of the matrix integration are also given.

Chapter 6 summarizes the contributions of the thesis and proposes some related problems for future research.

.

Chapter 2

Background Information

This chapter provides a brief review of RF switches, switch matrices, and their applications. Different types of conventional switches that are currently used in RF and microwave applications are first introduced. Then, a more detailed survey of existing RF MEMS switches and high density interconnect networks follow.

2.1. Conventional RF and Microwave Switches

Telecommunication involves a broad range of frequencies from below HF up to millimeter-waves. Along with varying operating frequency requirements, the switch specifications can also differ. There are many factors that must be considered in evaluating RF switches. Insertion loss and isolation are two critical parameters since they directly affect the overall RF performance of the system. Also, the DC power consumption of the switches is a key factor in system considerations particularly in space applications where the DC power requirement is one of the main design drivers. Advanced MEMS switches can be designed with no DC power consumption. Switch cost may not be the driving factor in satellite applications but it becomes the most important factor in other applications such as cell phones or Bluetooth. Another important design consideration is the RF power handling capability in both the ON and OFF states. In the following sections, conventional mechanical and semiconductor switches are reviewed and their limitations in view of the above design considerations are deliberated.

2.1.1. Mechanical RF Switches

Mechanical switching is achieved through a break in the transmission line or electrical path by a control signal activating an electromagnetic relay. These moving parts provide the ON and OFF states.

Figure 2.1 (a) depicts a waveguide mechanical switch from Advance Switch Technology [3]. By the rotation of the waveguide, the switch moves from its normal position and shifts the connection between the ports. These switches offer the benefits of a low insertion loss 0.05dB, a large OFF state isolation (70dB) and capability of handling high power up to 3.5 KW average power at about 10GHz.

A coaxial switch is also shown in Figure 2.1 (b) along with the switch's typical fail-safe mechanical operation. The switch employs an electromagnet for the actuation to move the arm, and a spring to pull it back to the initial position. Such a switch is consistently in the normal position until the application of the current to the coil actuates it. When the power is removed from the coil, the switch returns to the normal position.

Typically, these switches have good RF characteristics: i.e. a 60dB isolation, and a 0.5dB insertion loss at 10GHz [4]. Due to this fact, they have been used in applications with large number of elements such as matrix configurations, as shown in Figure 2.2, [5]-[6].

Although mechanical switches exhibit excellent RF characteristics, they have a very slow switching speed, typically 2 to 50ms [7]. The switches are also heavy and bulky and require new solution especially in satellite communications where mass reduction is a major issue.

(a)

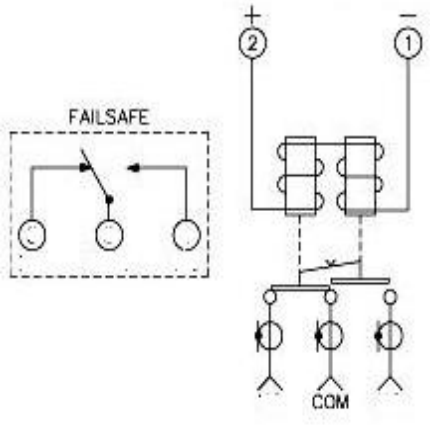

(b)

Figure 2.1: Mechanical Switches (a) waveguide switch [3] and (b) coaxial switch and its schematic [4].

Figure 2.2: Various coaxial switch matrices.

2.1.2. Solid State Switches

Typically, semiconductor PIN and FET switches are suitable for high speed switching applications. Such switches have a much faster switching speed and are smaller in size and weight but they are inferior in insertion loss, DC power consumption, isolation and power handling capabilities compared to their mechanical counterparts. Several efforts have been made to improve the performance and enhance the isolation [8].

As indicated in Figure 2.3, PIN diodes can be implemented with respect to the transmission direction and configured as switches. The circuit can be also embedded in microstrip lines. The signal passes through the line if the PIN diode is forward biased. It leads to low impedance (ON) and so that the signal flows from the input to the output. When the diode is reverse biased (OFF), it is in a high impedance state, causing the input signal to be reflected.

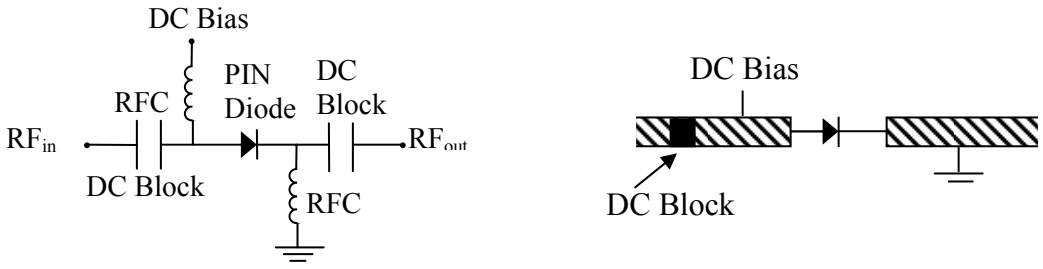

Figure 2.3: Configuration of series PIN diode switch (a) circuit and (b)mounted on microstrip transmission line [7].

The FET switch is a three-terminal device with the gate voltage acting as the control signal, as represented in Figure 2.4. The low and high impedance states required for switching applications are obtained by making the gate voltage equal to zero and greater than the pinch off voltage, respectively.

These circuits can be fabricated in a hybrid integrated circuit configuration or monolithically in MMIC circuits. In hybrid microwave integrated circuits, the active and lumped components are connected to distributed circuits by wire bonding or soldering

which also adds some loss to the switch. In MMICs, however, both active and passive components are fabricated simultaneously on a semiconductor substrate such as GaAs. MMIC's major advantage is that they can be manufactured in high volume. Due to this fact, MMIC switches have been widely used in large number applications such as switch matrices [9], as shown in Figure 2.5.

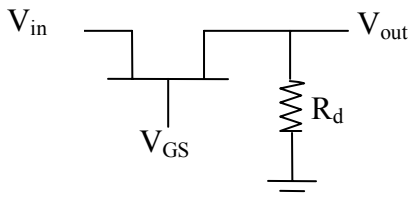

Figure 2.4: Typical configuration of FET switching circuit [7].

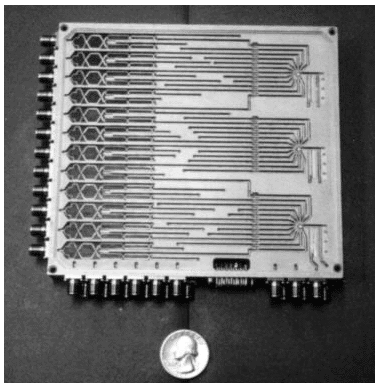

Figure 2.5: Solid state switch matrix configuration.

For signal frequencies higher than 1 GHz, these solid state switches exhibit a large insertion loss in the ON state (typically 1 to 2dB), and a poor isolation in the OFF state (-20dB) [7]. The limitations of mechanical switches and solid state technology have motivated the new research for solutions, particularly RF MEMS switches. The MEMS technology provides the possibility of replacing many of the microwave switches in today's mobile, communication, and satellite systems.

2.2. RF MEMS Switch Principle

MEMS switches are promising to combine the advantageous properties of both mechanical and semiconductor switches. MEMS switches offer the high RF performance and low DC power consumption of mechanical switches with the small size, low weight and inexpensive cost features of semiconductor switches, as summarized in Table 2.1. Most MEMS switches are actuated by electrostatic forces leading to near zero power consumption, since there is no current flow. In addition, MEMS switches use air gaps for the OFF state resulting in excellent isolation and have very low insertion loss. Based on the RF characteristics of these switches, Figure Of Merit (FOM) is introduced as "ON state resistance× OFF state capacitance", demonstrating the superior performance of MEMS over that of semiconductor switches. Moreover, they are very linear devices that result in very low inter-modulation products.

Table 2.1 : RF MEMS vs. FET, PIN, and mechanical switch comparison.

	FET	PIN	Mechanical	MEMS
FOM (10^{-15} Sec.)	270	110	0.073	2.5
DC Power	≈ 0	10 mW	≈ 0	≈ 0
IP3 (dBm)	40-50	30-45	80-90	65-80
Isolation	Low	Medium	High	High
Size (mm^2)	Small	Small	Large	Small

These switches are fabricated by using surface micromachining technology and consist of sputtered or evaporated thin metal films and silicon nitride or dioxide to create cantilever and membrane configurations. They can be built on quartz, Pyrex, Low-temperature Co-fired Ceramic (LTCC), mechanical-grade high resistivity silicon or GaAs substrates [10].

However, RF MEMS switches do have their problems. RF MEMS Switches have

relatively low speed of approximately 2 to 40μs whereas certain communication devices require much faster switches. Since MEMS switches cannot tolerate more than 20-50mW, their power handling is another issue. The electrostatic movement of the mechanical parts requires a high voltage of approximately 20 to 200 Volts for consistent operation which is well above the required voltage of other solid state technologies. In addition, packaging issues and their costs should be added to the list.

Recently, various kinds of MEMS switches have been extensively studied in series and shunt structures [10]-[11] and additional methods of electrostatic actuation have been introduced [12]. In next section, a short survey of cantilever beam and fixed-fixed membrane switches is given.

2.2.1. RF Switches Based on Cantilever Beams

A number of efforts have been reported on the development of cantilever beam switches [13]-[15]. A simple schematic of such a switch is drawn in Figure 2.6. The beam is anchored to the substrate and is pulled down by the use of a DC electrode underneath. In the ON state, the beam makes a metal- metal contact with the RF line.

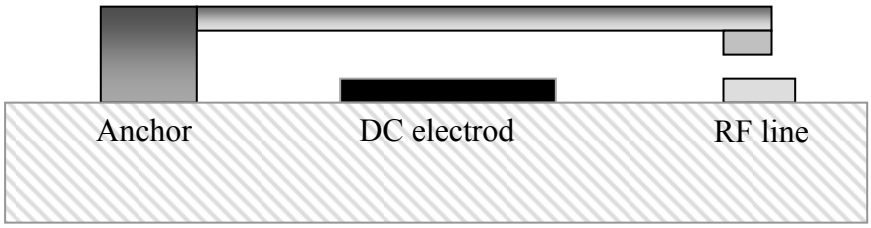

Figure 2.6: Side view of the typical cantilever beam RF switch

In this type of structure, even in the absence of an applied voltage, the cantilever beam deviates from the horizontal position due to high residual stresses in the metal and dielectrics. This can be controlled by the process development and temperature control of the switch itself under the operating conditions [14].

In 1991, the Hughes research laboratory reported the fabrication of a new CPW micro-machined switch [13]. It is similar in principle to the aforementioned silicon micro-machined structure with a substrate of GaAs and a conductor of gold to render it appropriate for RF applications. A schematic of this switch is offered in Figure 2.7. The switch's actuation is achieved electrostatically, and its pull down capacitor is incorporated into the transmission line. The structure is composed of a CPW port at the input, a middle portion which supports the microstrip mode, and a CPW line at the output port. The results confirm a good isolation and an insertion loss up to 40 GHz with an initial actuation voltage between 80-100 volts [13]

In another design, shown in Figure 2.8, a separation of the DC electrode from the RF electrode is considered [16]. In this switch, the electrostatic force between the bottom electrode and the metal pad on the beam causes the actuation. The metal pad is mounted

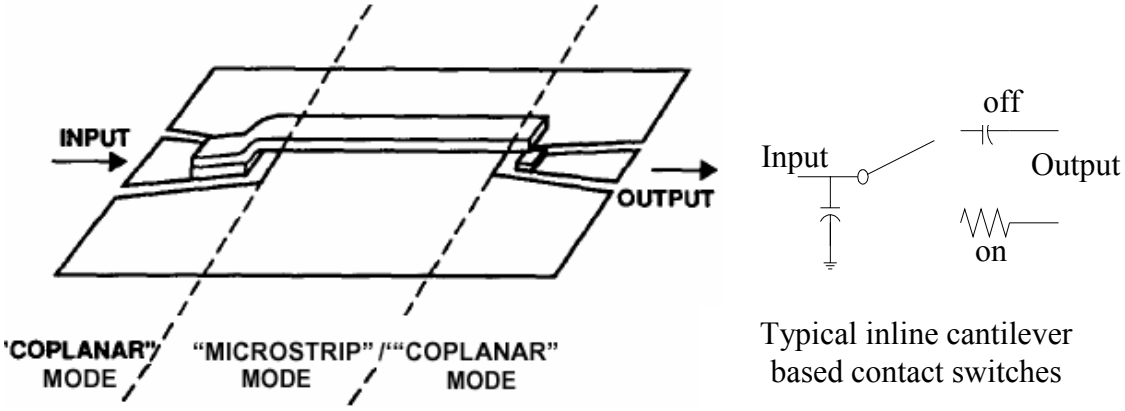

Figure 2.7 : Microwave micro-machined switch with pull down capacitance is incorporated into transmission line [13].

at the center of the dielectric cantilever with another conductor part at the far end of the beam to provide the RF contact. In the switch down state, the beam creates continuity by bridging the gap in the RF transmission line. RF measurement shows that the insertion loss increases very gradually with the increased frequency and grows up to approximately 0.25dB at 40GHz with an isolation of 20 dB.

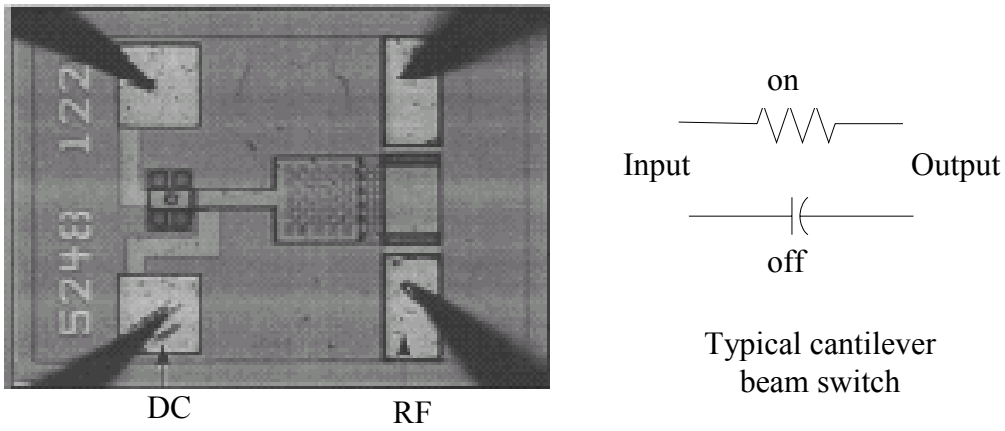

Figure 2.8: Micrograph of the SPST switch developed at Hughes Research Laboratory [16]

In addition to the metal to metal contact for the RF link, some switches operates based on capacitive coupling. In [15] a corrugated cantilever arm is used to design a metal to metal contact as well as capacitive coupling link. Figure 2.9 denotes the structure of the corrugated beam. This switch is relatively small (55μm by 45μm) and the pull-down electrode is in the RF path directly beneath the cantilever. To minimize the parasitic effects of the pull-down electrode it is constructed from a high sheet resistivity metal. Figure 2.9(a) illustrates the DC contact switch which has platinum pads to make the connection while in part (b) the RF links through the capacitive coupling between the beam and the RF pad. In order to achieve a satisfactory coupling, the area of the capacitor between the beam and the RF pad increases resulting in a longer beams (200μm by 148 μm). A 150nm thick silicon dioxide is deposited to make the parallel plate capacitor.

In the OFF-state, this switch curls up creating a relatively large separation distance of approximately 10-15 μm, which results in a high isolation and at the same time creates an increase in the pull-in voltage. It has been reported that about 80Volts is required for a good contact resistance whereas the primary actuation voltage is around 35V. However, the RF performance of this switch is not as good as that of the previously reported structures [15].

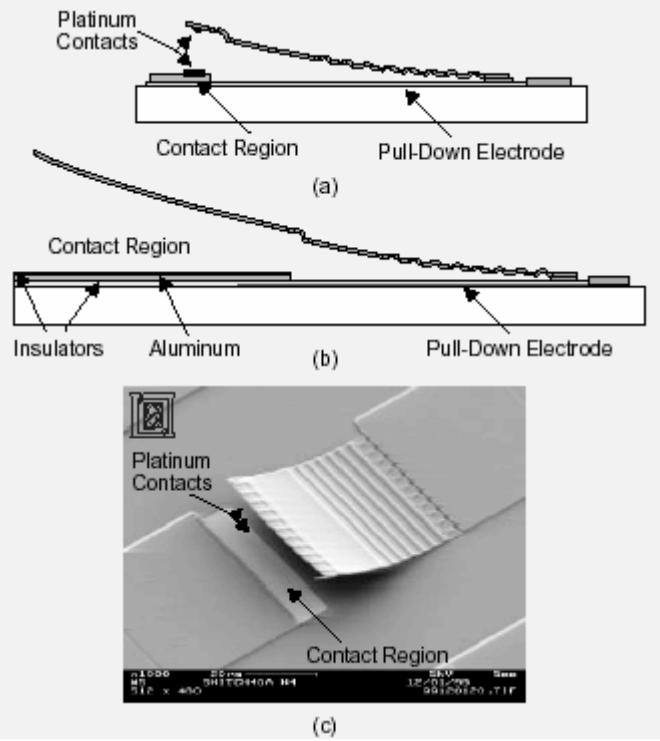

Figure 2.9 : *(a) SEM of Lincoln Laboratories in-line MEMS-series switch in a metal-metal contact, (b) capacitive configuration and (c) SEM of the metal-metal contact switch [10].*

In an overall view, cantilever beams are suitable for RF MEMS integrated structures, since the beams have the capability of being used in-line or broadside. In the latter, the actuation occurs in a plane that is perpendicular to the transmission line while in the former, the actuation occurs on the same plane as the transmission line. The main difference between the two designs is that the RF signal will pass by the entire in-line switch. In both cases, when the DC voltage is applied the switch turns ON identifing them as series type switches.

2.2.2. RF Switches Based on Fixed-Fixed Membrane

In this type of switch, a doubly-supported membrane is used as signified in Figure 2.10. Two approaches are explored for switching the RF line ON and OFF with such a membrane, series and shunt. In the first approach, the deformable beam realizes a segment of the transmission line carrying signal. When no voltage is applied, the beam is un_deflected which leads to an open line. When there is an actuation voltage, the beam deflects and closes the existing gap from the RF line. For shunt switches, the principle is based on capacitive coupling. There is a thin dielectric film on the RF

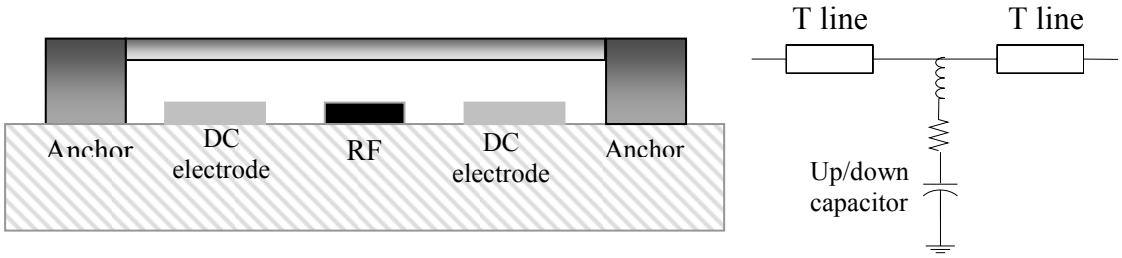

Figure 2.10: Typical fixed-fixed membrane switch structure

signal line that prevents them from making a metal contact. The air gap is electrostatically adjusted to achieve a capacitance change between the up and down states. In contrast to the series switches, applying DC voltage pulls the electrode down and turns the ON switch OFF.

2.2.2.1. Series Fixed-Fixed Membrane Switches

Extensive investigations have been performed on this type of switch, especially in the last couple of years [17]-[21]. In all the designs, the reduction of the actuating voltage and the improvement in the insertion loss and isolation of the switch were the primary goals.

Milanovic has published a paper on the batch transferring of the integration of an RF micro-relay on a quartz substrate [21]. In the fabrication, the MEMS design is

performed on the Si substrate and the microwave design is completed on the quartz. When the release process is performed, the structures remain on the chip due to the small gold bump staples. Then by using a flip chip bonder after a careful alignment the membrane is transferred to the substrate. The fabrication process is detailed in Figure 2.11. The RF measurement of this structure shows an isolation of 20dB up to 30GHz and insertion loss of 0.4 dB. According to this paper, the pull down voltage range is between 25V and 110V. This large variation is believed to be due to the variation in the height of the structures in the flip chip transfer from one chip to another.

Another type of fixed-fixed membrane switch, which is produced by the Rockwell Science Center (RSC) [19], is shown in Figure 2.12. The device is 250μm by 250μm with the suspended structure sitting a few microns above the substrate plane. This micro-relay is fabricated by surface micromachining. There are two small contact points with dimensions of $3\mu m^2$ on either contact area. The small contact points are needed to reduce the metal-to-metal stiction and to increase the contact pressure. It is a metal contact relay, with electrical isolation between signal and drive lines, that leads to a good insertion loss in the ON state of the switch. An insertion loss of 0.4 dB and an isolation of -25dB, are reported for the frequencies from DC to 40GHz. The electrostatic actuation of the switch occurs at about 70V and a low resistance can be achieved by a voltage that is 20% higher i.e. 85V.

The reliability and reproducibility of this switch has been also examined. According to [21], lifetime characteristic of the switch has been measured for several samples and the best devices show lifetime of higher than tens of millions cycle. Its reproducibility has also been tested across multiple fields of a wafer. The results show 15% actuation voltage variability and 90% of electrical yield defined by $|S_{21}| < 0.3$ dB at 2GHz.

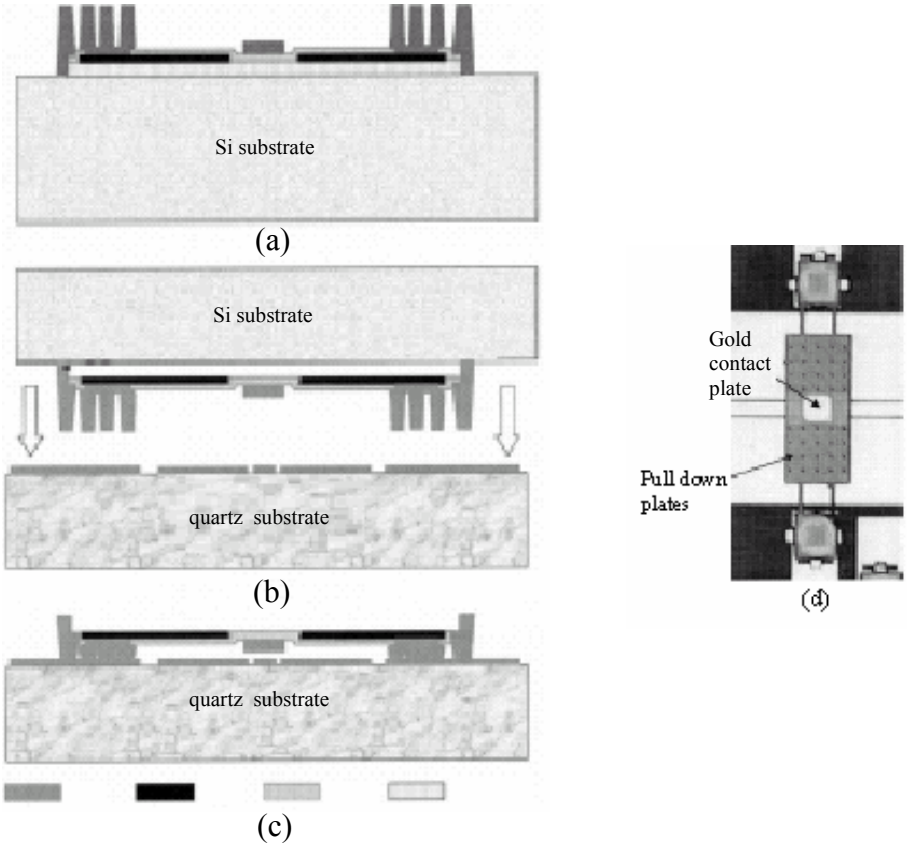

Figure 2.11: Schematics of the fabrication of (a) the structure before release and transfer, (b)the structure after release, flipped and aligned for transfer onto the substrate, (c) final transferred structure and (d) top view of the switch [21].

2.2.2.2.Shunt Fixed-Fixed Membrane Switches

In 1996, the first practical capacitive shunt switch was presented by Raytheon [10], as shown in Figure 2.13. It is based on a fixed-fixed metal beam design. The membrane is anchored to the coplanar ground plane with a height of 1.5 to 4μm and results in a pull

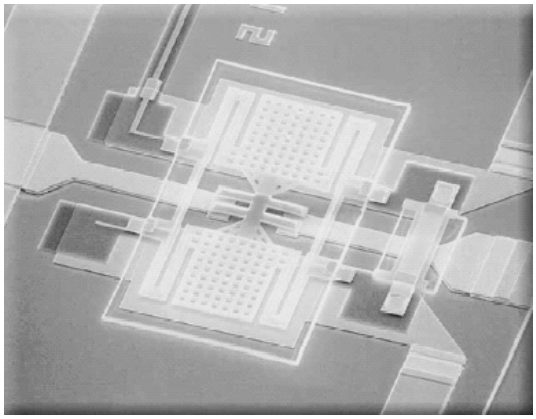

Figure 2.12(a) RCS MEMS switch [10]

down voltage of 10 to 60 volts. The switch's central electrode provides both the electrostatic actuation and the RF capacitance between the transmission line and the switch membrane. When the switch is in the up state, it provides a low capacitance of about 25 to 75fF and does not affect the signal. In the downstate though, the capacitance becomes 1.2-3.6pF and this results in a good short circuit. Since then, numerous studies have been conducted on capacitive shunt switches to achieve better performance and lower actuation voltage [23]-[26].

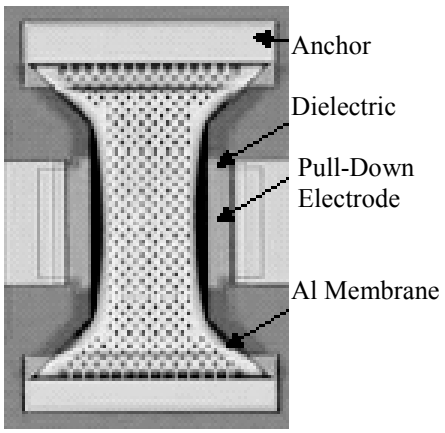

Figure 2.13: Raytheon MEMS capacitive shunt switch structure [10].

To reduce the actuating voltage, two different capacitive switches have been investigated at the University of Michigan (Figure 2.14). For the first switch, the membrane is composed of a 0.8μm thick gold layer with a height of 1.7-2.2 μm, which results in a pull down voltage of 25 to 30V. The second switch is based on a low spring constant membrane. This results in a pull-down voltage of 8 to 15V and at the same time a relatively slow switching time. These types of low spring constant switches are more efficient when pull0-up electrodes can be used. This is due to the fact that the restoring forces are low for such designs and extra pull up force is required when the membrane is down.

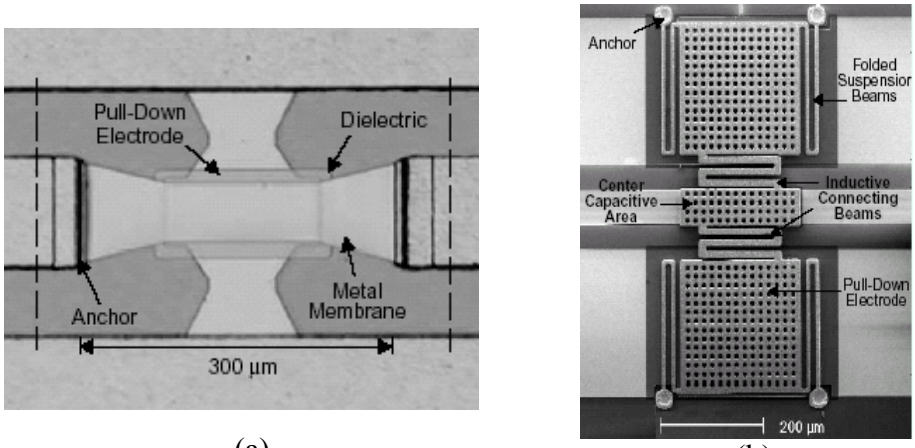

(a) (b)

Figure 2.14 : University of Michigan (a) low height MEMS switch, and (b) low spring-constant

In general, the limiting mechanism in capacitive switches is the charging of the dielectric layer between the electrode and the signal line within the switch structure. In the contact switches, the mechanism that limits the lifetime is the degradation of the ohmic contacts with repeated actuations [33].

Comparing the fixed-fixed beams and cantilever beam structures, the former is more flexible in expanding the electrodes area and possessing a larger actuating

capacitor. Whereas, the cantilever beam switches require a lower activation voltage than the fixed-fixed beam switches with the same length [14].

2.2.3. Electro-Thermal Switches

Electro-thermal switches are a well known type of actuation mechanism where high contact force is required. Up to now, a considerable amount of research has been dedicated to SPST switches.

Buckled beam thermal actuators, represented in Figure 2.15, have been used as RF MEMS switches [27]-[29]. This switch has exhibited a simulated ON state insertion loss of 1dB and an OFF state isolation of 19dB at 2GHz. To reduce the DC power consumption of the thermal actuators, bi-stable actuators have been employed. Figure 2.16 is an example of a bi-stable electro-thermal RF switch which can be operated with zero standby power in either latched states [28]. The device includes a bi-stable structure which electrically shorts the input and output signal lines. Two electro-thermal actuators are used to switch it ON and OFF. The measurement result indicates that at 3.5 GHz, the switch offers a 0.5dB insertion loss and -30dB isolation.

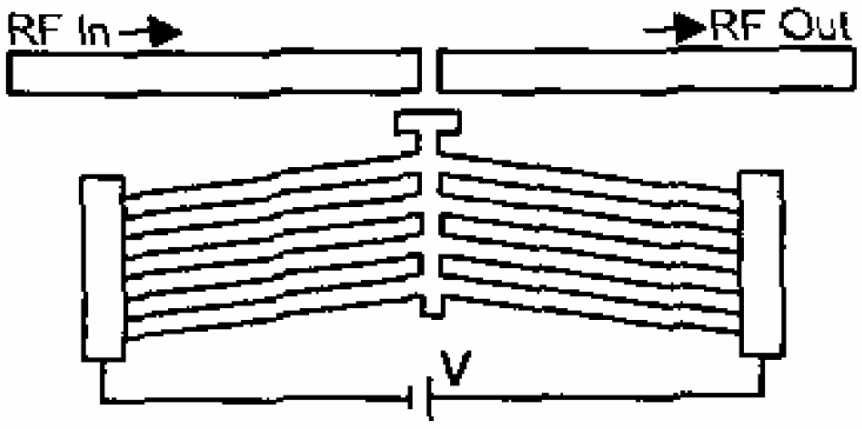

Figure 2.15: Buckled-actuators RF MEMS switch [27].

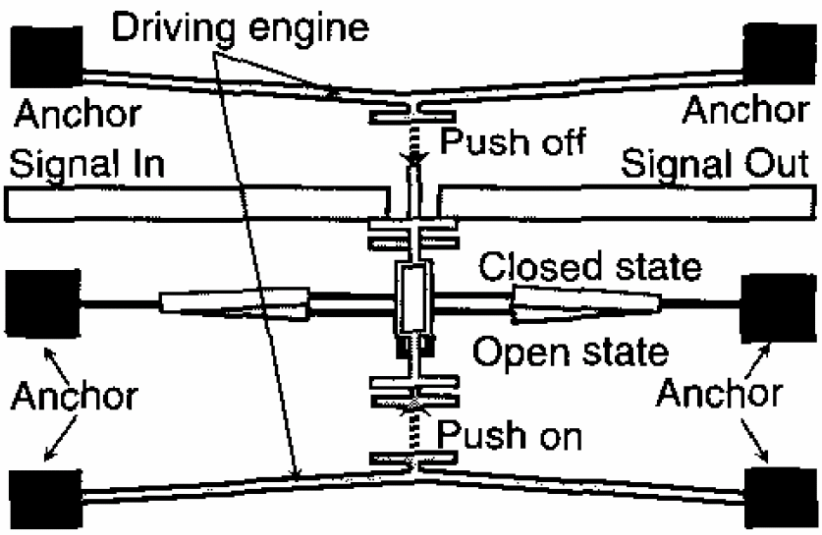

Figure 2.16: Schematic illustration of the bi-stable switch [28].

2.3. Multi-Port RF MEMS Switches

Although there are many reports on SPST RF MEMS switches, but limited research has been conducted on multi-port structures. Possibly, this is due to the complexity of the RF design, as well as the increased number of the actuating mechanisims.

LAAS-CNRS (France) have recently presented the SP2T CPW switch in Figure 2.17 [29] based on capacitive shunt membranes. The switch is very narrow band and lossy i.e 28GHz to 33GHz for a 2 dB insertion loss and 20dB isolation. Another SPDT has been presented by the School of EECS at Seoul National University as shown in Figure 2.18. This switch is based on a direct contact with a clamped-clamped membrane. The design includes a quarter-wave short stub to match the circuit. This limits the bandwidth to 40 to 45GHz for a return loss of 20dB and an isolation of 20dB. The only reported SP3T switch is from Sanida National Laboratory and is based on metal contacting switches [31]. The results are claimed to be a 29dB isolation and 0.3dB loss at 19GHz. unfortunately, to our knowledge, no more data has been published.

Another reported multi-port switch is a Single-Port Four-Throw (SP4T) from the University of Michigan/ Rockwell Science Center [22]. This switch is based on four of contact-shunt SPST Rockwell switches that have been integrated by the University of Michigan, as depicted in Figure 2.19. Recently, a wideband performance of this switch has been presented in [32]. This switch is also very limited in bandwidth i.e. up to 7GHz for a -20dB return loss. The presented data from multi-port switches highlights the need to develop wideband multi-port switches.

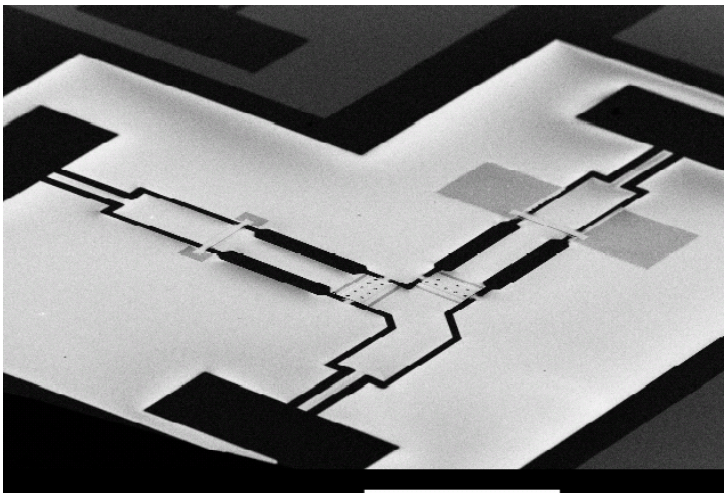

Figure 2.17: LAAS-CNRS (France) SP2T capacitive switch [29].

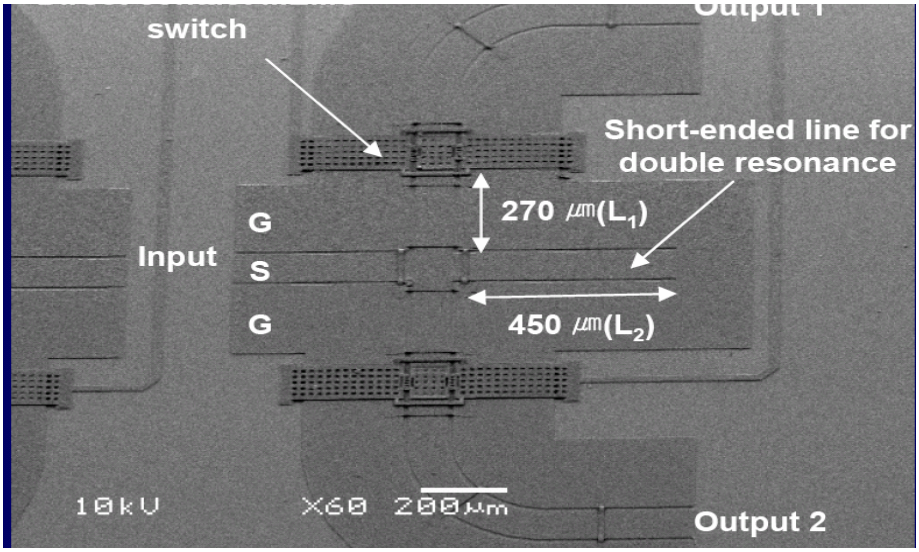

Figure 2.18: SPDT switch presented by the School of EECE Seoul National University

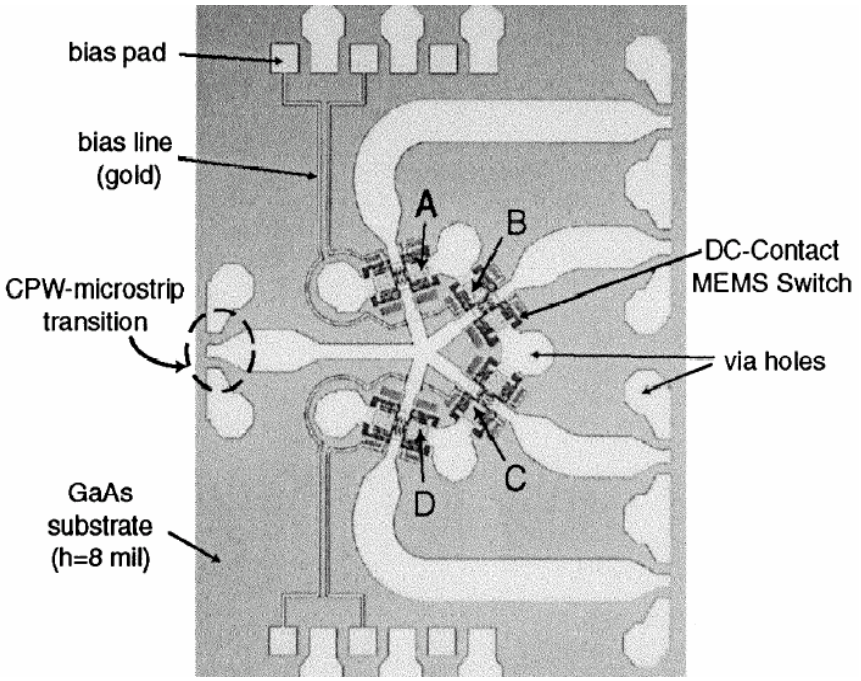

Figure 2.19: Single-Pole Four-Throw (SP4T) Rockwell/Michigan switch[22].

2.4. High Density Interconnects

Key component of the switch matrices is their interconnect network. Due to the downscaling of the switches, smaller and denser interconnect lines and multi layer structures are required. However, miniaturization causes several difficulties including parasitic capacitors and unwanted crosstalk between the lines. Additionally, moving from one layer to another through highly inductive vias adds some excess loading to the lines. These aspects subjects are addressed next.

2.4.1. Coupling and Crosstalk

When transmission lines are printed in high density configurations, minimizing the interactions between the adjacent circuits becomes extremely important. These interactions, known as crosstalk, can be caused by substrate modes in large electrical areas or parasitic coupling capacitances due to close proximities [34].

Several investigations have been conducted on coupling between the lines [35]-[38]. Figure 2.20 reflects the effect of the spacing between the lines on the cross coupling [39]. Although higher pitch values result in lower coupling, it is not always possible to avoid. Additionally, it leads to a larger circuit and increases the cost. The application of finite and separate ground planes in adjacent lines has been suggested to improve the isolation [34]. In 1996, Ishikawa and Yamashita [37] characterized a guided wave structure buried microstrip line. Half shielded lines are employed to reduce the isolation up to -100dB. However, the suggested configuration is not a planar structure and needs special fabrication process.

Also, a wide-band bridge or overpass has been used for cross over lines as shown in Figure 2.21, [40]. The design consists of a 25 μm air bridge formed on the intersection of two CPW lines printed on one layer. The grounds are separated to reduce the coupling to -35dB up to 50GHz.

Realizing transmission lines sandwiched by ground planes on multi-layer substrates can be a good solution to improve the isolation. However, there are still unsolved fabrication problems. For instance, (LTCC) which is the finest current technology for high frequency applications needs essential modification of ideal condition for the buried ground plane. This is implemented by meshed configuration and attributed mainly to the ceramic fabrication technology as the metallized area should be less than 50%. This causes unwanted coupling that has been characterized and modeled in [35]. It has been reported about -40dB at 4GHz for two parallel micorstip lines.

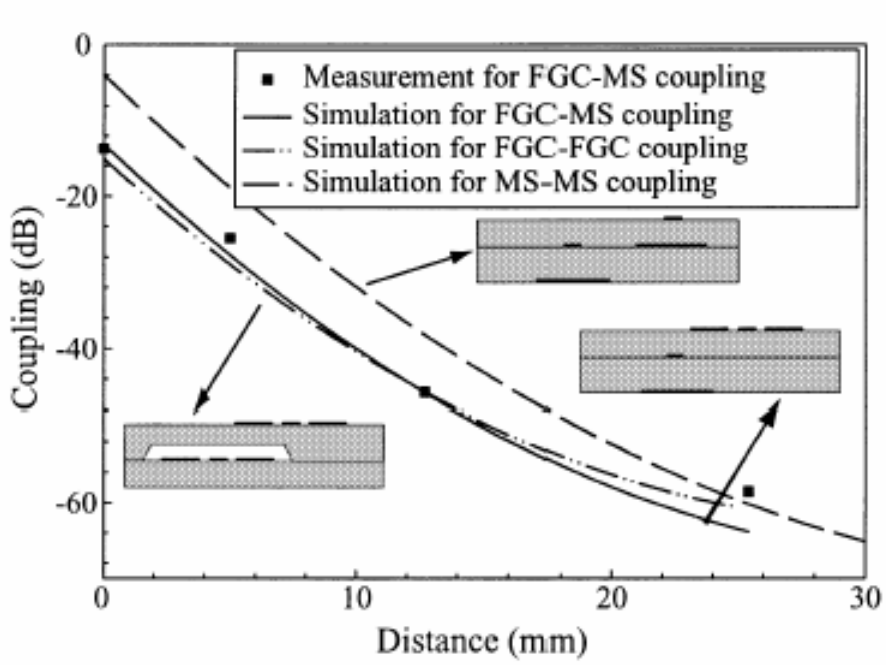

Figure 2.20: X-band measured and numerical results for vertically separated finite ground CPW and microstrip lines showing coupling versus centre to centre spacing [39].

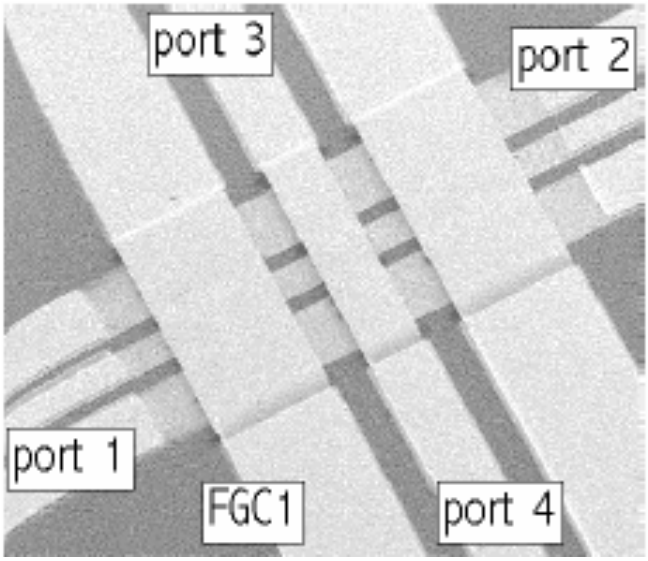

Figure 2.21: SEM micrograph of finite ground coplanar waveguide crossover junction. Both lines have the same dimensions [40].

2.4.2.Conductive Interlayer Connection

To provide a conductive connection between two different layers of a substrate, vias can be used whereas the connection between two different substrates can be achieved by flip chip bumps.

Figure 2.22 shows a transmission line terminated to a via followed by upper level lines. In such configurations, the inductive loading effect of the via on the signal line leads to severe mismatching and unwanted coupling [41]. This becomes one of the significant performance limiting factors, particularly at millimeter-wave frequencies. These via transitions have been studied and analyzed extensively [42]. Although different structures have been suggested to improve their performance, more work is still required to optimize performance over a wide frequency range.

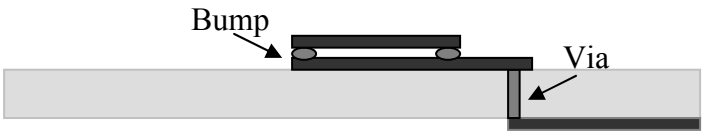

Figure 2.22: Interconnect through via and solder bumps.

Another attractive technique for an interlayer connection is flipchip technology and conductor bumps, as shown in Figure 2.22. It is a cost effective and promising method that has been investigated by Heinrich and presented in several papers [43]-[44]. It is reported that at lower frequencies the bump behaves as a capacitor due to the overlap area of the two conductors in the bump-pads. As the operating frequency is increased, the interconnect behavior becomes inductive. Careful consideration should be given to the size and shape of the bumps since they have impact on the return loss performance.

2.5. Switch Matrices

As it was mentioned, one of the main applications of the switches is for signal routing or redundancy schemes. The complexity of an interconnect network is determined

by trade offs of user needs, insertion loss, and cost. Among the various existing topologies, rearrangeably nonblocking Benes network shown in Figure 2.23 is one of the most well known structures [45]. It allows any point to point connection to be establishedm, but one or more existing connections may need to be rearranged.

There are various other structures which are used, depending on their applications. For instance, the configurations shown in Figure 2.24 can be used to provide protection

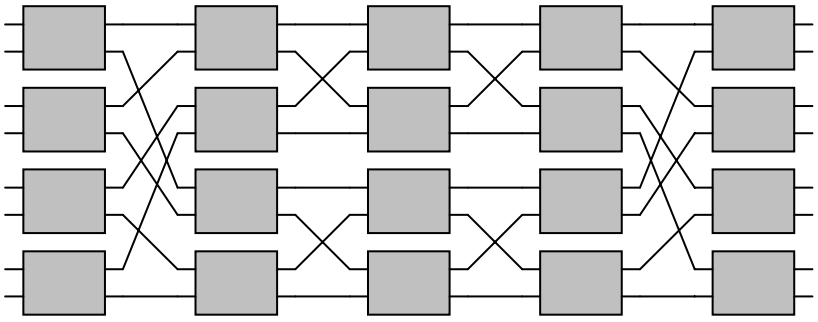

Figure 2.23: An 8×8 Benes Network

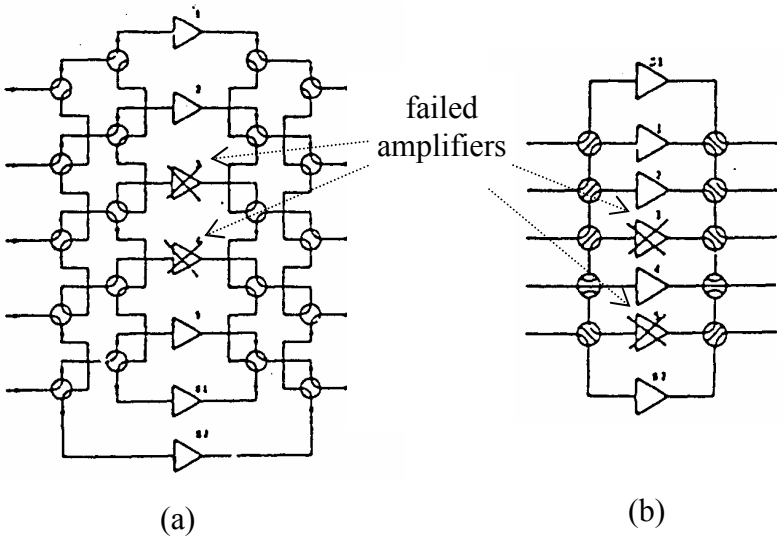

Figure 2.24 : Redundancy system with five primary channels and two spare channels using (a) C type and (b) R type switches as building blocks.

for a system and increase its reliability. Such configurations provide a five to seven redundancy for up to two failures of the amplifiers. C and R switches are used as the basic building blocks of the matrix [46].

Chapter 3

Planar (2D) Multi-Port RF MEMS Switches

3.1. Introduction

Over the last five years, numerous papers have been published on RF MEMS switches [10]-[21]. However, most of the research reported in the literature has been directed toward the development of SPST switches. They are two-port devices which act as simple RF relays. In today's communication systems, switches are typically used in the form of switch matrices either for redundancy or for signal routing. The use of multi-port switches, rather than SPST switches, as the basic building blocks, considerably simplifies the integration problem of large size switch matrices. In our knowledge, very limited work has been reported in lditerature on integrated multi-port MEMS switches [22].

In this investigation, electrostatic and thermal actuators have been employed to develop multi port switches such as Single-Pole Double-Throw (SP2T), Single-Pole Three-Throw (SP3T), C-type (transfer), and R-type switches. The design and analysis of these switches as well as their monolithic and hybrid fabrication are presented in this chapter. They represent the basic building blocks for the realization of large switch matrices.

3.2. Hybrid Electrostatic Multi-Port Switches

In this section, integrated electrostatic SP3T and C-type MEMS switches are demonstrated. RF simulation, along with circuit modeling is used to analyze and design the switches. Bi-layer cantilever beams with narrow tips are incorporated on top of the co-planar transmission lines by using flip chip technology to form the proposed structures. After the SP3T switch is described in details the proposed C-type switch is explained and presented.

3.2.1. Single-Pole Three-Throw (SP3T) RF MEMS Switch

Figure 3.1 illustrates the proposed SP3T MEMS switch structure. It is a compact ($500\times500\mu m^2$) coplanar series switch, consisting of three actuating beams. One end of each beam is attached to a 50Ω coplanar transmission line, whereas the other end is suspended on top of another 50Ω coplanar transmission line to form a series-type contact switch. The pull down electrodes, which are part of the RF ground, are placed underneath the beams. The design can be implemented by integrating the beams and the substrate on one chip. Alternatively, the SP3T switch can be implemented in a hybrid form, where the beams are micro machined separately, and then integrated on an Alumina substrate by using flip-chip technology [47]. In this section, we report the results of the hybrid version of this switch and the monolithic fabrication is explained in details in the next section.

3.2.1.1. Fabrication Process

The beams are fabricated by the Multi-User MEMS Processes (MUMPs) surface micro machining [48]. Each beam is constructed of a Polysilicon layer with a thickness of 1.5μm coated by a gold layer of 0.5 μm. To improve the isolation of the switch the tips are narrowed and the contact is realized only by small tips at the end of the beams. The coplanar line circuit is fabricated on an Alumina substrate with a thickness of 254μm.

The beams are flipped on top of the gold-coated Alumina substrate by the flip chip

process and gold bumps, as shown in Figure 3.2. With this technology, a gold-to-gold contact is achieved while it can not be realized by using only the MUMPs process. Another advantage of this method is the possibility of using a low loss substrate for the microwave and radio frequency applications along with silicon micro machined beams.

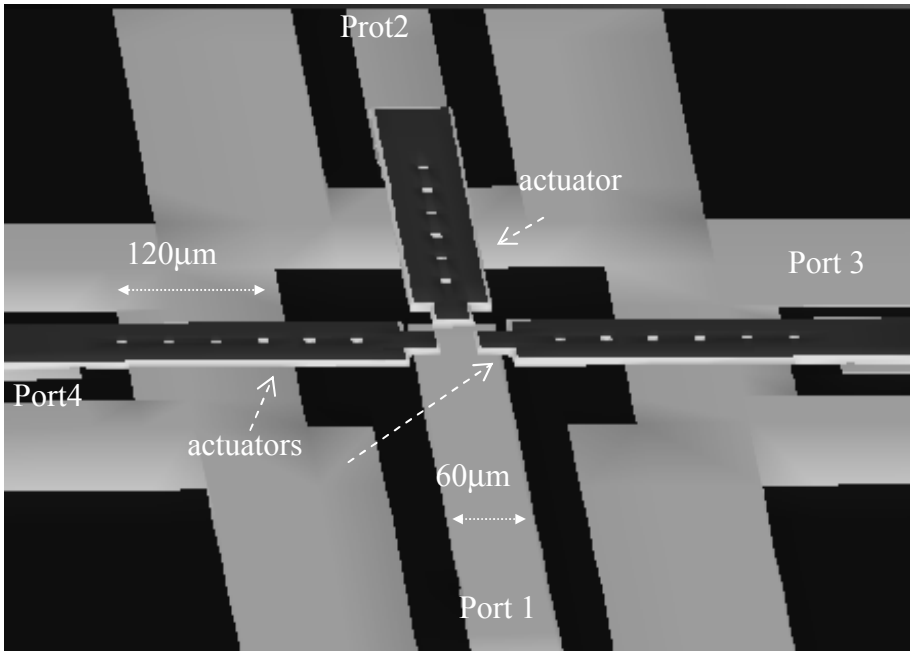

Figure 3.1: Proposed SP3T RF MEMS switch

To etch the sacrificial silicon dioxide layers and release the structure from the silicon substrate, the module is submerged in 49% HF for two minutes. This is due to the HF selectivity of the silicon dioxide over polysilicon, gold, and the alumina substrate. The trapped oxide beneath the beams is exposed to the HF through the release holes accommodated on the beams as indicated in Figure 3.3. The HF accessibility to the beams is performed through the space between the chip and the substrate; this space depends on the solder ball height. For a 15μm bump height and chip size of 2 × 2 mm, two minutes wet etching is favorable. For the larger chip sizes or smaller chip to substrate separation (< 15μm), a longer period of time is required. However, this results in some imperfection and deficiency in the samples due to the fact that the HF over etching affects the adhesion layer between the gold and the substrate, detaching the gold. To solve this issue, pre-etching which includes 1 minute wet etching before the flip chip integration, is suggested.

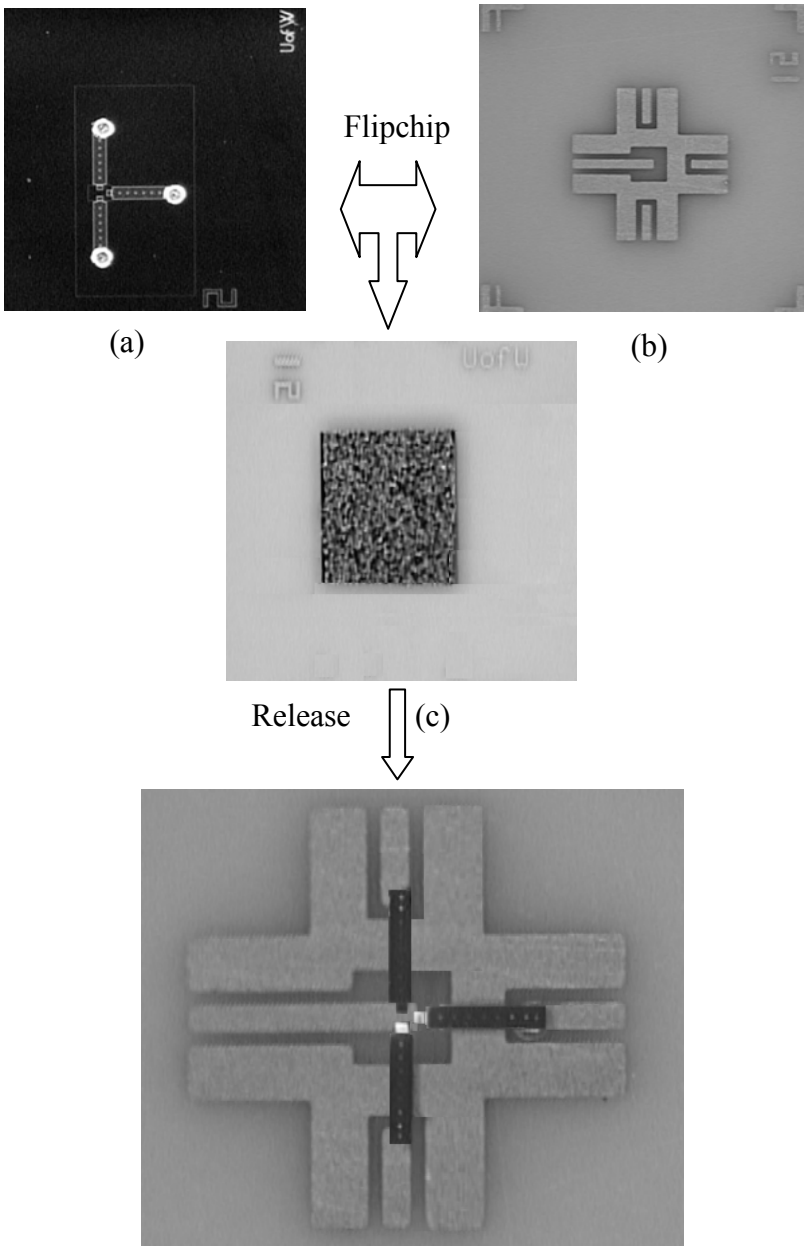

Figure 3.2: Fabrication process of the SP3T switch.(a) the PolyMUMPs chip which includes the beams, (b) the Alumina substrate,(c) the PolyMUMPs chip is attached to the substrate, and (d) the SP3T switch after releasing the beams from the PolyMUMPs chip.

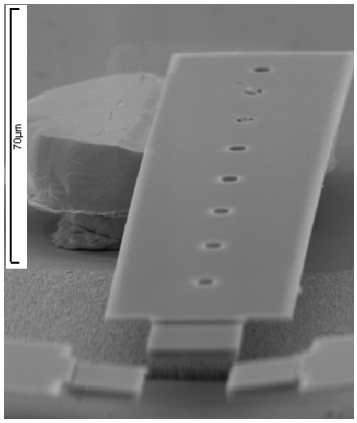

Figure 3.3 : Release holes and the narrowed tips on the SP3T switch (SEM photo).

3.2.1.2. Switch Design and Characteristic

The warpage of MEMS cantilever structures that consist of polysilicon and gold on top is one of the design considerations in using the PolyMUMPs process. The warpage exists because of the residual stresses and the thermal mismatches that result from the fabrication process [50]. The former is due to the chemical reactions such as oxidation and LPCVD deposition that can be modified by thermal processes such as annealing. The latter can be reduced by using a single layer beam structure to avoid different thermal expansion coefficients of the various layers.

However, in this design, the top layer of gold becomes the bottom layer of the beams, resulting in an inward warpage of the beams, as reflected in Figure 3.4. It brings the tips closer to the substrate while the distance between the beams and the DC electrodes is increased. The large distance prevents the beams from collapsing on to the electrodes (see Appendix A) and helps to reduce the coupling between the beams and the RF ground. The disadvantage of the warpage is that it increases the actuation voltage. It should be noted, however, that depending on the fabrication process and the residual stress of the layers, the flip chip gold bumps height can be controlled to realize the desired height.

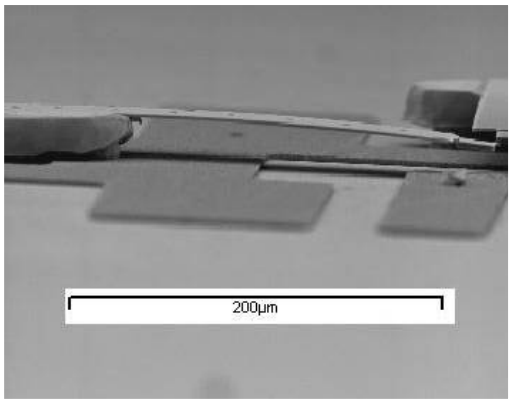

Figure 3.4: Cantilever beam warpage (SEM photo).

A full wave FEM analysis by Covnetor-Ware software is performed to find the turn ON voltage for the beams. As plotted in Figure 3.5, a turn ON voltage of 40 volts is predicted. However, it should be mentioned that in this simulation, the warping of the beam is not considered. In practice, to keep the distance between the beams and the input RF line constant, the distance between the electrode and the beam is increased leading to a higher required voltage of approximately 120 volts. A detailed mechanical modeling of the beam is performed and described in Appendix I.

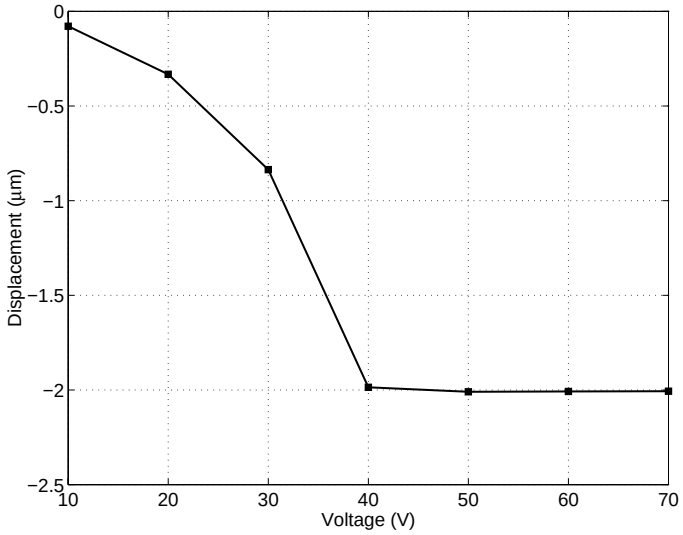

Figure 3.5: Coventor-Ware FEM analysis for the displacement.

Considerable efforts have been made to optimize the dimensions for a low return loss and maximize the isolation over a wide range of frequencies from DC to 40GHz. The HFSS simulation results for the case when port 2 is in the ON state and ports 3 and 4 are in the OFF state are shown in Figure 3.6. When port 3 is ON, and the others are OFF, the results are recorded in Figure 3.7. It is worth mentioning that due to the symmetric configuration of the switch, the results for the case of port 4 in ON and port 2 and 3 in OFF states are similar to the case in Figure 3.7.

To obtain a better insight in to the performance of the switch, its circuit model is studied. The circuit is illustrated in Figure 3.8 and the results are compared to those of the HFSS in Figure 3.6. At the input of each port, there is a 50Ω transmission line, followed by gold bumps which attach the beam. Typically, these bumps demonstrate capacitive performance at low frequencies and are inductive at high frequencies [51]. In the investigation described in this thesis, we found that the switch performance highly depends on the bumps which play an inductive role in the range of interest.

Moreover, due to the multi-port structure of the switch, the isolation of the throw ports becomes an important issue. It is evident that because of the narrow tips of the beams in this structure and thus small capacitors, a satisfactory isolation between the ports is achieved. The inter-coupling capacitors of the output ports are approximately 0.1 and 0.3fF whereas the isolation capacitors between the input line and the OFF ports are 5fF. The latter is determined by the coupling across a 2-micron gap between the narrow tips and the RF line.

In the ON state, the beam represents a bridge passing over the electrode which is demonstrated by a 20fF capacitor and a very small inductor. The beam widths are 60μm which are changed to 30μm at the tips. This change is represented by two series inductors and a parallel capacitor. Afterward, it is followed by a series contact resistance that can be obtained by the following equation [13]:

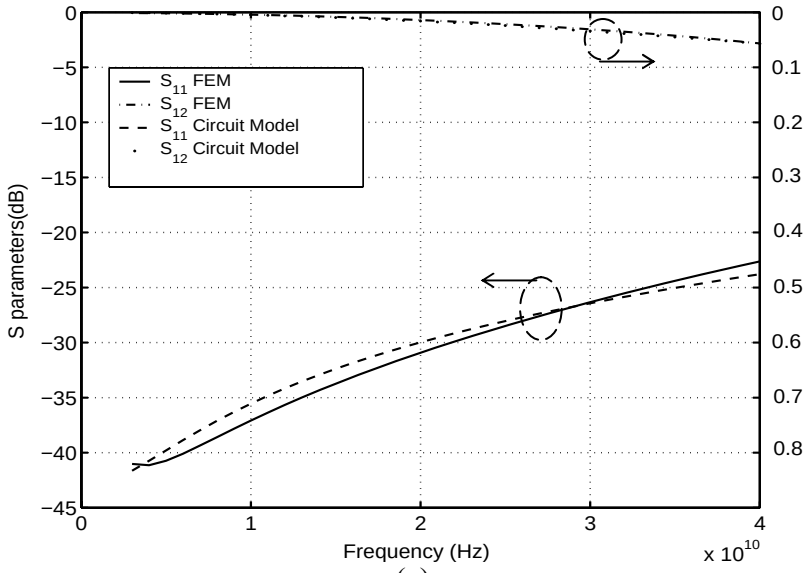

(a)

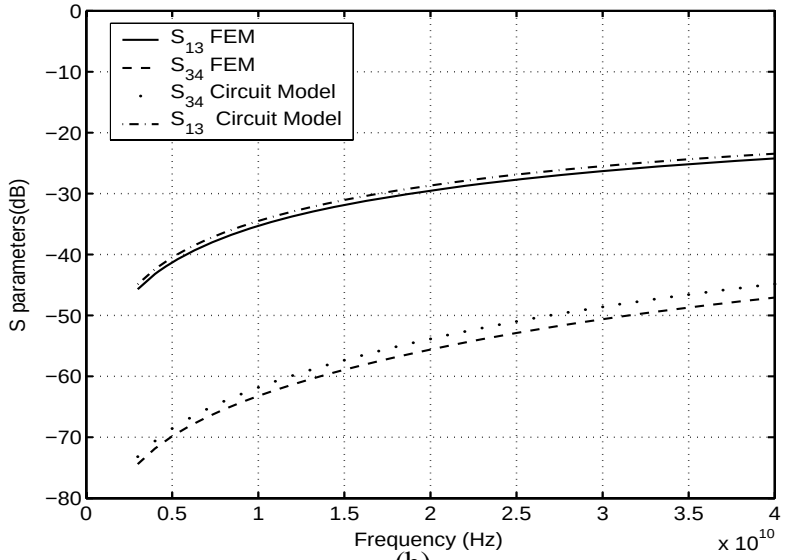

(b)

*Figure 3.6**:** RF performance for the switch in Figure 3.1 when port 2 is ON and ports 3 and 4 are OFF, (a) insertion loss and return loss,(b) isolation between the ports.*

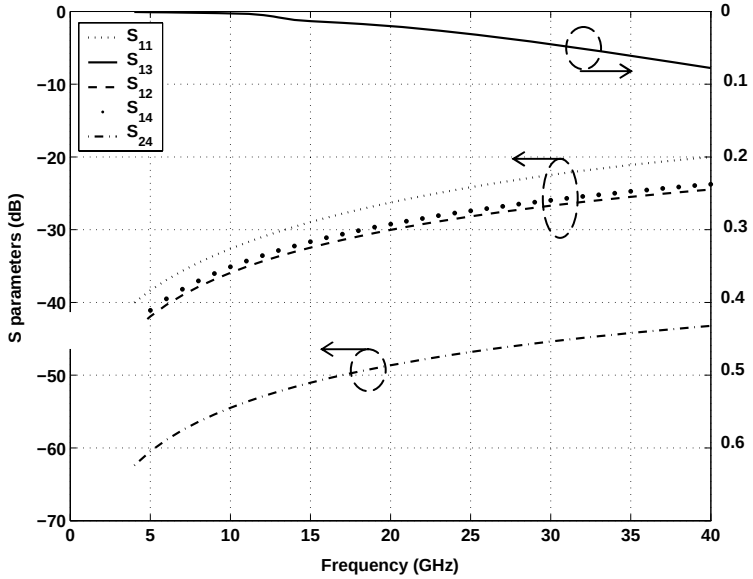

Figure 3.7: RF performance for the switch shown in Figure 3.2 when port 3 is ON and ports 2 and 4 are OFF

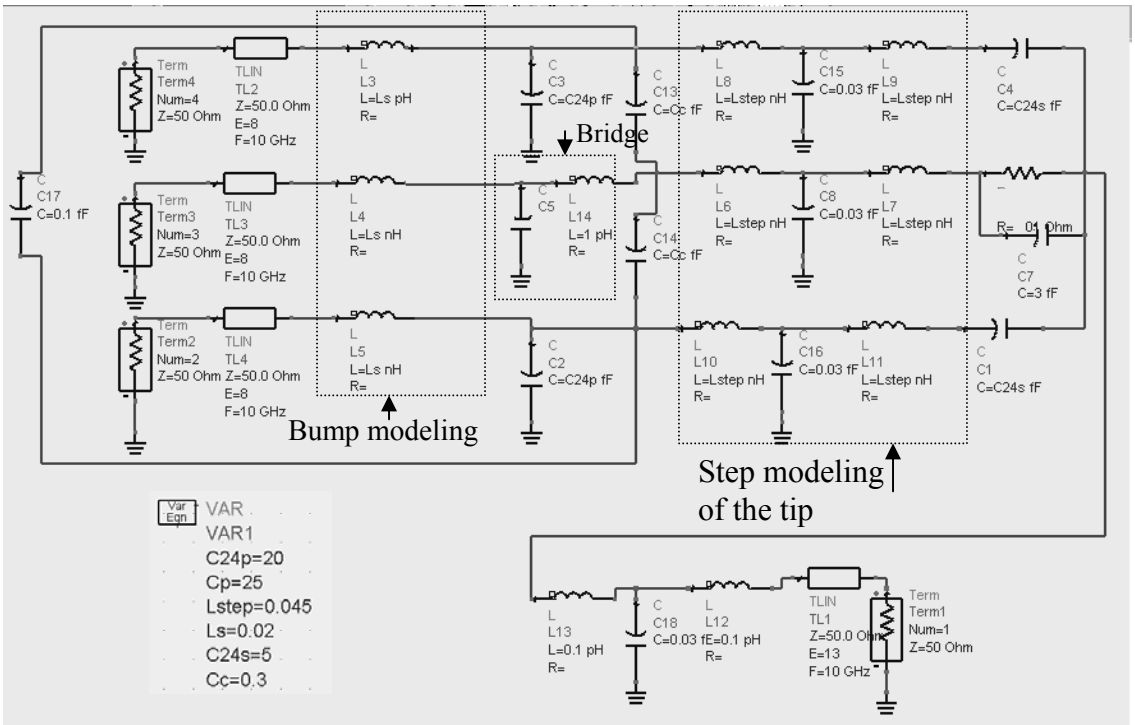

Figure 3.8: Circuit model for the switch shown in Figure 3.1, when port 3 is ON and the other ports are OFF.

$$R_{contact} = \sqrt{\frac{\pi}{4}} \frac{\rho\sqrt{\sigma}}{\sqrt{F}} \tag{3.1}$$

where σ is the yield strength, F is the contact force (See Appendix A) and ρ is the resistivity of the gold which is around 2.6×10^{-6} Ω–cm in the MUMPS process. Consequently, the contact resistance for a good contact is approximately 0.15 Ω.

3.2.1.3. Measured Results

Now that the theoretical RF characteristic of the switch has been considered, its experimental behavior is investigated. A two-port on wafer 180 degree probe measurement is performed. For measurement purposes, the switch is actuated by applying a DC voltage to the RF ports, through bias-tees. With the application of the actuation DC voltage, the beams deflect, thus closing the gap while providing a continuous path through the transmission line. The results are shown in Figure 3.9 (a) and (b) for the ON and OFF states.

Primarily, the mechanical actuation of the beam is tested. Throughout the experiment, the required actuation voltage of 120-140 volts is measured. Also, the isolation of the switch specified by S_{12} in the OFF state is measured. The results are better than -30dB up to 20GHz. This data is obtained while the switch is in the rest position and no DC voltage is applied. The results show good agreement with those of the HFSS© simulation in Figure 3.6. In addition, the ON state of the switch is measured and recorded in Figure 3.9 (a). The switch exhibits about 0.5dB insertion loss, better than -20dB return loss, and more than 30dB isolation up to 20GHz.

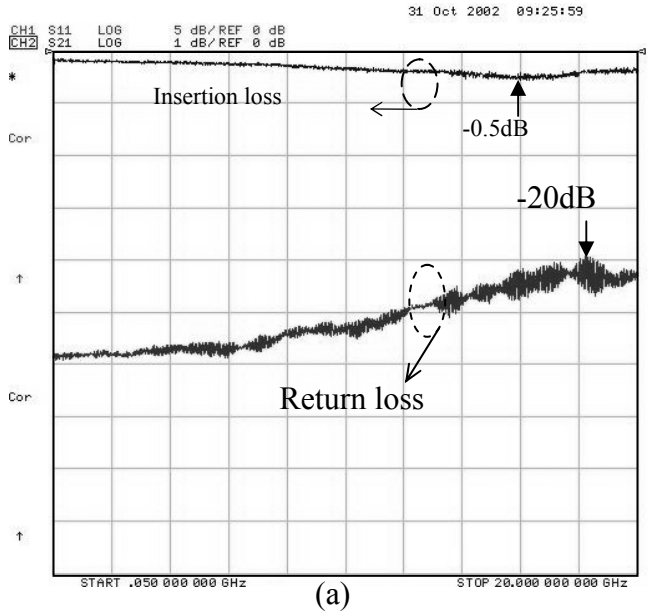

Figure 3.9: Measurement results for the switch shown in Figure 3.1 when port 3 and 4 are OFF: (a) return loss and insertion loss and (b) isolation for port 2.

To turn one port ON, the associated beam is connected to the positive potential, and the electrode is connected to ground while the remaining beams are left floating. It should be noted that, leaving the ports in a floating potential, may cause unwanted charging of the beams and thus unintended actuation. Therefore, to improve the design, separate DC electrodes can be employed since they have been used for the C switch, explained in the following section.

3.2.2. C-Type RF MEMS Switch

C-type microwave switches are widely utilized in sophisticated redundancy switch matrices for satellite applications. The switches have two operational states that are illustrated in Figure 3.10. In state I connections are established between ports 1 and 2 and between ports 3 and 4. In case of any failure, the arrangement of the switch is modified to state II to shift the signal path to the spare components such that full functionality of the system is maintained.

Figure 3.10: C-type switch schematic; in state I ports 1-2 & 3-4 are connected and in state II ports 1-4 & 2-3 are connected.

The mechanical design of the switch begins with considering the required DC actuation voltage. Equation (3.2) presents a widely cited formula for calculating the actuating voltage of cantilever beams as follows:

$$V = \sqrt{\frac{2kg^2(g_o - g)}{\varepsilon_0 A}} \tag{3.2}$$

Where A is the electrode area, g_o is the initial gap between the electrode and the beam, g is the steady gap between the electrode and the beam after the application of voltage, and ε_o is the dielectric permittivity on the top of the electrode. k is the spring constant of a cantilever beam that can be written as $k = \frac{EWt^3}{4l^3}$ where E represents young modules, W is the beam width, t is the thickness, and l is the beam length (for more information on the parameters, see Appendix A)

As shown in Equation (3.2), the actuating voltage is proportional to the square root of the spring constant *k.* Therefore, for decreasing the actuating voltage from 120 (as for the SP3T reported in the previous section), the spring constant *k* should be proportionally reduced. Previously, serpentine beams have been employed to reduce the pull in voltage for clamped-clamped beam switches [49]. Here, it is proposed to use similar type of spring in series with the primary cantilever beam as represented in Figure 3.11.

The general form of the serpentine spring constant has been reported as [49]

$$k = \left[\frac{8N^3a^3 + 2Nb^3}{3EI_x} + \frac{abN[3b + (2N+1)(4N+1)a}{3GJ} - \frac{Na^2\left[\frac{2Na}{EI_x} + \frac{(2N+1)b}{GJ}\right]^2}{2\left(\frac{a}{EI_x} + \frac{b}{GJ}\right)} - \frac{Nb^2}{2}\left(\frac{a}{GJ} + \frac{b}{EI_x}\right)\right] \tag{3.3}$$

where the parameters are defined in Table 3.1 and N is the number of meanders. Equation (3.3) in combination with the lumped modeling is adopted to develop a Matlab code to

calculate the total spring constant of the new beams.

Primary meander length (a)	*15(μm)*
Secondary meander length (b)	*125(μm)*
Switch thickness (t)	*1.5(μm)*
Beam width (ω)	*5(μm)*
Poly silicon young modulus (E)	*163 GPa*
Polysilicon Poission's ratio (ν)	*0.22*
Shear modulus (G)	$E/(2(1+\nu))$
x-axis moment of inertia (I_x)	$\omega t^3/12$
z-axis moment of inertia (I_z)	$t\omega^3/12$
Polar moment of inertia (I_p)	I_z+I_x
Torsion constant (J)	$0.413I_p$

Table 3.1: Physical dimensions and material constants for the proposed low-voltage switch

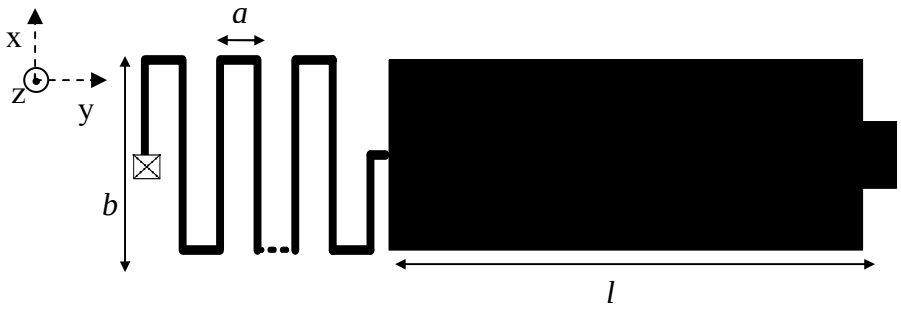

Figure 3.11: Proposed configuration to use a serpentine beam to reduce the actuation voltage.

This idea is used to design a new beam with N=1 and reduce the *k* to 50%, and thus, decrease the actuating voltage to about 70%. The measured actuation voltage is around 80 volts which verifies the calculation. However, one should note that additional meanders could add extra unwanted inductive loading to the switch in high frequencies. Therefore, careful modeling of the structure is essential.

The switch is produced by the same technique as that of the previously reported SP3T switch and is shown in Figure 3.12 . The beams are fabricated using poly MUMPs process [50] and the electrodes and the RF lines are patterned over a 10 mil (~254μm) alumina substrate. Then using the flip chip technology, the beams are assembled on the substrate and HF wet etching is used to release the switch. The required bridges are created by using wire bonding. In state I, beams 1 and 3 are actuated, whereas for state II beams 2 and 4 are pulled down.

The RF performance of the switch is analyzed by HFSS© and then optimized. The simulation results for the switch in Figure 3.13 and illustrate a return loss and an isolation of better than -20 dB up to 15GHz. It is noteworthy that in this configuration, the DC electrodes of the switch are separated from the RF ground plane, providing more flexibility to control the beams. However, to suppress the odd parasitic modes due to the discontinuities on the ground plane, air gap bridges are required which are realized by using wire bonds. Due to the fact that the structure of the switch is symmetric, the RF characteristics of the other ports are similar to those of port1.

A two-port RF measurement is performed on the switch when port 1 is connected to port 2 and the results are deployed in Figure 3.14. The measured return loss for port 1 and 2 is better than -15dB up to 15GHz. The insertion loss is less than 1dB which is attributed to the error in the assembly and the contact resistance. The isolation is better than 20dB, as predicted.

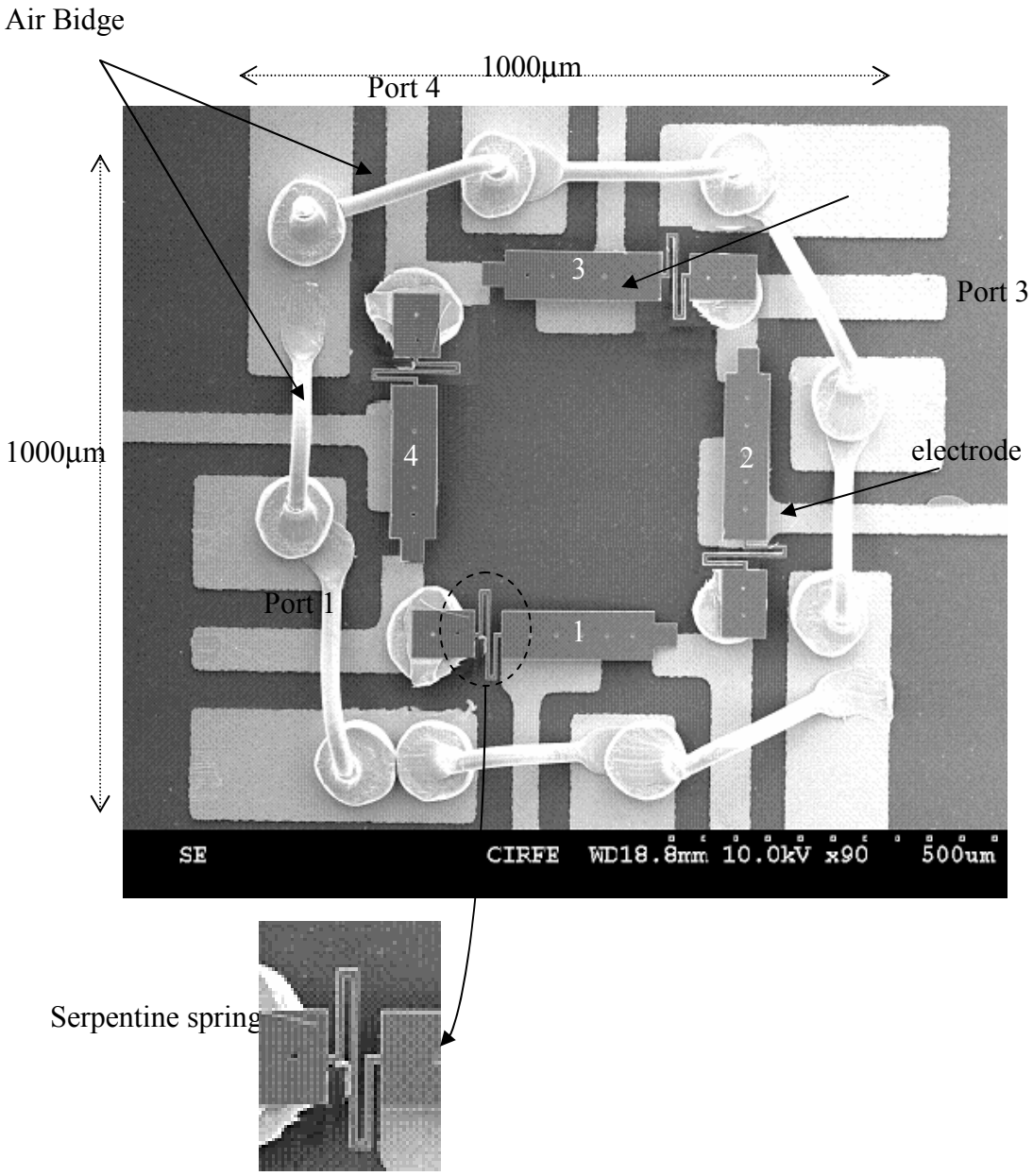

Figure 3.12: C-type RF MEMS switch after complete assembly.

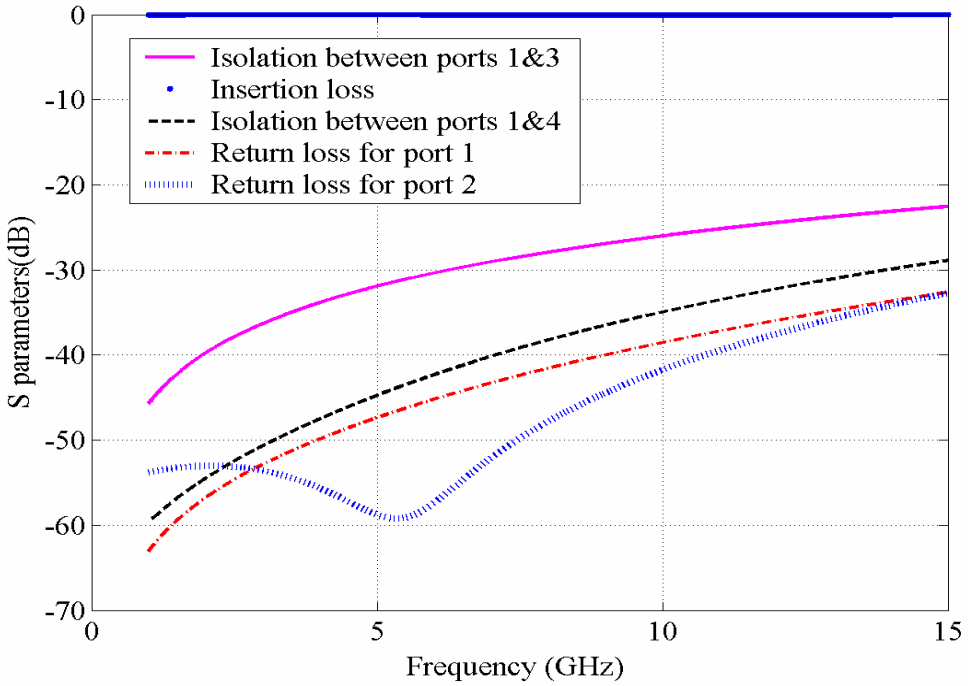

Figure 3.13: Simulation results for the proposed C-type switch.

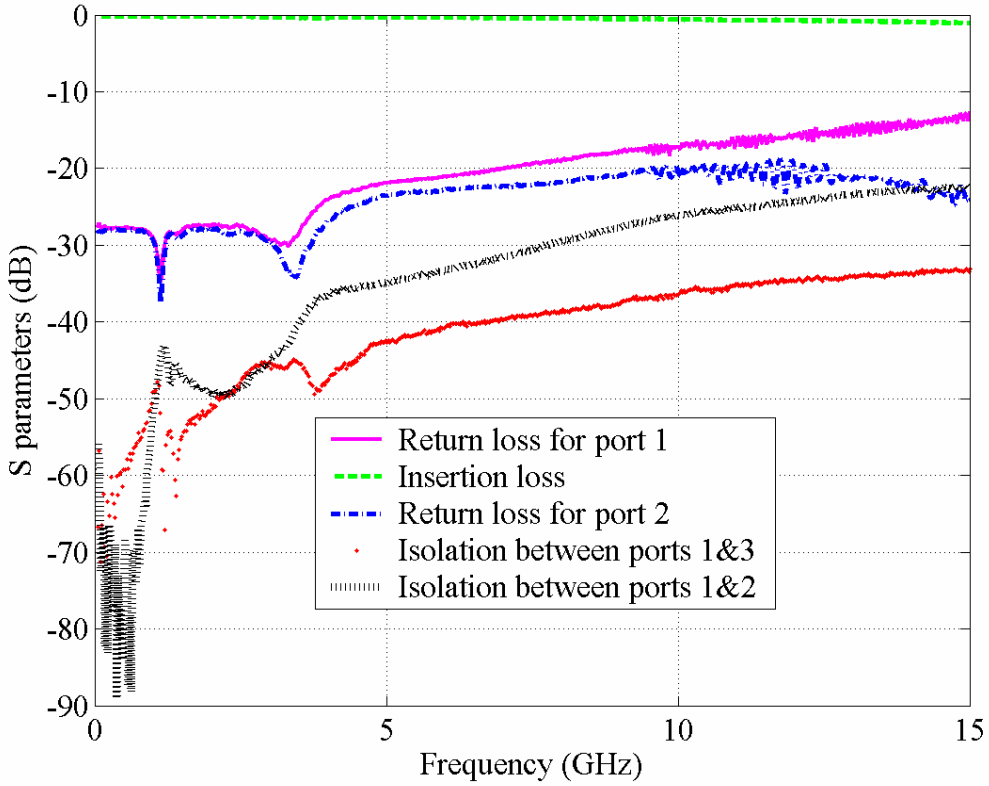

Figure 3.14: Measured RF characteristics of the proposed C switch.

3.3. Monolithic Multi-Port Switches

SP3T, C-type, and R-type switches are the focus of this section. A monolithic configuration rather than hybrid integration not only improves the performance but also increases the production yield and reproducibility. In this section, a new fabrication process dedicated to multi-port MEMS switches is presented and is used to construct multi-port MEMS switches.

3.3.1. Fabrication Process

An alumina substrate is selected for the base substrate since it retains its intrinsic properties during the process and exhibits a good RF performance at high frequencies. The fabrication of the switches is comprised of the simultaneous processing of all the electrodes and the beams by one type of process. This requires a total of six mask levels to pattern the different layers for the switches as shown in Figure 3.15. All the fabrication process is carried out in the CIRFE lab at the University of Waterloo.

Process starts with Cr evaporation of about 400nm. This layer is used for resistors as well as adhesion of the following gold film. The gold film is 1μm and is deposited using E-beam evaporator without breaking the vacuum resulting in a good adhesion. The lithography of this level is performed using AZ2035 (a negative photoresist) and a dark field mask. Quick RIE DESCUM step is used to clear the unwanted remaining residue of the resist. For wet etching of the gold film, a solution of Potassium Iodide and Iodine is employed that results in a complete removal of the unwanted features. Afterwards, second mask is used to pattern the Cr for the DC bias resistors.

Silicon dioxide as a dielectric layer is then deposited at 250 degrees by the Plasma Enhanced Chemical Vapor Deposition (PECVD) system. This film is mainly used for the isolation between the electrodes and the beams. To provide good adhesion of oxide and gold, very thin film of TiW (400nm) is sputtered under the oxide layer. The third mask is used for the patterning and the process is continued with plasma etching of the oxide and a CF_4 plasma using RIE.

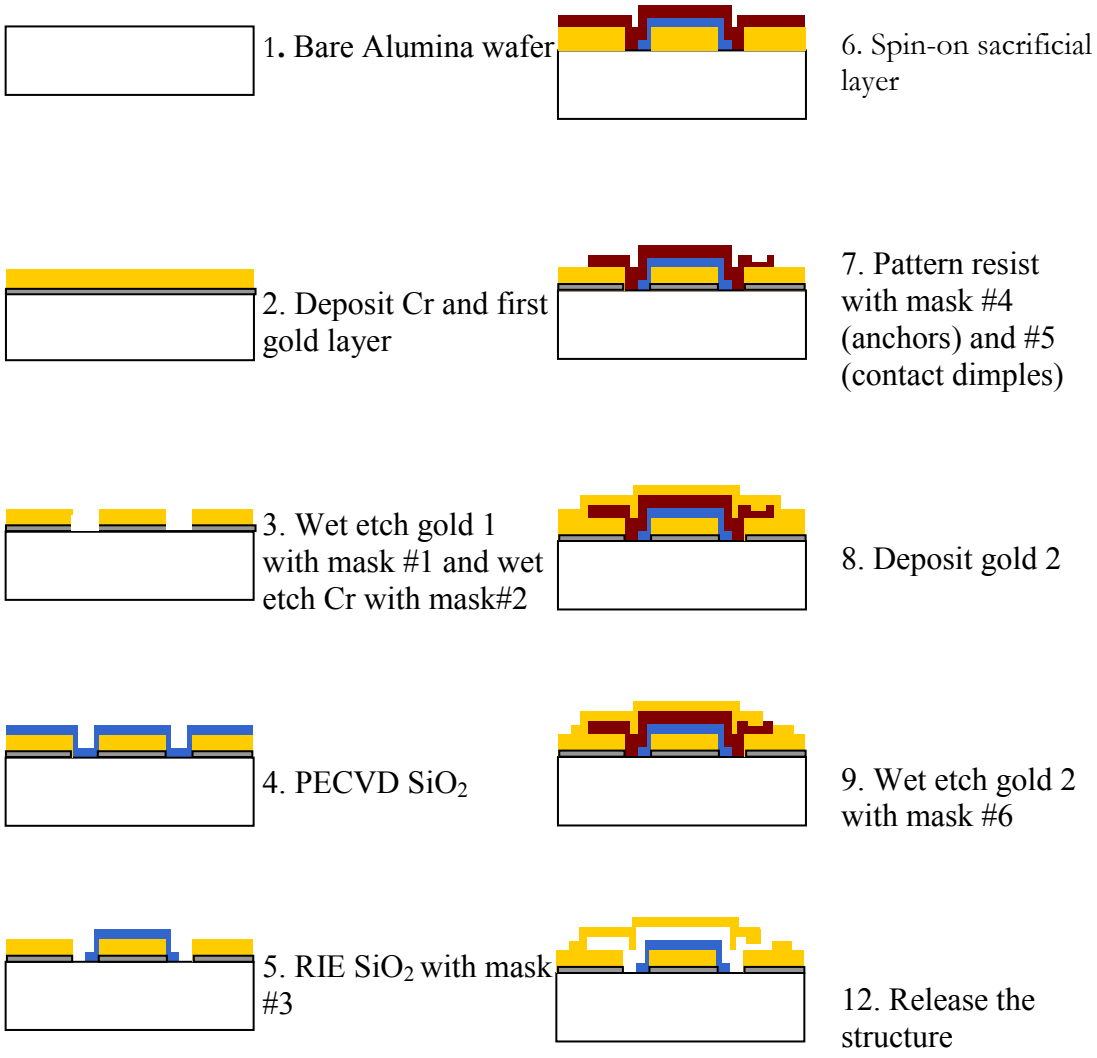

Figure 3.15: Fabrication process of the monolithic RF MEMS switches in CIRFE lab.

After the patterning of the oxide layer, the sacrificial layer the (AZ 3330 photoresist) of 2µm is spin coated. Initially, the resist is fully exposed through mask # 4 to pattern the anchors. Then it is followed by a partial exposure step using mask #5. This helps to develop half the thickness of the resist and provides the required openings for the contact dimples of the switches. Four minutes of 120 degrees hard bake is used to overflow the photoresist and create sloped side walls.

The last film of 2μm gold is evaporated using E-beam evaporator as the structural layer. The sixth mask (dark filed mask) is used for lithography in combination with negative resist. After etching the top metal in a similar manner as the first step, the wafer is dry released. This step is performed in RIE and oxygen plasma with high pressure, high ICP (Inductive Coupled Plasma) power and much less RF power. This reduces the directivity of the etch, helps in a large under etch, and results in released devices.

3.3.2. Monolithic Single-Pole Three-Throw (SP3T) RF MEMS Switch

A new SP3T switch is fabricated based on the proposed fabrication process in the CIRFE lab at the University of Waterloo and is represented in Figure 3.16. It is a compact ($500\times500\mu m^2$) coplanar series switch, consisting of three actuating beams. One end of each beam is attached to a 50Ω coplanar transmission line, whereas the other end is

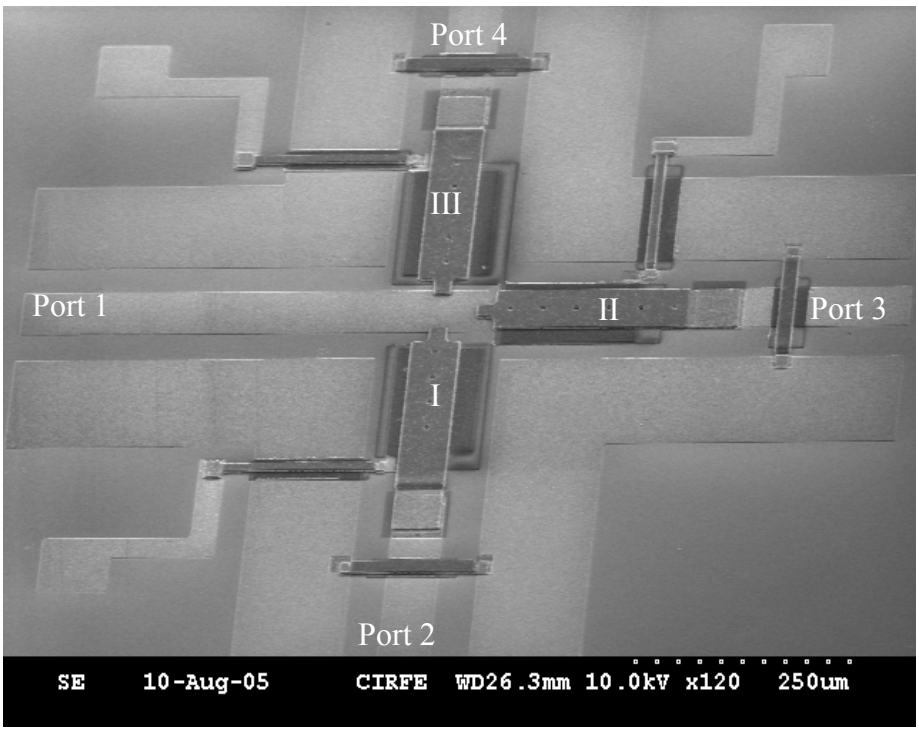

Figure 3.16: Proposed monolithic SP3T RF MEMS switch fabricated in the CIRFE lab at the University of Waterloo.

suspended on top of another 50Ω coplanar transmission line to form a series-type contact switch. However, in contrast to the previously presented SP3T switch, the electrodes are separated from the RF ground plane which results in a better control of the beams, and also prevents unintended actuation. To avoid producing parasitic CPW modes due to the existing discontinuities on the ground plane, air bridges are used.

To evaluate the switch performance, a two port on-wafer measurement is performed. The required actuation voltage is about 65 volts to obtain good contact force. The switch exhibits a good RF performance as presented in Figure 3.17. The insertion loss for the ON state of Port 2 is less than 0.5 dB, the isolation is more than 30dB and the return loss is better than -20dB up to 10GHz. While Port 3 is ON switch shows similar performance with excellent insertion loss and Return loss. The third state of the switch where port 4 is ON is similar to the case that port 2 is ON. Compared to the previously presented switch in section 3.2.1, the switch has a much higher yield and consistency. The main superiority of this switch is its potential for integration in large numbers especially in the form of switch matrices.

3.3.3. Monolithic C-type RF MEMS Switch

With the advantages of monolithic fabrication, a new C-type switch to improve the performance of the presented switch in section 3.2.2, is introduced. The fabricated structure is shown in Figure 3.18 where the switch presents two different states. First, in the State I, the connection is established between ports 1 to 2, and 3 to 4 and in the state II the connection is changed from ports 1 to 4 and 2 to 3.

The input ports are 50Ω CPW lines with a signal line width of 60μm, gap of 40μm, and ground plane width of 120μm. Air bridges are employed to prevent the parasitic odd CPW modes and to improve the performance. The structural material of the beam is 2μm of gold with a spacing of 3μm with the electrodes that includes 1μm oxide and 2μm gap. The cantilever beam is identical to that of the previously mentioned SP3T switch

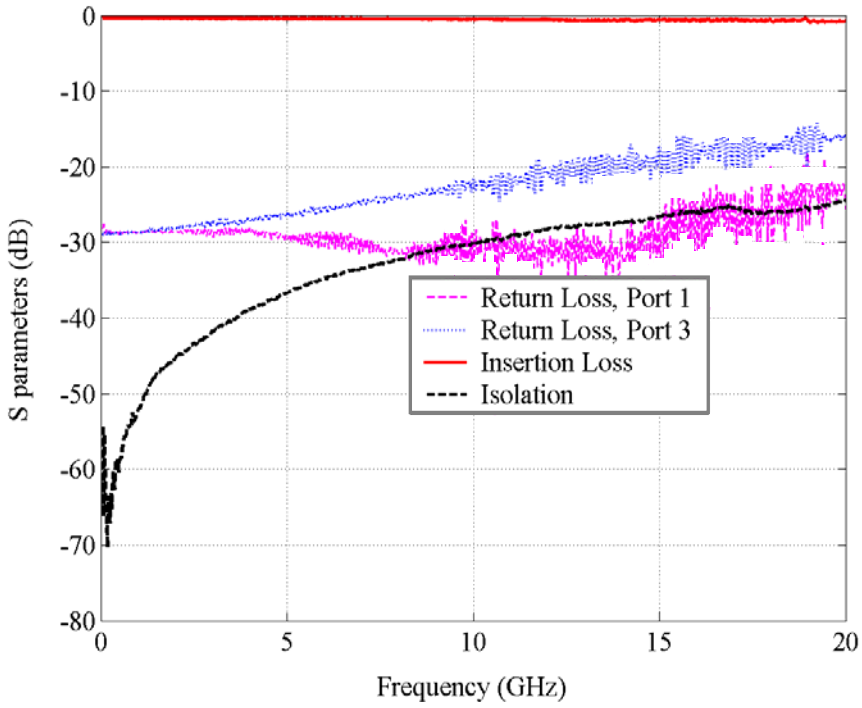

(a)

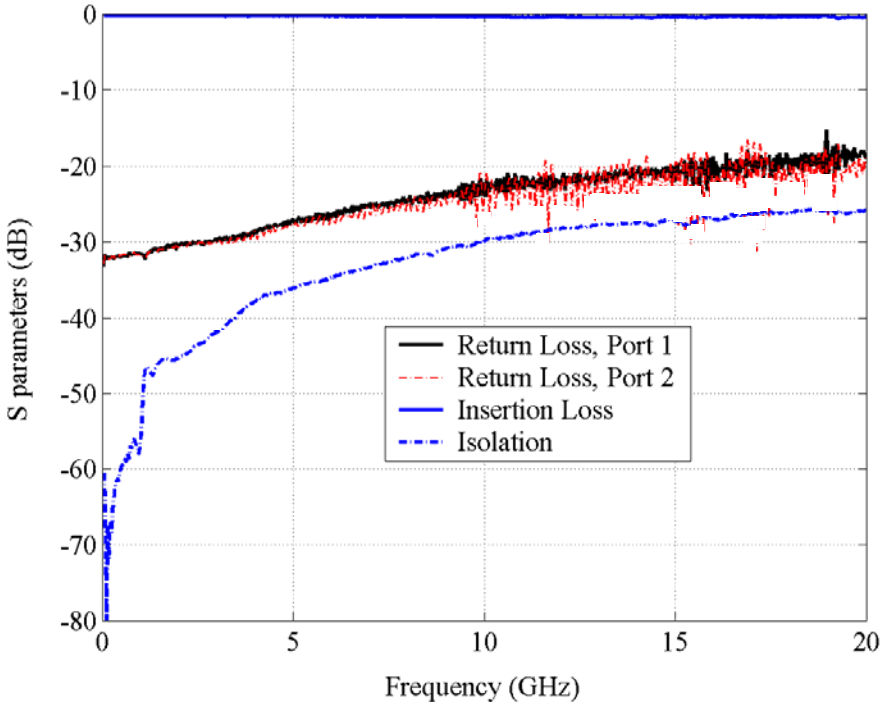

(b)

Figure 3.17: Two port measurement results for the proposed SP3T switch (a) while port 1 & 2 are connected, and (b) port 1&3 are connected

with actuation voltage of 65 volts. A two port on wafer probe measurement shows an excellent RF performance as presented in Figure 3.9. The insertion loss of the switch is 0.8dB at 10GHz and about 1.1dB at 15GHz. The return loss is -15dB at 10GHz, and the isolation exceeds 20dB for all the frequency range up to 15GHz. This switch is indeed suitable for integration in the redundancy switch matrices and redundancy networks.

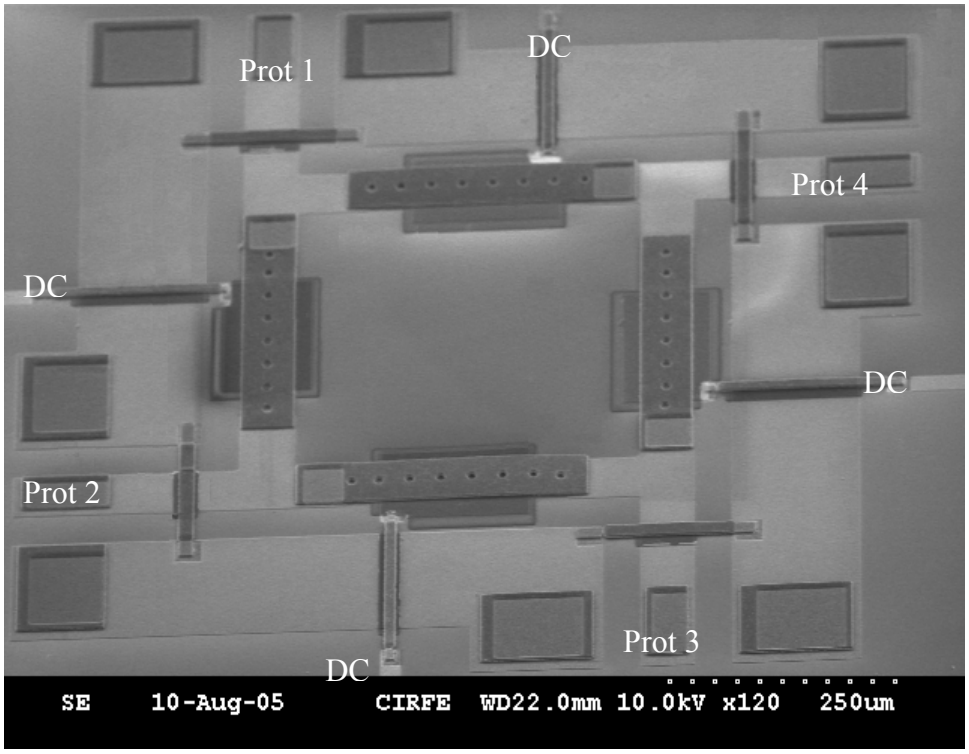

Figure 3.18: Proposed monolithic C-type switch fabricated in the CIRFE lab at the University of Waterloo.

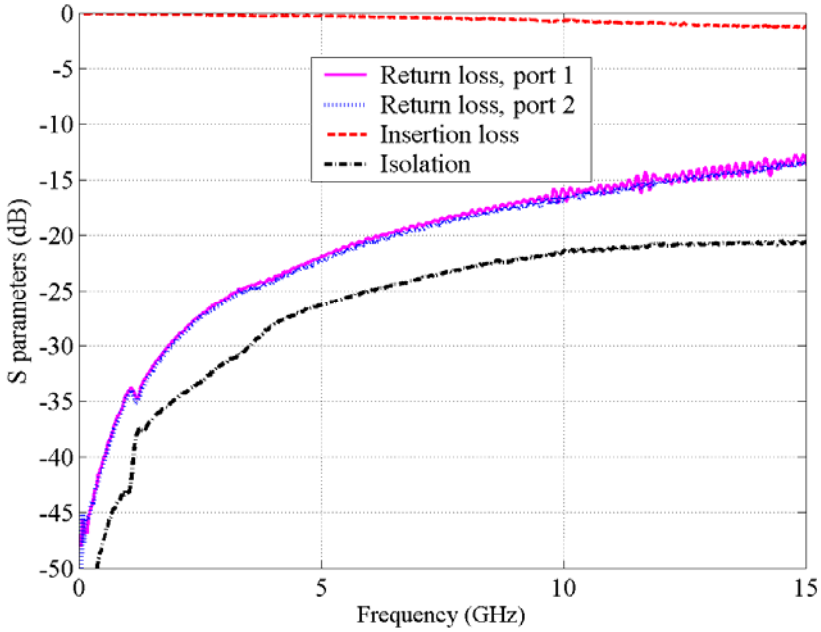

Figure 3.19: Measured results for the proposed switch in Figure 3.18.

3.3.4. Monolithic R-type RF MEMS Switch

R-type switches provide a superior advantage in comparison to *C* switches as they operate in one more state (shown in Figure 3.21) which considerably reduces the number of building blocks in redundancy switch matrices and simplifies the overall topology.

Figure 3.20 illustrates the proposed R-type MEMS switch. The switch is fabricated in the CIRFE lab, based on the fabrication process proposed in section 3.3.1. The switch has three different states. The ON position of the beams, 2 and 4, correspond to state I shown in Figure 3.21, whereas state II is achieved when beams 1 and 3 are in the ON position. Additionally, when all the beams except beam 5 are OFF, the switch represents state III.

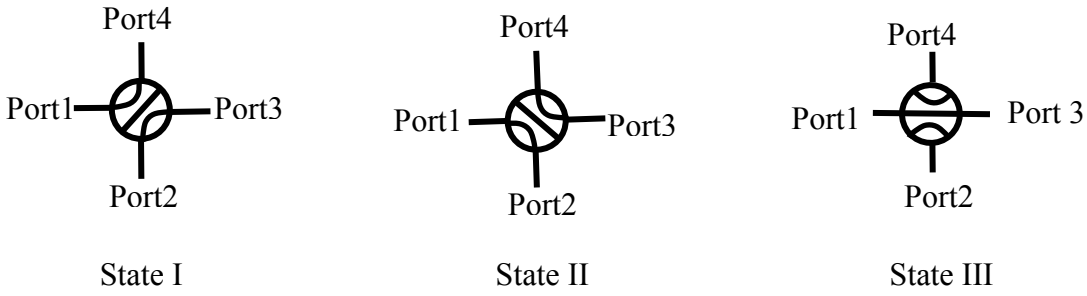

Figure 3.21: R type switch and its three different states; state I ports 1 and 4, and 2 and 3, are connected, state II ports 1and 2, and 3and 4, are connected, and state III only ports 1and 3, are connected.

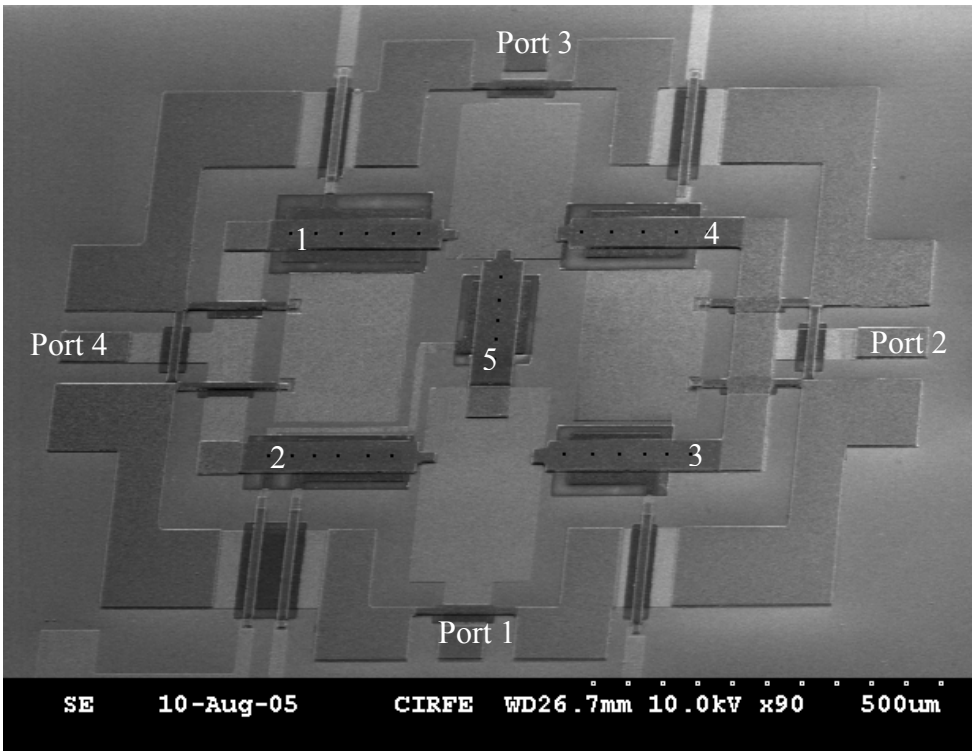

Figure 3.20: Fabricated R-type switch in the CIRFE lab at the University of Waterloo

This switch consists of four CPW ports that are transformed to microstrip lines by using the step junctions at ports 1 and 3. The steps' inductive effect is optimized to compensate for the capacitive characteristics of the beams. Moreover, the small tips at the beams are also used to reduce the coupling between the adjacent ports.

The measured results of the proposed switch verify the concept as displayed in Figure 3.22. Overall, the switch shows better than 0.8dB insertion loss at 10GHz for all the states and about a -20dB return loss. The isolation of the switch is more than 20dB for all the frequency range up to 15GHz. Because of the symmetry, the results of state II are similar to those of state I. The aforementioned switch is very suitable for integration in switch matrices, and considerably reduces the number of the switches in redundancy switch matrices.

3.4.Thermally Actuated Multi Port Switches

Compact and energy efficient micro-actuators that yield a high output force and displacement fulfill several uses in micro-system applications. This is more pronounced for contact switches since the contact resistance strongly depends on the applied force. Consequently, the use of thermal MEMS actuators is beneficial in developing RF MEMS switches.

Generally, thermal actuators, based on metal materials have a number of advantages due to metals large thermal expansion coefficients, and can deliver large displacements and forces and consume less power. The power consumption is even further reduced when the actuators are hermetically packaged in a vacuum. In this study, one of the most well known MEMS metal micro-actuators called the Thermal Expansion Device (TED) [52] is employed to develop novel SPST , SP2T, and C-type switches. The performance of this type of switch is investigated under room conditions as well as vacuum (see appendix B).

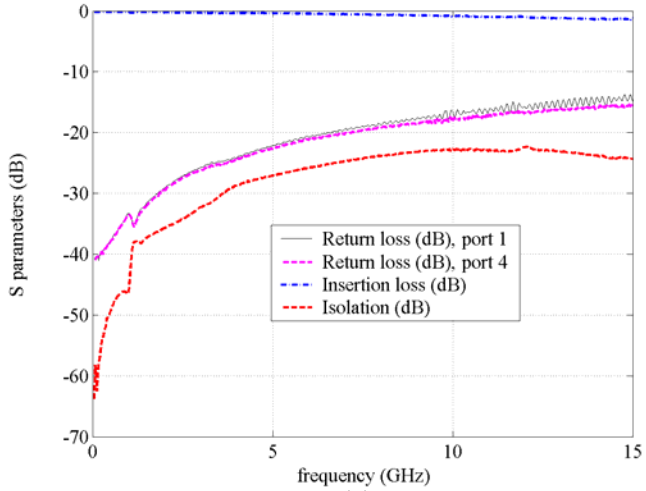

(a)

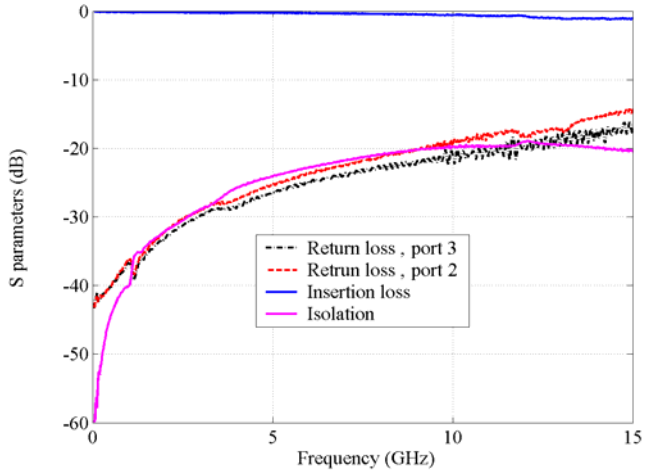

(b)

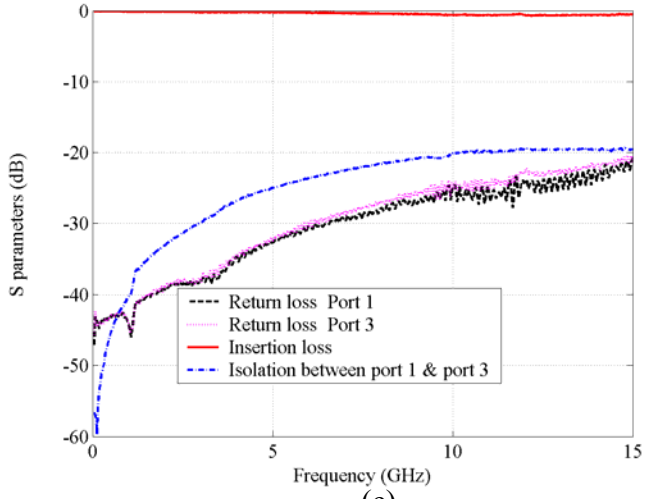

(c)

Figure 3.22: Measured results for the proposed R-type MEMS switch for (a) state I port 1 and 4 are connected, (b) state I port 2 and 3 are connected, and (c) state III port 1 and 3 are connected.

3.4.1. Operation Principle of the Proposed Thermal MEMS Switch

TED actuators consist of two metal arms with different widths as shown in Figure 3.23. The thin arm of the micro-actuator has a higher electrical resistance than the wide arm and therefore, on the application of a current, the thin arm is heated more. Consequently the thinner arm is elongated more than the wider arm, and produces a forward movement, that is transferred to an RF contact element by a dielectric layer (Silicon Nitride).

Figure 3.24 reflects the entire structure of the proposed SPST switch fabricated by the Metal MUMPs fabrication process [53]. The switch is based on finite ground CPW lines. The thickness of the lines is 20μm, the signal line width is 80μm, the spacing is 75μm and the ground plane width is 80μm. This creates a 50Ω line lying on top of silicon substrate. A 25μm trench is etched under the transmission lines to reduce the RF loss. As it was mentioned above, a dielectric layer of nitride is used to transfer the actuator movement to the contact element. This layer is released and located underneath the ground conductor. The use of an electric isolator rather than a conductor provides

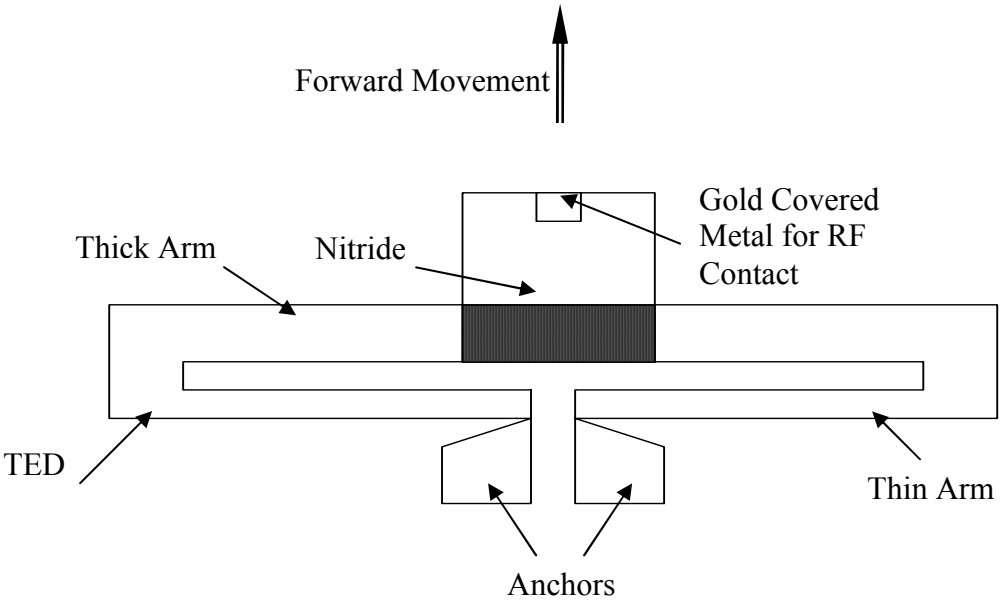

Figure 3.23: Proposed actuator based on thermal Expansion Device (TED.)

flexibility in the RF design of the switch, and renders the RF performance independent of the actuators structure. The contact element is a small gold cover nickel that has a low contact resistance with a 6μm gap to the signal line. By application of DC voltage, the actuator moves forward and shorts out the input line to the output port. On removal of the DC bias, the actuator returns to its initial position and the switch turns OFF.

To close the existing gap between the contact metal and the signal line, a displacement of 6 μm is required. The measured result indicates that a voltage of 1.64V induces a current of 360mA in the actuator. The generated heat from the current is 590mW which produces a forward movement and a high contact force at the signal line. To prove the concept, a two-port RF measurement is performed and the data are plotted in Figure 3.25. The results reveals a good return loss of better than -20dB for the frequency up to 20GHz. The insertion loss of the switch is less than 0.9dB up to 10GHz and increases to 1.5dB up to 20GHz. The insertion loss of the switch is mainly due to the

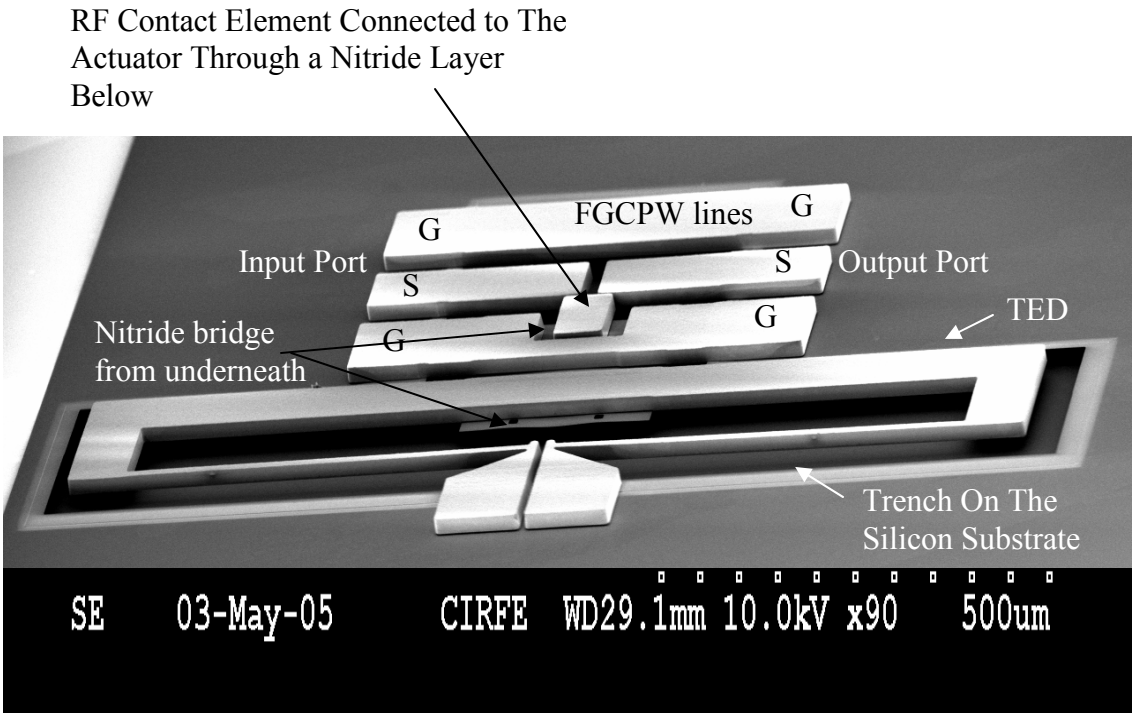

Figure 3.24: SEM picture of the proposed SPST switch.

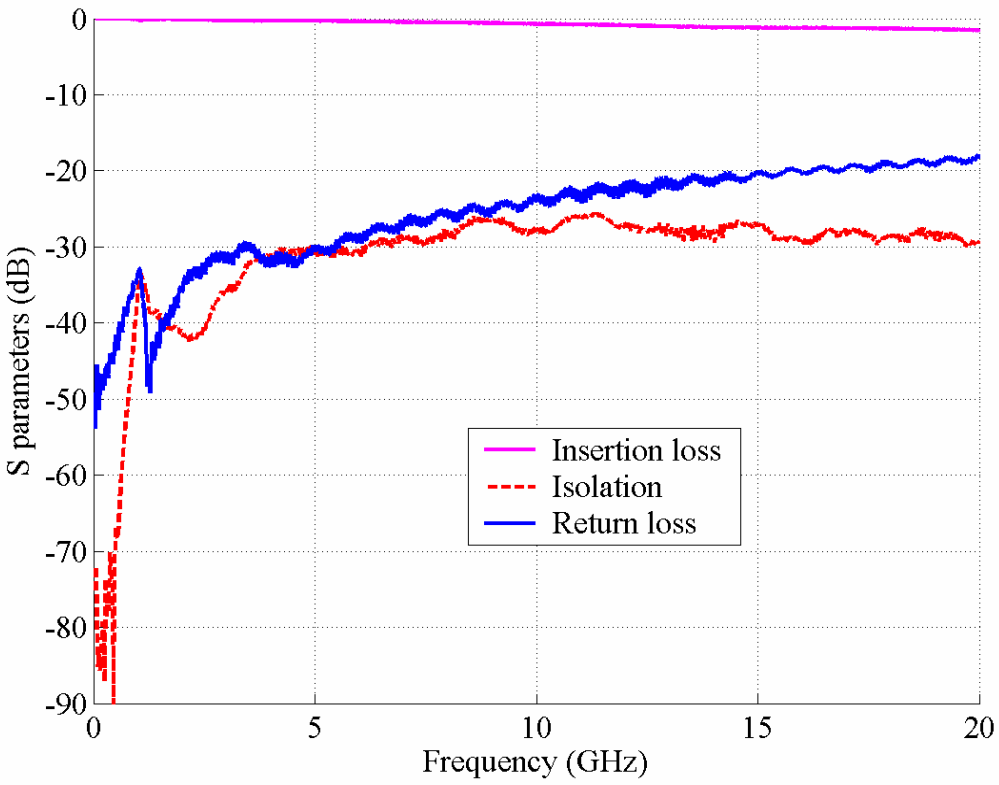

Figure 3.25: Measured performance of the proposed switch in Figure 3.24

low resistivity of the silicon substrate. In addition, the switch exhibits a good isolation of more than 25dB for the entire frequency range.

The proposed structure is promising to handle higher power levels in comparison to the conventional MEMS switches as it has thick metal conductors (25um). In addition, it avoids the "self biasing", [57], problem due to high spring constant of the actuator. The newly developed structure is indeed suitable for integration in large systems and can be easily incorporated in a circuit without adding any extra loads.

3.4.2. Thermally Actuated Multi-Port RF MEMS switches

The proposed concept is a good candidate for integration in large numbers and thus suitable for basic building blocks of switch matrices. This idea is used to develop SP2T and C-type or transfer switch as the main building block for redundancy switch matrices.

A single-pole double-throw (SP2T) thermally actuated switch is presented in Figure 3.26. The switch makes use of TED actuators with an extended rigid silicon nitride arm to transfer the force to the contact point. A bridge over the nitride layer is used to connects the ground lines of the adjacent ports and eliminate the unwanted parasitic modes of the CPW lines. In addition, to reduce the RF substrate loss, a 25μm trench is etched into the substrate.

To verify the concept, a two port measurement is performed, and the results up to 10GHz are illustrated in Figure 3.27. The return loss of the switch is less than -20dB for all the frequency range. The insertion loss is better than 1dB up to 7GHz and less than 1.9dB up to 10GHz. The slightly high insertion loss is attributed to the substrate loss as well as the discontinuity of the ground plane. The use of high resistivity silicon as base substrate and also air bridges on the ground planes to avoid the asymmetry parasitic modes of CPW lines, can significantly improve the performance. Also, the isolation of the switch is measured which is more than 27dB for all the frequency band.

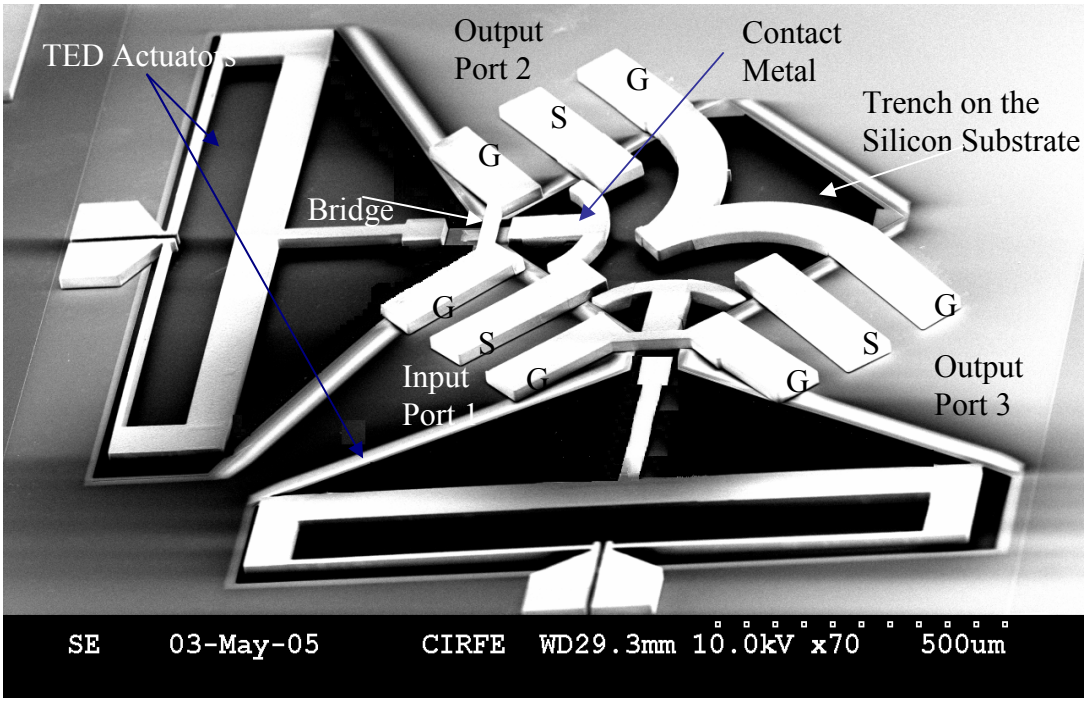

Figure 3.26: Proposed single- port double-throw (SP2T) switch.

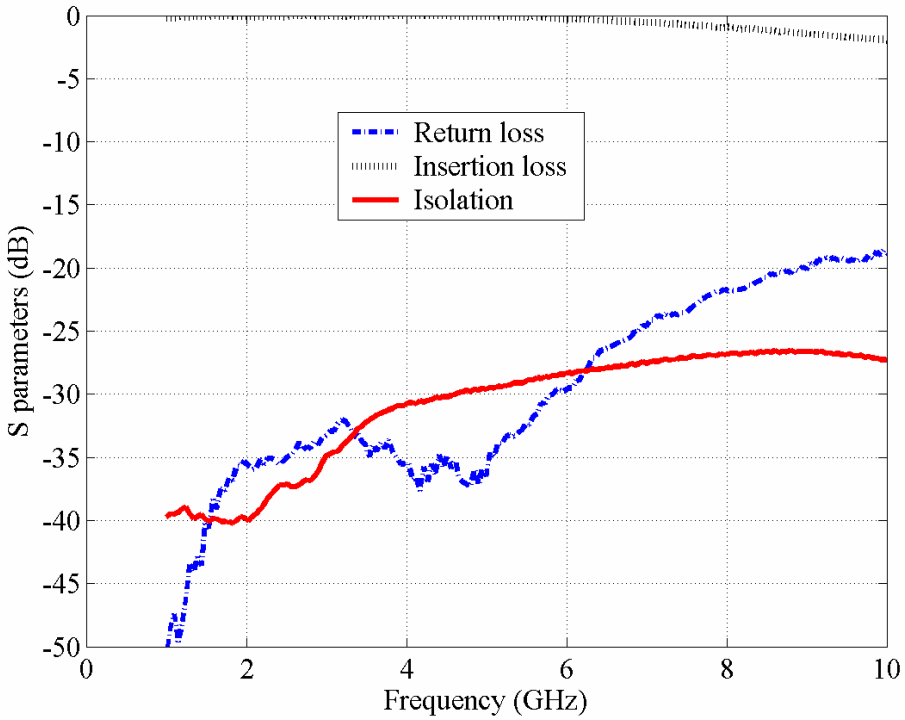

Figure 3.27: Measured results for the proposed SP2T

C-type or transfer switch is another type of multi-port switches that has been investigated. As it was demonstrated in Figure 3.10, the switch has two operational states. In state I, the connection is established between ports 1 and 2, and between ports 3 and 4, and in state II, ports 1 and 4 and ports 2 and 3 are connected. Here, a new configuration as shown in Figure 3.28 is proposed that is based on TED actuators and finite ground CPW lines. A Nickel based TED is used to move a gold covered Ni contact element to turn the switch ON and OFF. In state I, actuators 1 and 3 are excited and move forward to provide a short circuit between ports 1 and 2 and ports 2 and 3. The ground planes of the adjacent ports are connected to reduce unwanted asymmetry CPW modes. In the same way, actuators 2 and 4 are biased to present stat II of the switch. Similar to the previously proposed thermal switches, the actuators are electrically isolated from the RF section of the switch shown in Figure 3.28 (b). This makes it more suitable to be integrated in large switch matrices.

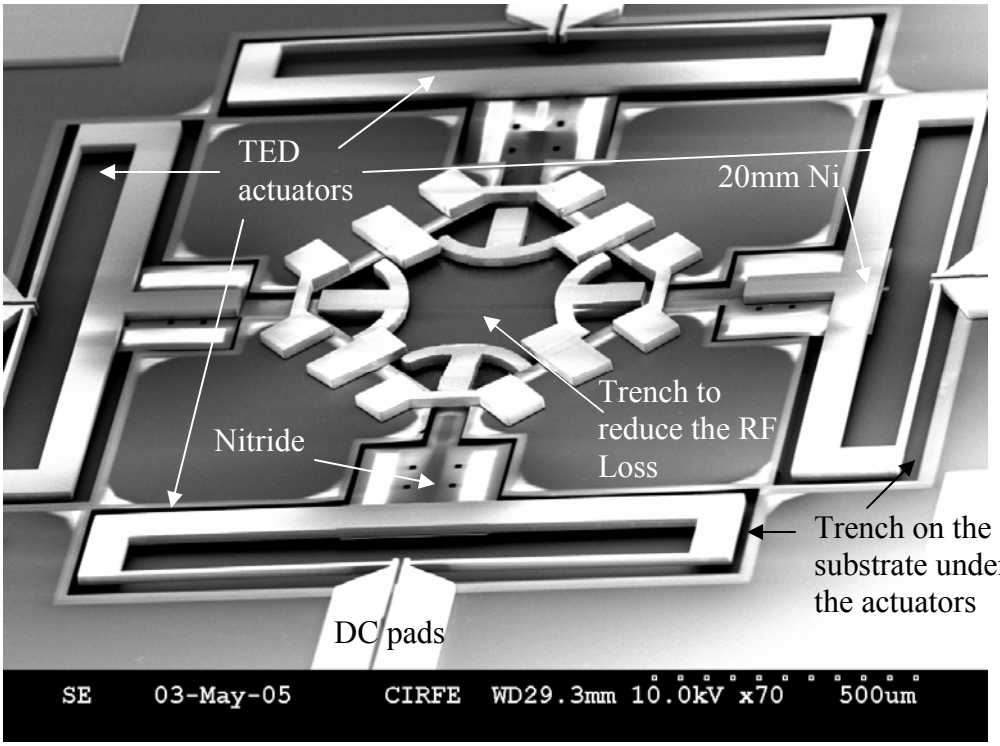

(a)

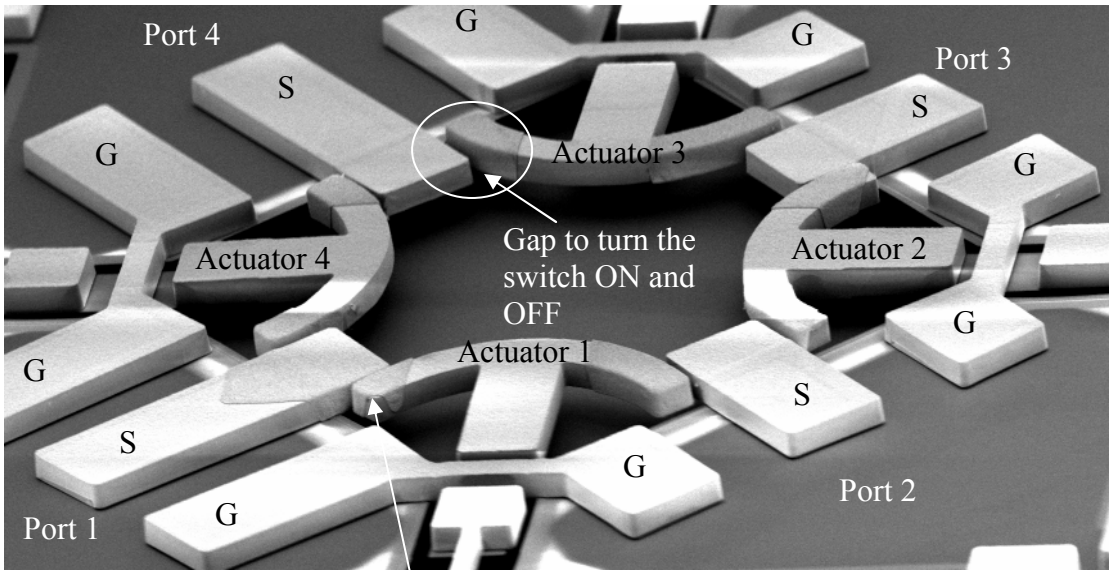

Side wall gold coating on the contact points

(b)

Figure 3.28: (a) Proposed C-type switch and (b) RF section of the proposed switch.

A two port measurement is performed and the results are plotted in Figure 3.29. It shows a return loss of better than -17dB up to 10 GHz and the insertion loss is less than 1 dB at 8GHz. Although, there is a trench under the CPW lines, the slightly high insertion loss at higher frequencies, is attributed to the silicon substrate loss. In addition, the discontinuity of the ground planes induces parasitic odd modes and limits the operating frequency band. Adding more air bridges helps to improve the performance. The switch isolation exceeds 25dB for all the frequency band of interest. Due to the symmetric structure of the switch, the results for state II are identical to that of state I presented in the figure.

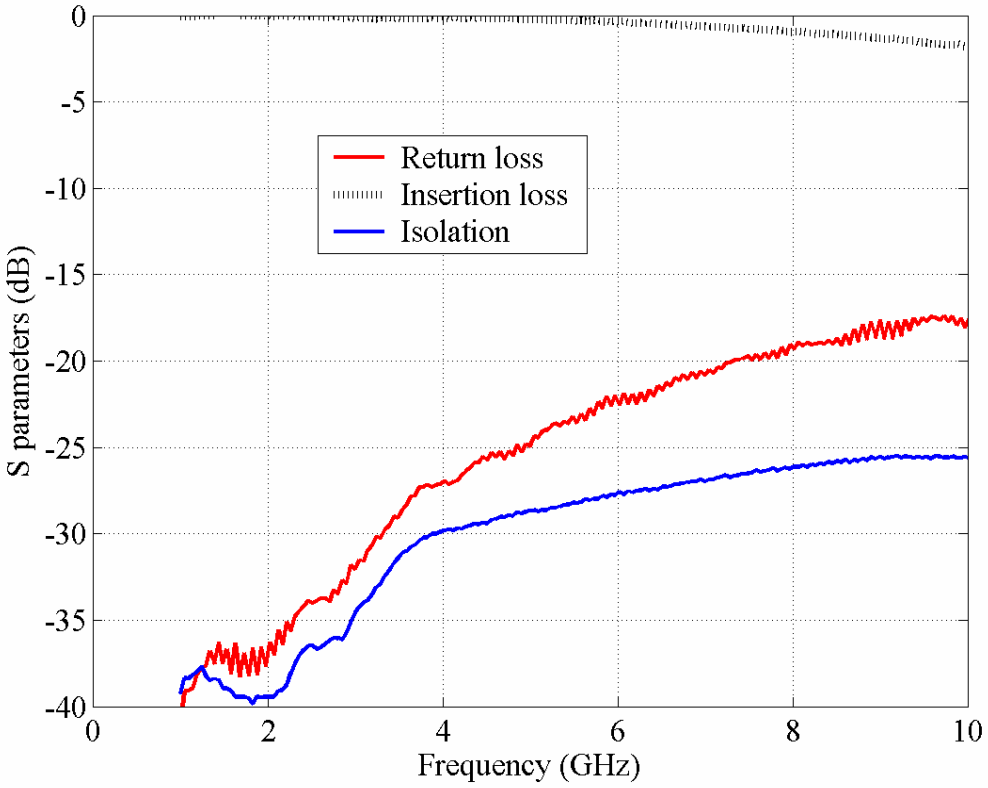

Figure 3.29: Measured S-parameters for the proposed C switch shown in Figure 3.28

3.4.3. Improved Multi-Port RF MEMS Switch

Although the presented switches show good mechanical performance, their RF response can be still improved by using higher resistivity substrate. This modification results in a superior RF performance as explained in this section.

The idea is initially verified by realizing an SPST switch using high resistivity silicon substrate. The design is slightly modified and the RF circuit of the switch is made more compact as shown in Figure 3.30. The RF results shown in Figure 3.31 present an excellent performance. The insertion loss is less than 0.5dB for all the frequency range up to 40GHz with a return loss of better than -15dB. Compared to the previously presented thermal SPST switch in section 3.4.1, not only the loss has drastically decreased but also the operating frequency band has significantly improved. The switch maintains the isolation of better than about 20dB for all the frequency range up to 40GHz.

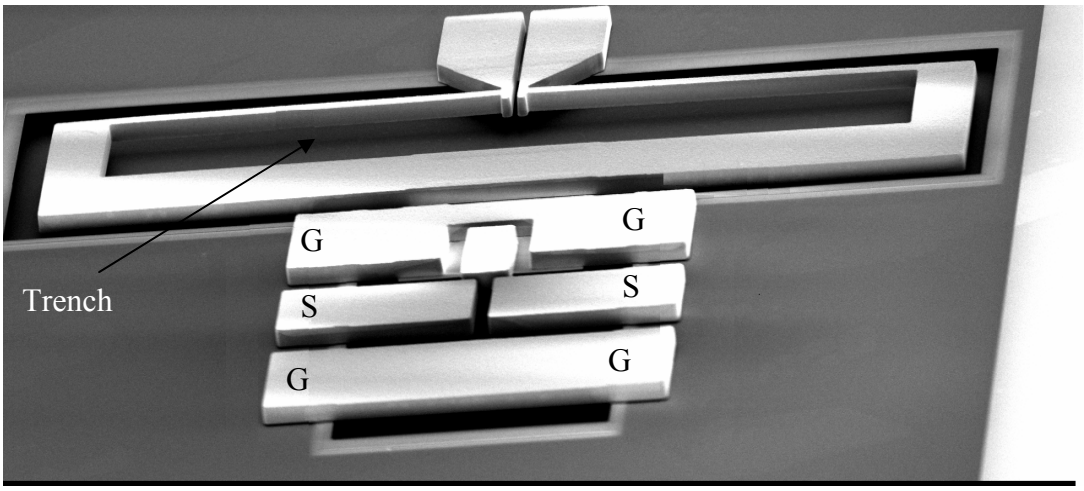

Figure 3.30: Modified design of the proposed SPST thermally actuated RF MEMS switch

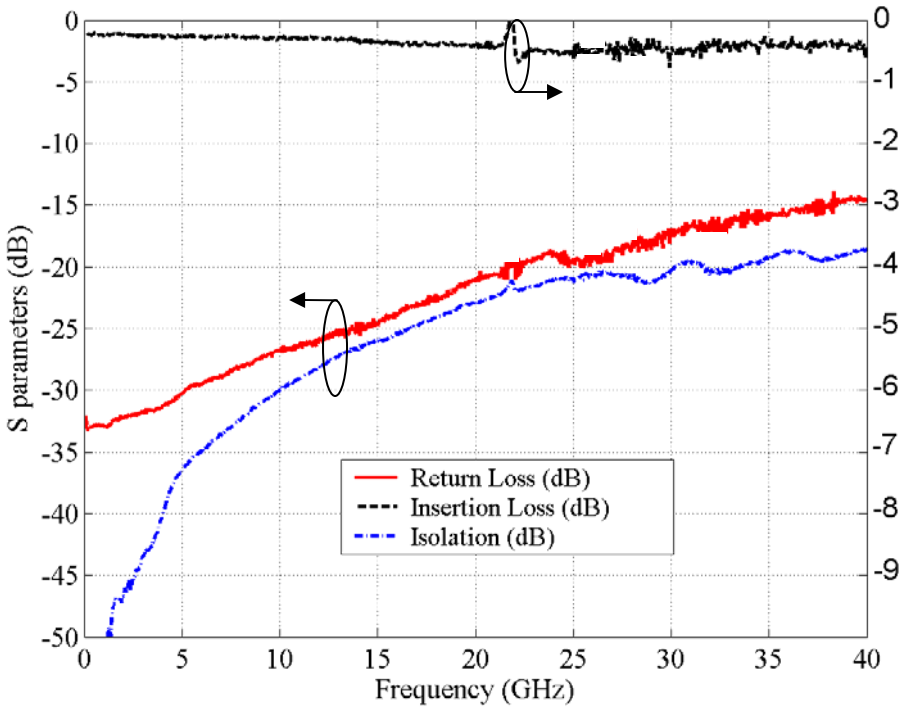

Figure 3.31: Measured results for the proposed design shown in Figure 3.30

The proposed SP2T switch shown in Figure 3.26 makes use of a contact metal that has a round shape. This provides a 90 degrees bend, required to connect the two adjacent ports. However, the amount of the applied force at the contact points is much less than the actuators induced force. This is due to the 45degrees angle of the actual generated force of the actuators and the contact surfaces. To overcome this problem and enhance the switch performance, a new design shown in Figure 3.31 is proposed. In this configuration, the total force of the actuators is transferred to the contact points and thus reducing the contact resistant significantly. Besides, use of high resistivity silicon substrate improves the performance and reduces the RF loss. The results that are illustrated in Figure 3.33**Error! Reference source not found.**, indicate a 0.5 dB insertion loss at 20GHz with a return loss of better than -15dB. The isolation of the switch is better than about 30dB for all the frequency band of interest.

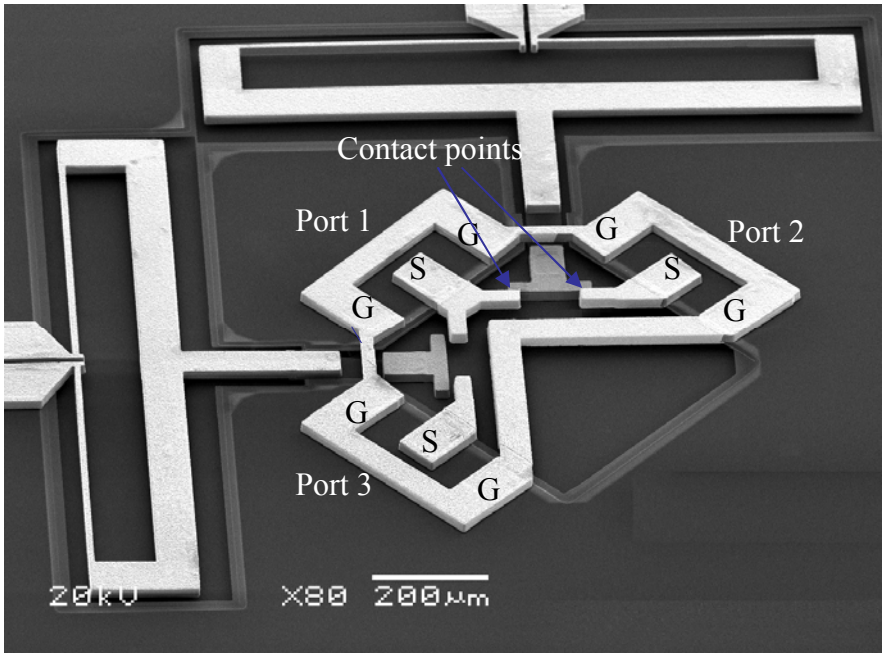

Figure 3.32: Modified design of the propose SP2 thermally actuated RF MEMS switch

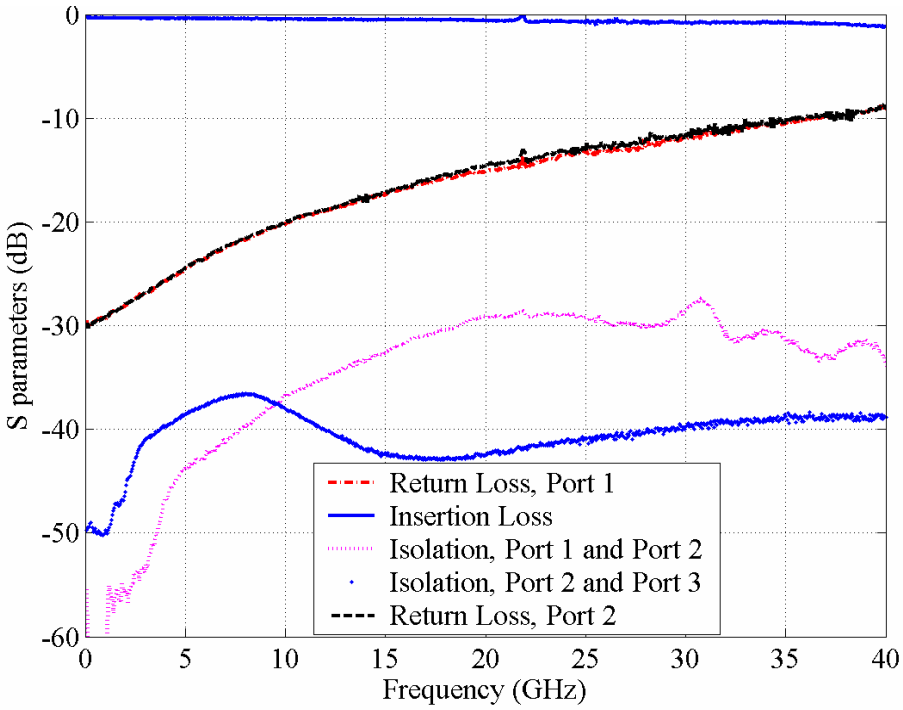

Figure 3.33: Measured results for the proposed design shown in Figure 3.32

This concept is also implemented on C-type switch and shown in Figure 3.34. The force generated on the actuators is directly transferred to the contact points and results in very low contact resistance. Besides, the continuity of the ground lines is maintained to avoid unwanted parasitic CPW modes and obtain wideband performance. The switch comprises two different states while ports 1 and 2, and port 3 and 4, are connected and in the other state ports 1 and 4, and ports 2 and 3, are linked. The results are shown in Figure 3.35 which represent a significant improvement compared to the previously discussed C-type switch. The insertion loss is as low as 0.9dB at 10GHz and 1.5 dB at 30GHz and the isolation is better than 30dB for all the frequency band of interest.

Multi-port nature of these switches and their low insertion loss and high isolation, creates unique devices for the applications with large number of elements. These switches are superb nominees for basic building blocks of redundancy switch matrices in satellite communications.

3.5.Summary

In this chapter, electrostatic and thermal actuators are investigated to develop multi-port RF MEMS switches. Experimental results for novel configurations of SPST, SP2T, SP3T, C-type and R-type MEMS switches are given.

Initially the PolyMUMPs process is used to fabricate the electrostatic switches. To avoid the extensive loss of the silicon based process, the switches are assembled on an alumina substrate using flip chip technology.

The switch designs are optimized and are fabricated monolithically on an alumina substrate at the CIRFE lab at the University of Waterloo. An extensive effort is spent to develop and fine tune the new fabrication process for the proposed switches. This results in a superior performance and substantially increases the fabrication yield.

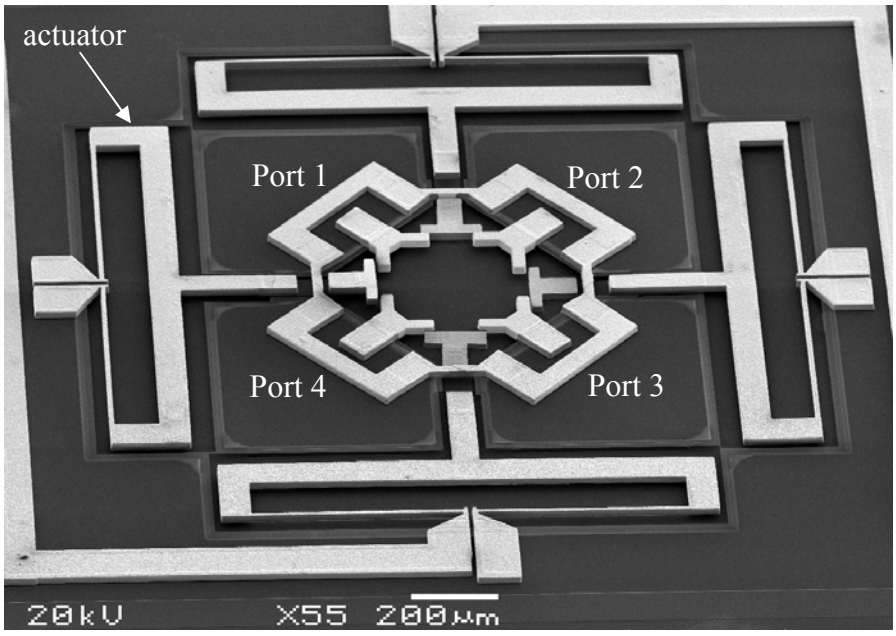

(a)

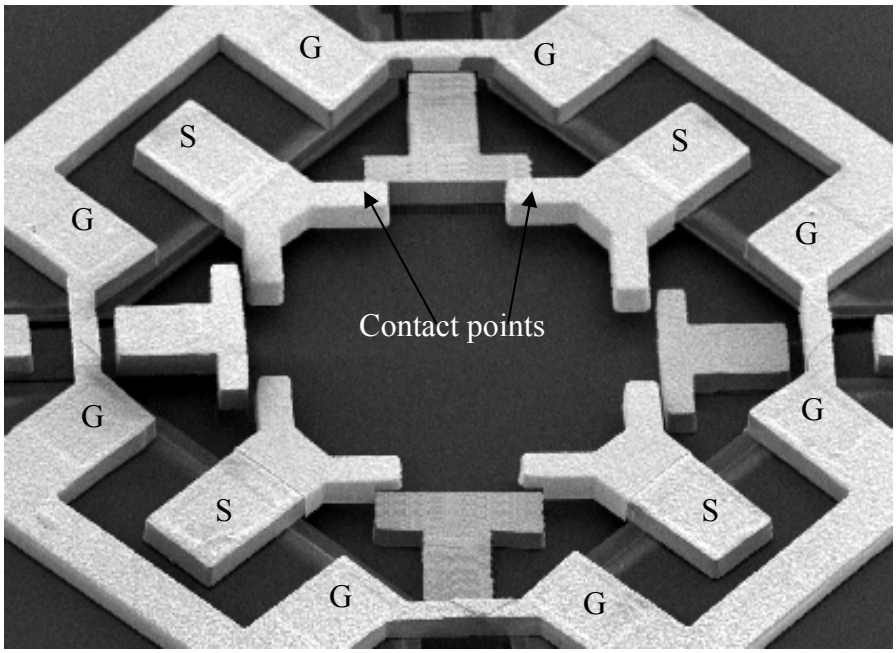

(b)

Figure 3.34: (a) Proposed modified C-type switch and (b) its RF section

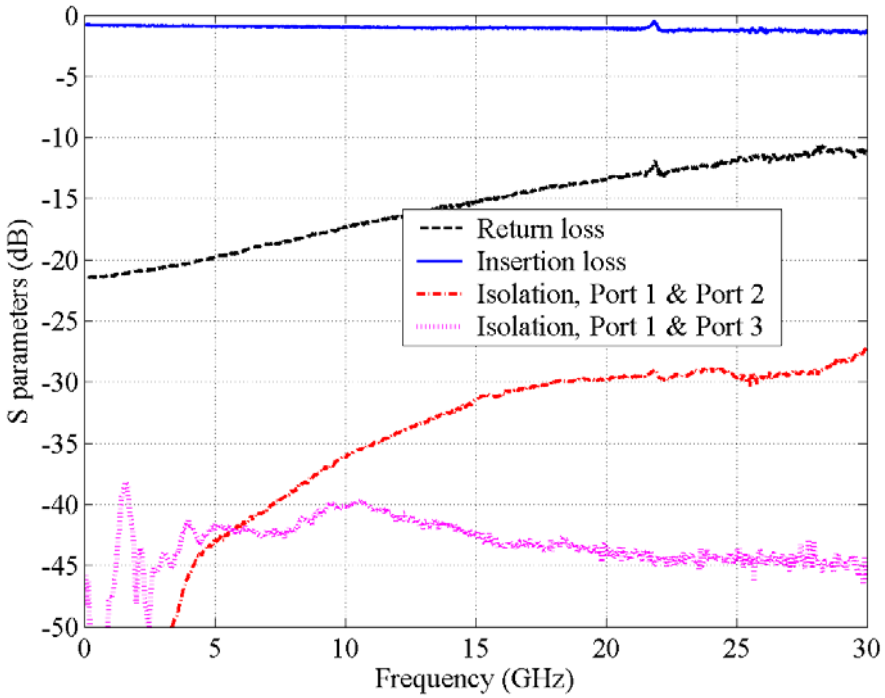

Figure 3.35: Measure results for the C-type switch illustrate at Figure 3.34

In addition, novel thermally actuated switches are developed and new SPST, SP2T and C-type switches are designed, analyzed and fabricated. These units are fabricated monolithically with well established Metal MUMPs process and make use of well-known metal thermal actuators (TED) which consume very low power. The switches are investigated and tested at three different situations: 1) room condition, 2) vacuum and room temperature and 3) a very low temperature of 77K degrees. The prototype units behave very well under all conditions and show a good mechanical and RF performance.

Chapter 4

3D Multi-Port RF MEMS Switches

4.1. Introduction

Another key area which has not been adequately addresses yet by MEMS researchers is the development of millimetre-wave switches. These switches are applied in communications that cover a wide frequency range of 30GHz to 300GHz.

In recent years there has been a growing interest in wireless communications for indoor applications as well as global coverage by mobile phones. Since millimeter-wave bands are less congested than the bands at lower frequencies, they can offer wide bandwidths for multi-channel communications. Typically, these types of systems need many switches in the form of switch matrices to provide the connectivity. Millimeter-waves also play an important role in the automobile industry. Adaptive cruise control (ACC) systems employing 77GHz car radars have recently become available in luxury models [58]. Automotive radar for collision avoidance is another field of active research in the frequency range of the V band and W band. They require switches to be activated in the case of emergency. In addition, frequencies higher than 100GHz play an important role in the military and imaging systems of radio astronomy.

In these applications, high performance switches, suitable for low cost microwave integrated circuit production are strongly required. PIN diode and InP HEMT switches are popular at millimeter wave bands up to 100 GHz [59]. However they are lossy (~ 3db insertion loss), narrow band (~5% BW) and exhibit poor isolation (~ -18dB) [60]. To achieve a good RF performance as high as few hundred gigahertzes, waveguide switches

could be used. Figure 4.1 is a photo of a motorized waveguide switch that is currently available in the market and exhibits an excellent performance as high as 220GHz [60] with isolation higher than 50dB and approximately 40% BW. The switching is accomplished through a make or break in the waveguide path by a control signal activating a rotary electrical motor. In contrast with PIN diode, the switches have capability of handling high power. However, motorized waveguide switches are heavy and bulky and require new solution especially when the mass reduction is a critical issue.

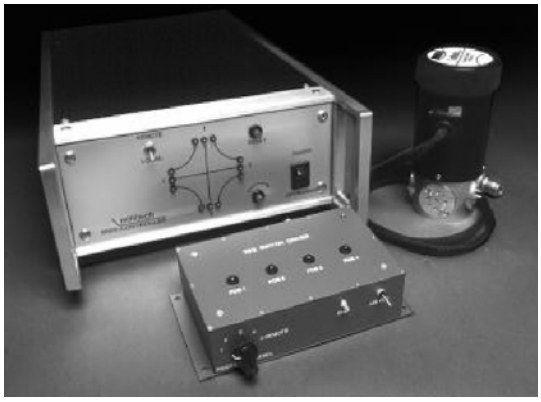

Figure 4.1: Motorized waveguide switch for the frequency range of 18GHz to 220GHz [60] .

RF MEMS switches are good candidates to substitute for the existing mechanical switches due to their superior RF performance and miniaturized dimensions [57]. However, their high actuating voltage and low power handling are still major obstacles. The “stand off voltage” or “self biasing” of electrostatic MEMS switches, defined as the maximum RF voltage before pulling the beam down, is one of the main limiting factors. In additions, a stiction problem due to the charge trapping in the dielectric layer between the electrodes is also a challenge to switch reliability.

In this chapter, we introduce unique RF MEMS 3D switches that promise to combine the advantageous properties of both 3D transmission lines and MEMS switches. It is based on waveguide and coaxial lines with inner integrated MEMS vertical actuators to create the ON and OFF states. It provides the opportunity to have high power levels and excellent RF performance, but avoiding the heavy and bulky motors of the

conventional mechanical switches.

4.2. RF MEMS Ridge Waveguide Switch

Figure 4.2 offers a schematic of the proposed DC-contact shunt MEMS waveguide switch. It consists of a ridge waveguide incorporated with MEMS actuators. The dimensions of the ridge waveguide are: a=10.8 mm and b=4.4mm. The ridge width and height are 1.6mm and 4mm respectively, which leaves a 400μm gap on the bottom side of the waveguide. It is well known that the electric field has a strong intensity in this gap along the ridge where the MEMS plates are located. When the plates are in the horizontal position the switch is ON and the wave propagates through the waveguide. By moving the plate to the vertical position, wave propagation is blocked and the switch

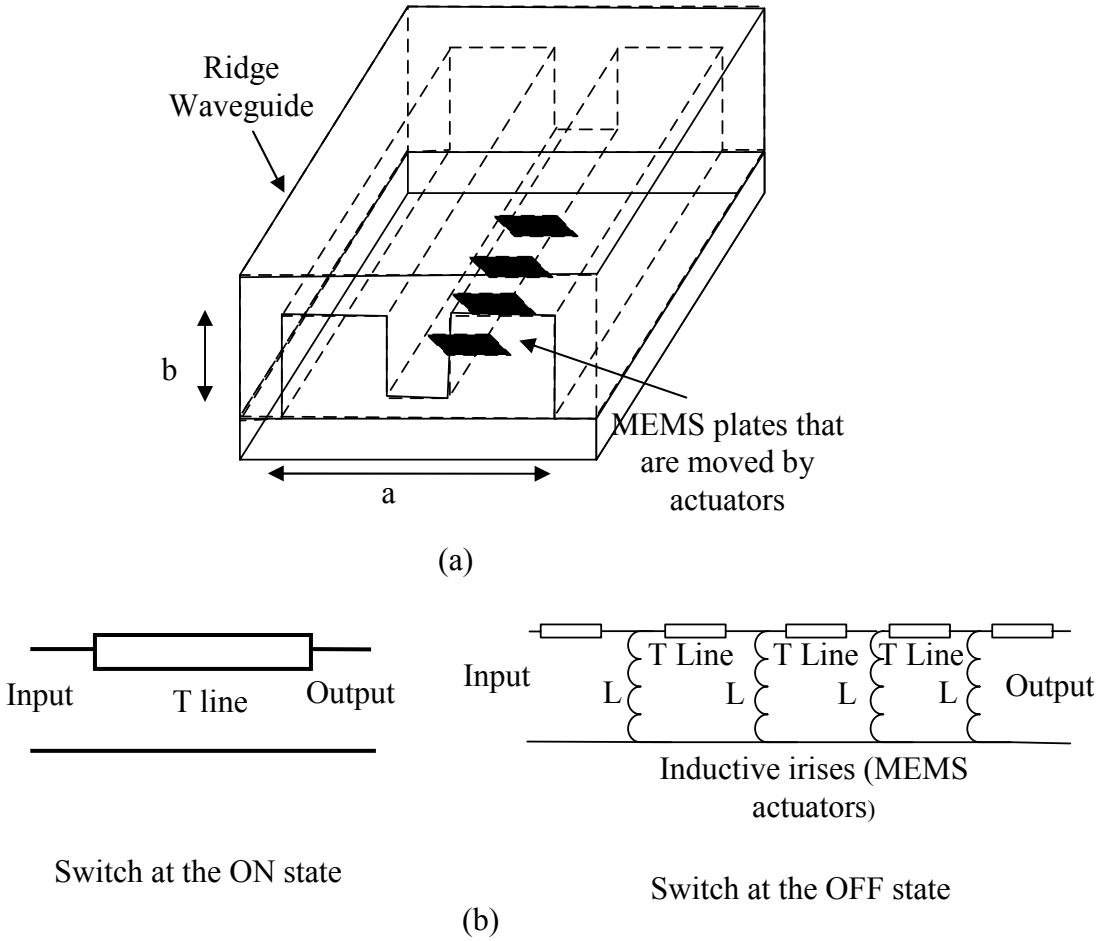

Figure 4.2 (a) Waveguide switch conceptual schematic and (b) circuit model.

turns OFF.

Several of these MEMS plates have been used to obtain a good OFF state switch isolation. The plates act as parallel irises inside the waveguide. For the dominant mode, the equivalent circuit of each actuator is simply an inductor shunting the waveguide. The entire switch circuit model is presented in Figure 4.2(b). The MEMS actuators are substituted with 130pH inductors whereas the waveguide is represented by a transmission line. Figure 4.3 is a comparison between the isolation results of the EM HFSS model and those of the circuit model in Figure 4.2. A good agreement is observed. It is clear that an isolation of more than 40 dB could be achieved for the ideal contact over the satellite Ku band (12-15 GHz).

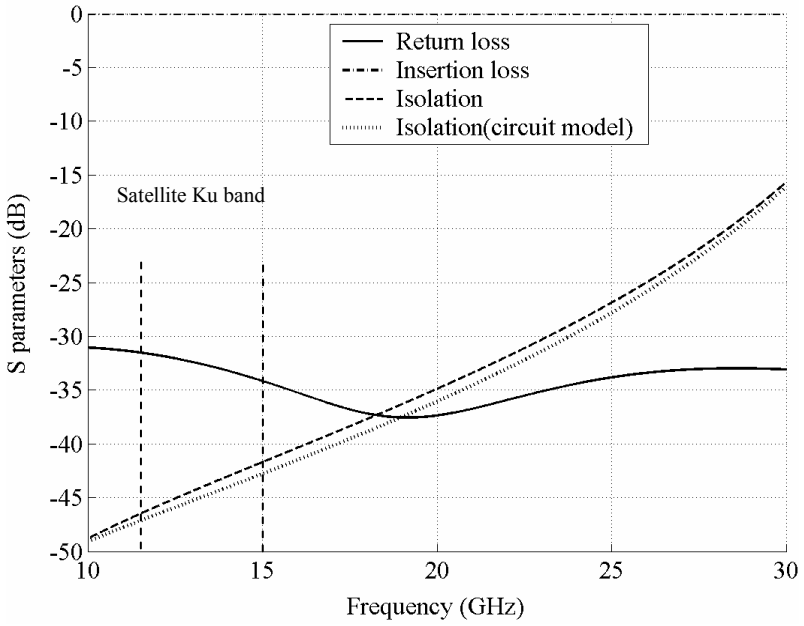

Figure 4.3. Ridge waveguide switch performance based on the HFSS Simulation and circuit model.

4.2.1. Single-Pole Single-Throw RF MEMS Waveguide Switch

The proposed waveguide switch involves a large plate that is used to block the waveguide in the "OFF" state. In the "ON" state, this plate should be entirely removed

from the signal path, to a position that is coincident with the waveguide surface. For an SPST switch, the thermal plastic deformation assembly (TPDA) method is used to assemble a large plate to an orientation orthogonal to the substrate [61].

Figure 4.4 graphically depicts the principle behind the TPDA method. Initially, a bimorph of gold and polysilicon fabricated by using the PolyMUMPs surface micromachining process assumes a planar geometry. When the temperature is increased, the difference in the thermal expansion coefficients results in a deflection of the bimorph in the direction shown in Figure 4.4(b). At high temperatures (~200 C) the metal layer yields under large compressive stresses from actuation. Upon relaxation as the temperature is lowered, the bimorph assumes a new geometry due to plastic deformation (Figure 4.4(c)). When a current is passed through the beam, joule heating actuates the bimorph to return to its initial position [62].

The geometry in Figure 4.5 provides a large out-of-plane rotation with a small footprint, and can be actuated with low voltages of ~10V and a current of 5mA to rotate 90 degrees in less than 1 millisecond. This is accomplished by cascading several of the bimorphs by using a staggered helical geometry. The deflected tip of a bimorph is connected to another bimorph using a passive beam, and this process is repeated to obtain the desired motion by adding the deflections in series [63].

The payload of the actuator, shown in Figure 4.5, is 100μm × 200μm × 2μm plate. The waveguide switch makes use of the same actuators with a much larger payload, a 400μm × 2500μm × 2μm plate, as shown in Figure 4.6(a). Figure 4.6(b) displays four MEMS plates in the vertical state that are used for the waveguide switch. After initial assembly, the application of s DC voltage rotates the plates to the horizontal state acting as a flat gold surface at the inner bottom side of the waveguide. The gold coating of the silicon surface (actuators base substrate) is instrumental in avoiding signal loss in the waveguide.

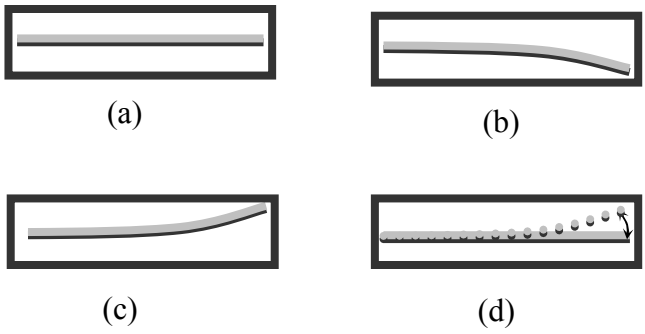

Figure 4.4: Device (a) initial position, (b) exposed to higher temperatures and stress: ~200 degrees C, ~20minutes metal yields, (c) relaxation, new stress mismatch results in deformed geometry and (d) low voltage can be used to actuate the bimorphs to return to their initial position [63].

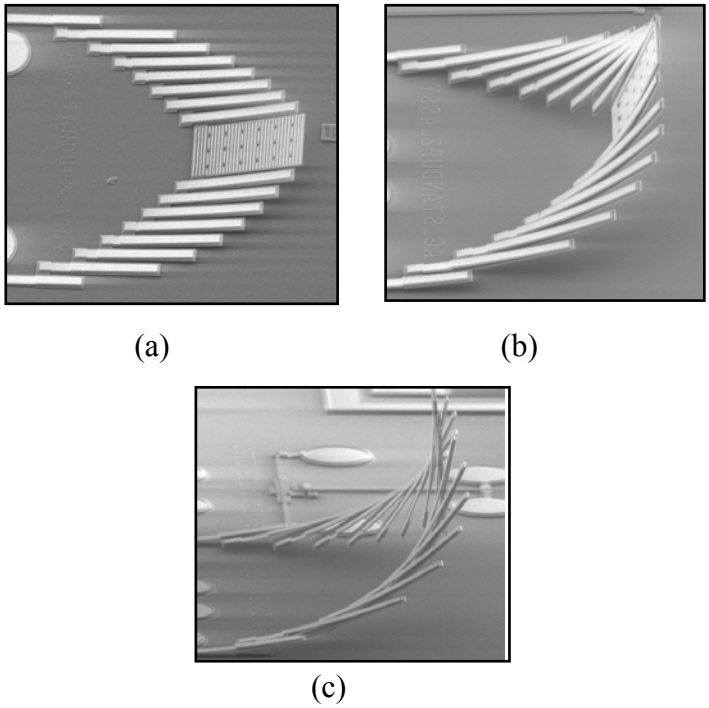

Figure 4.5: Cascaded rotary actuator at (a) initial position, (b) partially assembled and (c) fully deformed position [63]..

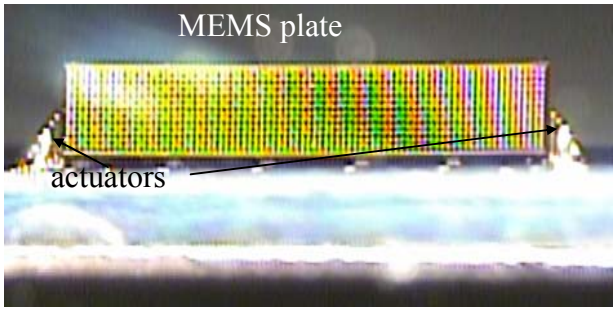

(a)

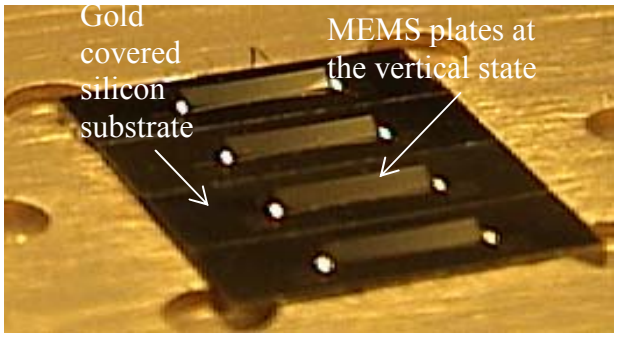

(b)

Figure 4.6 (a) 2.5mm×0.4mm gold covered plate moved by the actuators, (b) four MEMS plates are incorporated at the bottom plate of the waveguide.

4.2.1.1.Single-Pole Single-Throw (SPST) MEMS Waveguide Switch With Waveguide Transition

To integrate the waveguide switch in a system, a ridge waveguide to standard waveguide transition is needed. Figure 4.7 shows a switch schematic that consists of a single ridge waveguide in the centre and two quarter-wave multi-section impedance transformers on both ends. The total length of the switch is 26mm which includes 10mm of the central ridge waveguide section. The switch is designed to match to a WR62 waveguide interface.

The switch is manufactured in two detached top and bottom parts that facilitates the assembly of the MEMS actuators. As shown in Figure 4.8, the MEMS actuators are integrated in the bottom plate and the waveguide channels and ridge are fabricated on the

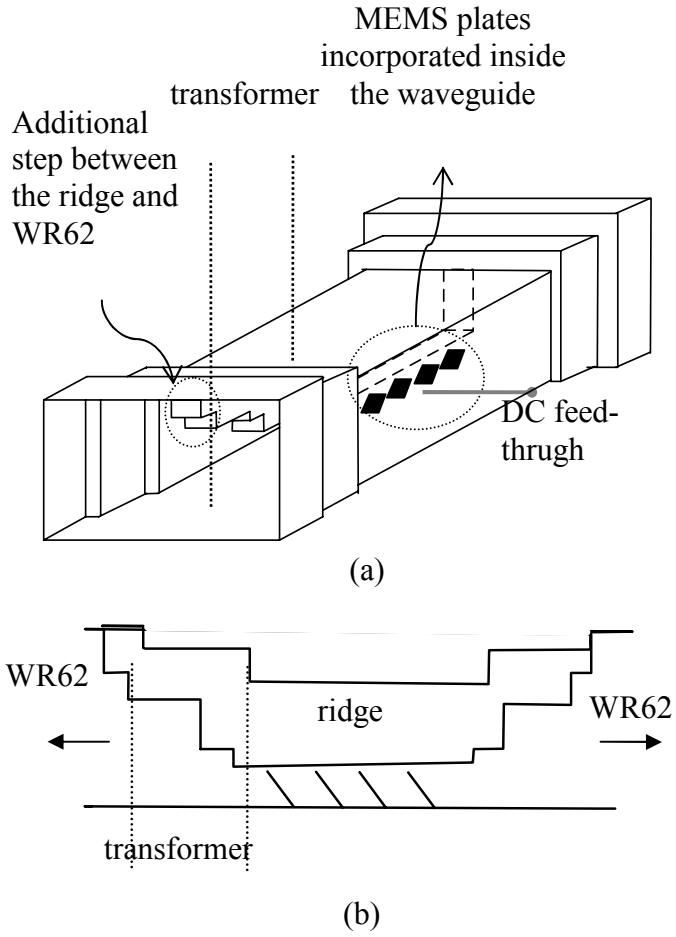

Figure 4.7: Schematic of the proposed MEMS waveguide switch (a) 3-D and (b) cross section.

top cover. This helps to fabricate the structure by a well established machining process followed by gold plating.

To evaluate the fabricated waveguide and the transitions performance, the simulation and measurement data are compared in Figure 4.9. For measurement purposes, a flat gold plate is used instead of the MEMS chip. The small discrepancy is attributed to the machining error and to the discontinuity created by the gold plate.

After the integration of the MEMS actuators, a two-port measurement on the waveguide switch is performed and the results are illustrated in Figure 4.10. This figure shows an isolation of better than 18 dB and a return loss better than 15 dB over a 1 GHz

bandwidth (13.2 to 14.2 GHz). An insertion loss of 2.5 dB which is much higher than the measured insertion loss, shown in Figure 4.9 for the ideal gold plate, is observed. The high insertion loss is attributed to the existing small gaps between the silicon substrates as four separate chips are used. It is also attributed to the substrate loss because only the top surface of the silicon chips is coated with gold.

For higher frequency range and millimeter wave applications, the bottom part and the MEMS actuators could be monolithically fabricated. The top ridge waveguide cover could be done through silicon wafer deep Reactive Ion Etching (RIE) followed by gold evaporation. Then well known wafer bonding techniques are used to assemble the entire waveguide switch.

.

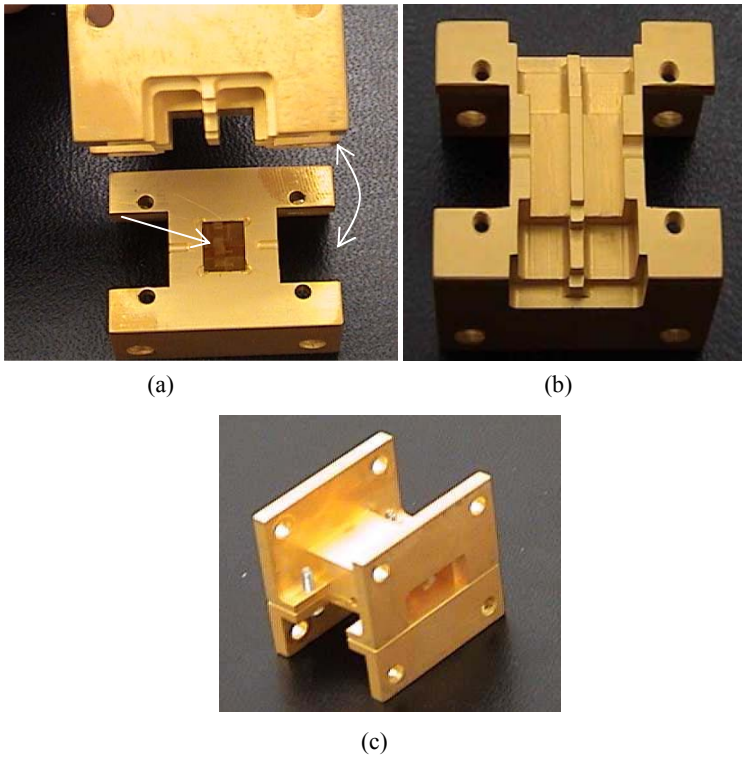

(a) (b)

(c)

Figure 4.8: Fabricated waveguide switch (a) bottom plate, (b) top cover, and (c) assembled on top of each other.

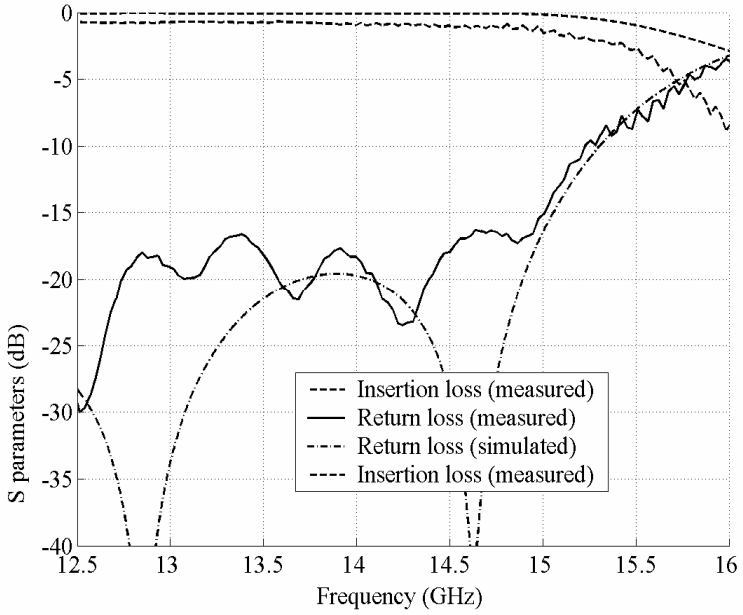

Figure 4.9: Measured and simulated results for the ridge waveguide structure with the transitions.

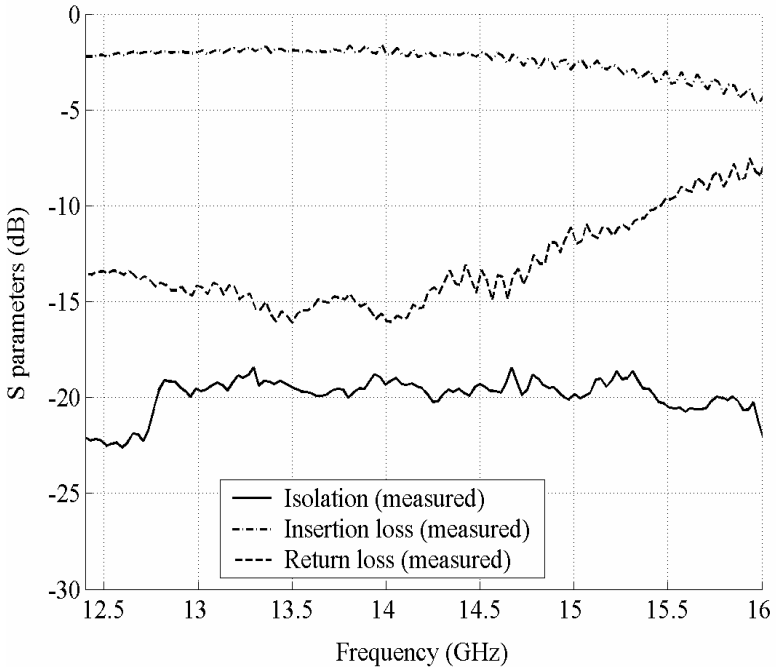

Figure 4.10. Measured results for the waveguide switch shown in Figure 4.7.

4.2.1.2.Wideband Single-Pole Single-Throw (SPST) MEMS waveguide switch with CPW transition

Although the ridge waveguide switch shown in Figure 4.2 is suitable for wideband applications, the use of the waveguide impedance transformer limits the operating frequency band. To overcome this problem and evaluate the wideband performance of the waveguide switch, we use a ridge waveguide to coplanar line transition to cover both Ku and K bands. A conceptual schematic of the proposed idea is shown in Figure 4.11.

To realize this switch, the MEMS plates and actuators are integrated on the bottom plate and the waveguide channel and ridge are fabricated on the top cover, as seen in Figure 4.12. A microstrip line is used as an interface to transform the ridge waveguide mode to the CPW mode. When the ridge waveguide and the circuit board are clamped together, the ridge makes contact with the microstrip signal line. An extra extension of the ridge is used to achieve a good contact between the waveguide and the planar circuit. The lower broad wall of the ridge waveguide is extended to form the microstrip ground plane. Then an in line microstrip to CPW transition is used. Plated through holes are utilized to connect the CPW ground planes to the waveguide bottom surface. For measurement purposes, the widths of the lines are further narrowed to match the 150μm probe pitch.

To minimize the mismatch between the waveguide and microstrip line for over the band of interest, the ridge waveguide characteristics impedance is designed to be around 50Ω. This leads to a ridge width of 1.6mm, height of 4mm, and the waveguide channel dimensions of 10.8mm×4.4mm. To assure minimum field perturbation during the waveguide to microstrip mode transition, a low k substrate is employed. For a 15mil (~254μm) quartz substrate with ε_r=3.8, the microstrip line width is 0.8mm. It is observed that adding an inductive section to the microstip line improves the performance by compensating for the fringing capacitance of the ridge at the transition.

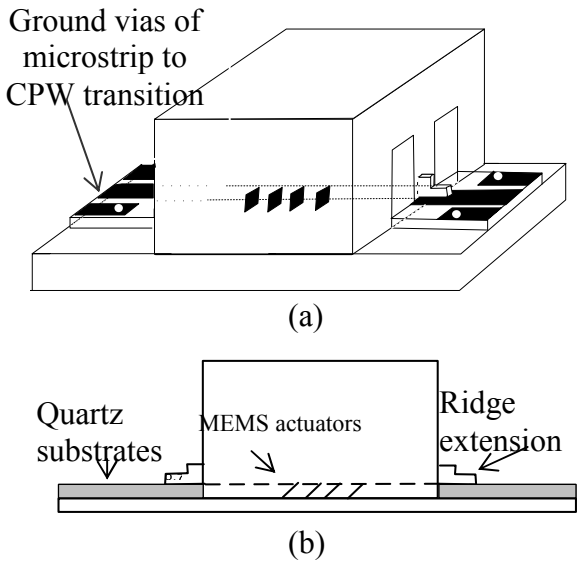

Figure 4.11: Schematic of the proposed MEMS Switch (a) 3D view and (b) cross view.

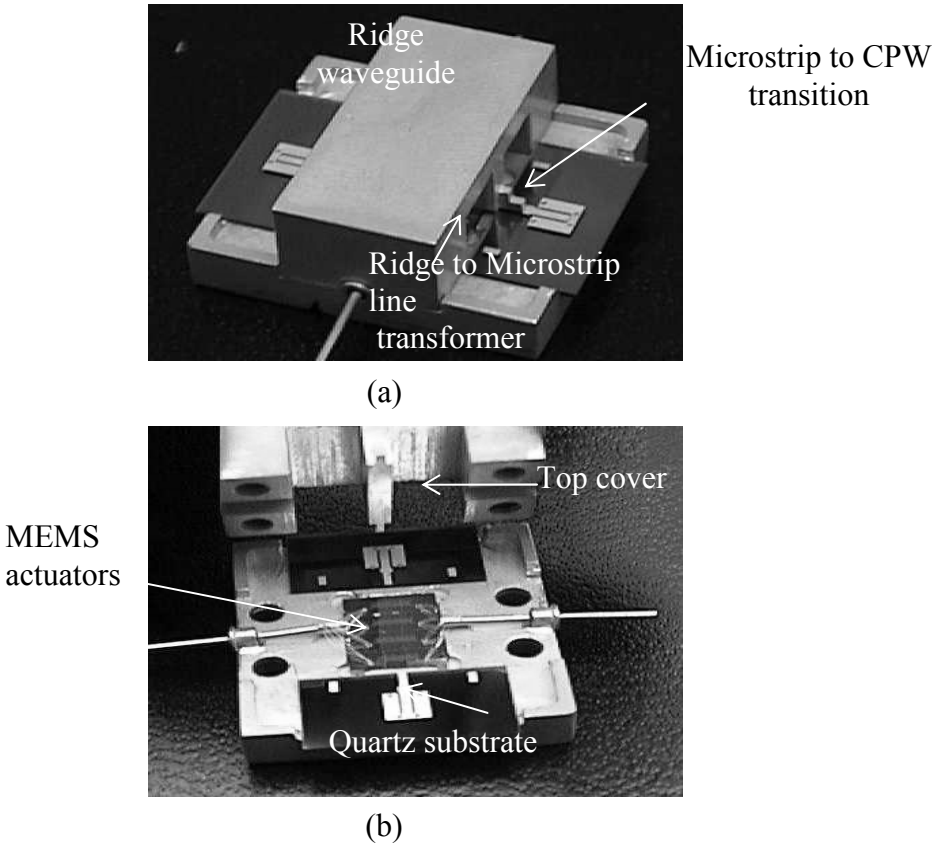

Figure 4.12: MEMS waveguide switch with transition to CPW (a) total structure and (b) top and bottom plates.

To verify the performance of the ridge waveguide to the CPW transitions, the MEMS chips are substituted by a flat gold plate and a 2-port measurement is performed. The results are presented in Figure 4.13. After integrating the actuators in the waveguide, the switch performance is also measured and is shown in Figure 4.14. This proves that the switch in Figure 4.2 has a great potential for wide band applications. A return loss close to 15dB is achieved over a 12-30 GHz band. The insertion loss of the switch is between 1 to 2.8dB over the Ku and the K band which is attributed to the gaps between the MEMS actuators. The insertion loss can be significantly improved by realizing the four MEMS actuators on one chip. The isolation of the switch is also measured and is reflected in Figure 4.14. The deviation between the measured data and the theoretical results shown in Figure 4.3 is due to the non ideal contact of the actuators and the ridge surface. However, the measured results of the initial prototype are encouraging and demonstrate that the switch is promissing for wideband applications.

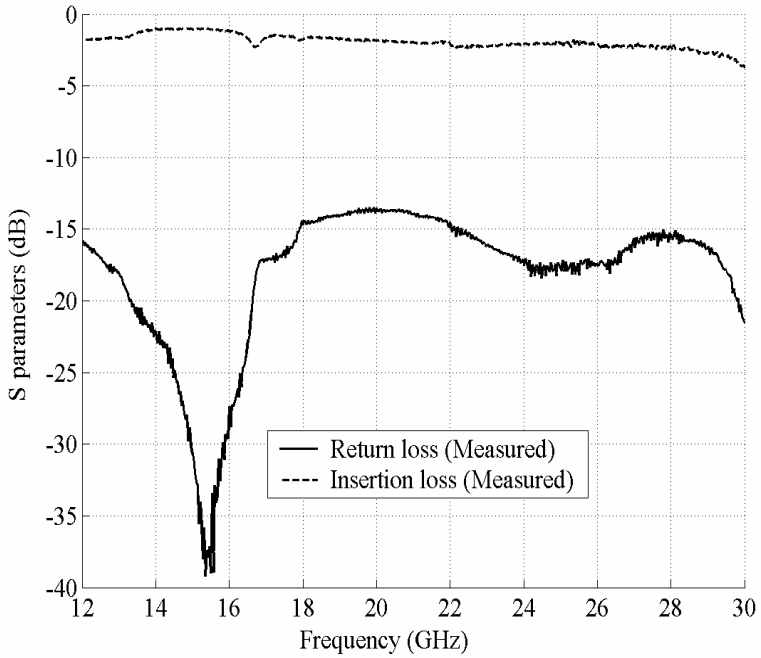

Figure 4.13: Ridge waveguide performance with the CPW transitions.

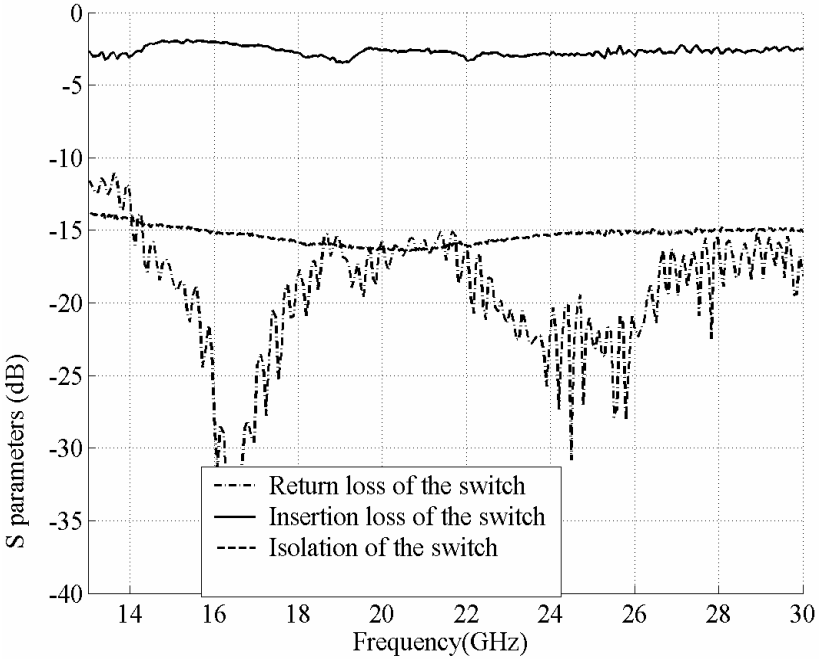

Figure 4.14: Measured data the switch shown in Figure 4.12.

4.2.1.3. MEMS Waveguide Switch Power Handling Analysis

Although traditional MEMS switches have demonstrated superior RF performance in terms of insertion loss and DC power consumption, their power handling capability is very limited. To date, the vast majority of the studies have been focused on the MEMS switch applications and few authors have addressed the power handling concerns [64]-[66]. In this section, a theoretical and experimental study that addresses the different power limiting factors of our proposed switch is provided.

A. ON state

When the switch is in the ON state, the MEMS plates are in a position which coincides with the bottom surface of the waveguide. In this situation, the main concern is the switch self actuation problem which is discussed next.

Figure 4.15 illustrates the electric field distribution for the dominant mode of the ridge waveguide. It is clear that the electric field mainly concentrates between the ridge and the MEMS plates. The resultant potential difference between the ridge and the MEMS plates induces a force on the plates toward the ridge that can be modeled by parallel plate force as follows [57]:

$$F_{RF} = \frac{\varepsilon A}{2g^2}\left(\frac{V_o}{\sqrt{2}}\right)^2(1+\cos(2\omega t)) \tag{4.1}$$

where g is the gap between the ridge and the MEMS plates and A is the area of the plates. It should be noted that the high frequency component of the force does not move the plates and only the constant portion of that may affect the switch functionality. Thus, the applied force is equal to that of the two parallel plates with a voltage of $V_o/\sqrt{2}$ and an equivalent area of *A*. Due to the large fringing field generated around the ridge, this area is not equal to the physical area. A numerical electrostatic simulator, Maxwell Q3D, is used to calculate the overall capacitance and also the equivalent area A_{eq}. For a ridge thickness of 4mm and a width of 1.6mm, the equivalent area is $A_{eq} \approx 3.8A_{physical}$, where $A_{physical}$ is $1600\mu m \times 400\mu m$ (the ridge's and the MEMS plate's common area). It should be noted that this calculation is based on a 400μm constant gap between the two parallel plates. Therefore, the induced force can be calculated from:

$$F_{RF} = \varepsilon\frac{3.8A_{physical}}{2g^2}\left(\frac{V_o}{\sqrt{2}}\right)^2 \tag{4.2}$$

Additionally, according to the idea of the transmission line (TL) theory presented in [57] and [65], the potential difference V_o, for 10W input power is about 31volts. Following this procedure, the induced force to the actuator from the RF signal is 33nN

for a 10W input power and 165nNfor a 50W input power. This force is comparable to the MEMS plate gravity force which is about 78nN but it is far below the micro Newton range force that is applied through thermal actuators.

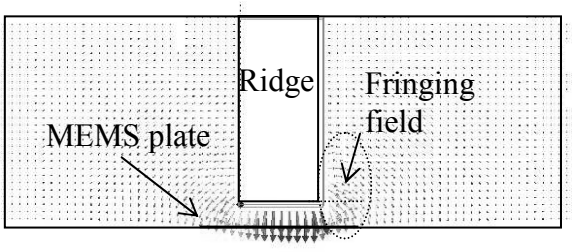

Figure 4.15: Field distribution for the dominant mode of the waveguide switch.

To verify the concept, a high power measurement is carried out on the waveguide switch (as denoted in Figure 4.16), for the ON state. A 14GHz signal is generated in the synthesizer and is amplified in a 20W Varian amplifier with a built-in isolator. The signal is guided to the switch under test through a 20dB coupler. A small portion of the signal is used to record the power by using a power sensor and power meter. Another coupler, power sensor and power meter is used to measure the switch output power. The switch is tested up to 13 Watts with no major change in the RF performance. Only a small increase in the insertion loss is observed which is attributed to the increase of the loss as the switch is heated. The 13 Watts value is the power limit that is obtained by using the existing setup in our lab.

The results indicate that the proposed switch does not suffer from the self biasing voltage problem which is one of the main RF power limiting factors of the existing switches. Despite the fact that the equivalent area of the parallel plates ($1600\mu m \times 400\mu m \times 3.8$) are much larger than that of the existing MEMS switches ($\approx 100\mu m \times 100\mu m$ [57]), the large gap allows significantly higher power handling levels.

For high frequency ranges, (100 to 200 GHz) one can still maintain a relatively large gap (50 -100 μm) which makes it possible to construct high frequency, high power MEMS switches.

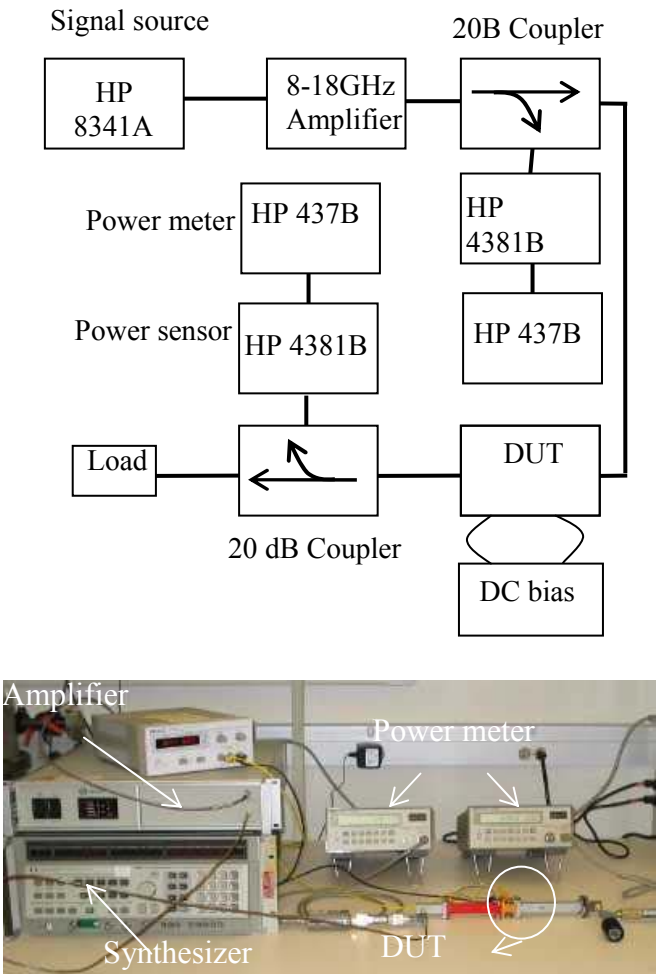

Figure 4.16: Power measurement setup.

B. OFF state

As mentioned before, the MEMS plates in the OFF state act as inductors which shunts the switch. For high power applications, the current passing through the plates can exceed the gold critical current density damaging the switch. However, this problem is less pronounced in the proposed switch, since the current (depicted in Figure 4.17) does not peak up at the edges as in the case of the CPW and microstrip MEMS switches.

Having neglected the mutual effects of the actuators, it can be assumed that each MEMS plate provides one quarter of the total measured isolation, as signified in Figure

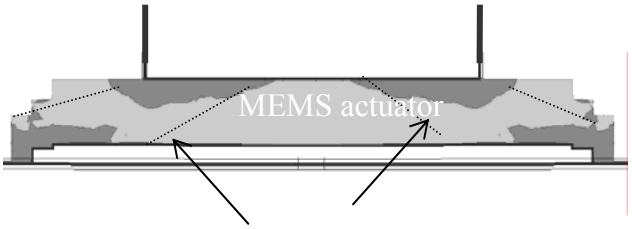

Figure 4.17: RF MEMS actuator model and its surface current distribution inside the waveguide in the OFF state.

4.10. According to the TL theory, this results in 44% of the total short circuit current being conducted in the first MEMS plate which makes it the most vulnerable actuator in the joule heating issue. Considering the skin depth of the gold, for an input power of 1 ,10 and 50 W, the resultant current density is 0.01, 0.03, 0.07 MA/cm^2 respectively. These values are far below the critical current density of gold (0.5MA/cm^2) proving that in this power range joule heating is not the limiting factor [62]. The same power test setup in Figure 4.16 is adapted to evaluate the switch power handling capability in the OFF state. As the vast majority of the current (44%) passes through the first actuator, only one of the actuators is assembled to turn the switch OFF. The measured isolation does not change as the input power is increased from 1W to 13W. The experiment is repeated several times providing consistent results.

Although the waveguide nature of the switch solves some of the concerns related to the MEMS switches, the use of thermal actuators could be one of the limiting factors. The plastic deformable actuators life time under the high power condition is considerably reduced. This is due to the change in the residual stress of the actuators, which leads to a significant change in the actuating voltage.

4.2.2. Multi-Port RF MEMS Waveguide Switch

To provide redundancy schemes and improve the reliability of both receive and transmit subsystems, satellite payload systems employ sophisticated switch matrices. The basic building blocks of such switch matrices are the C-type switches in Figure 3.10.

The use of multi-port switches rather than simple SPST switches considerably simplifies the integration problem. It is the objective of this section to present the new idea of an integrated multi-port MEMS-based waveguide C-type switch for satellite redundancy switch matrix applications. Here, the new switch configuration takes advantage of unique sets of bi-layer electrostatic actuators. These switches offer an excellent RF performance with no DC power consumption which is a key requirement for satellite applications.

For this purpose, a unique set of electrostatic bi-layer curled actuators are designed and fabricated using PolyMUMPs surface micromachining process [67]. The thermally plastic deformation assembly (TPDA) method [63] is used for the initial assembly of the beams; afterwards, electrostatic voltage is used to roll the beams up and down.

Figure 4.17 (a) shows the fabricated actuators composed of a 1.5μm of thick poly silicon and a 0.5 μm gold layer on top. The beam is approximately 100 μm in width and 1500 μm in length. Initially, after the release, the bimorph of gold and poly silicon assumes almost a planar geometry. At the expose to higher temperature (~200 degrees for 10 min), the metal yields and upon relaxation, a new stress mismatch results in a deformed beam toward the gold layer (top layer). This results in a curled beam as illustrated in Figure 4.17(b). Another polysilicon layer (poly0) under the beam is used as the electrode layer. To prevent the beam from collapsing to the bottom electrode, two stoppers steps at both side edges of the beams are utilized [71] . At the down position, these two steps contact the lower surface of the chip and stop the beam from unwanted collapse to the electrodes underneath. The measurement results demonstrate a required voltage of about 20 volts to roll the beam down. The actuation mechanisms of the bi-layer beams are similar to that of Lincoln Lab tri-layer beam used for an SPST switch [64]. Upon the application of DC voltage, the beam begins to roll down till the entire beam coincides with the bottom surface of the chip.

Figure 4.18 (b) exhibits the entire actuator set that is used in the proposed switches. It contains four rows of the electrostatic actuators. Each row includes four bi-layer beams acting as shunt inductive irises in the OFF state. The applications of four separate

Two steps at
both edges are
used to prevent
from collapsing

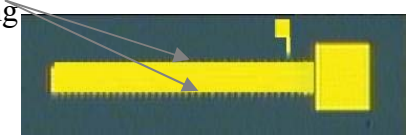

Bi layer cantilever beam (top view)

(a)

Gold covered

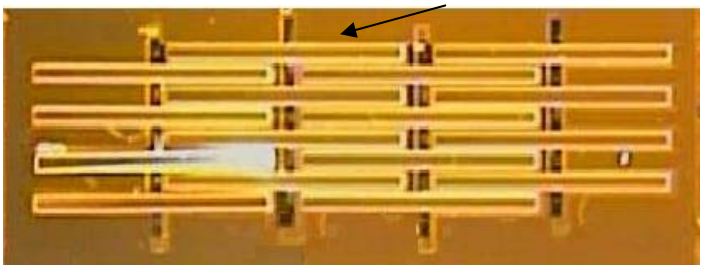

An array of actuators for the ON state act as a flat gold plate.

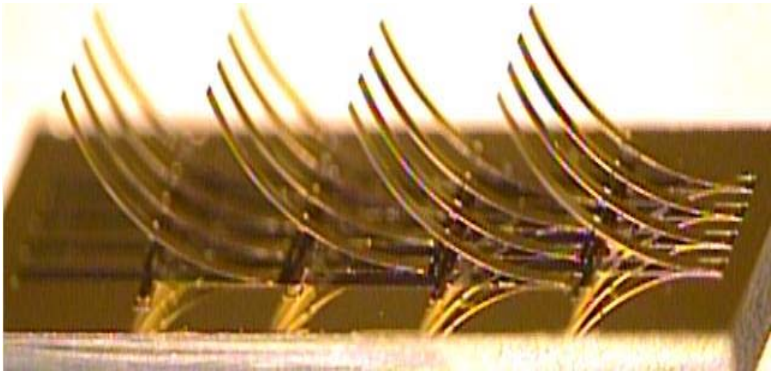

Actuators curled up to provide a short circuit.

(b)

Figure 4.18. (a) Single bi-layer curled beam from the top view and (b) one set of actuators in the down and up states.

beams rather than a single plate facilitate to have a better isolation in practice. It is because of the fact that the use of separate actuation mechanisms increases the overall contact points and hence reducing the contact resistance. All the actuators and also the rest of the area of the chip are covered with gold film to reduce the loss of the silicon base substrate.

4.2.2.1. C-type or Transfer RF MEMS Waveguide Switch

The proposed configuration of the C-type RF MEMS waveguide switch is portrayed in Figure 4.19 [69] . The prototype unit is designed for satellite Ku band applications. The switch is based on multi port single ridge waveguide structure that incorporates four sets of MEMS actuators. The inner waveguide channel is 10.8×4.4 mm with a ridge width of 1.6 mm and height of 4mm. This leaves around a 0.4 mm gap in between the ridge and the inner surface of the waveguide. The MEMS actuators are incorporated inside the waveguide under the ridge where the electric field has its maximum intensity. These actuators are initially in a position perpendicular to the inner wall of the waveguide which provides a short circuit between the ridge and the bottom plate of the waveguide. To establish a through path, these actuators are entirely removed to a position that coincides with the inner surface of the waveguide to have the least interference with wave propagation.

Figure 4.20 depicts the principle theory behind the proposed structure demonstrating state I. The switch is designed to be integrated in standard WR62 waveguide systems. Therefore, $\lambda/4$ transition to ridge waveguide is designed and utilized at the input ports. A ridge waveguide T-junction is used to connect the input line to two neighbouring ports. In the state I, the actuator sets of 1&3 are in the vertical position acting as shunt inductive irises. These inductors are designed to make a good short circuit and provide a high isolation between ports 1 & 2 and ports 3 & 4 at the frequency band of interest. An extensive effort is made to design the ridge waveguide discontinuities and the junctions in a way that the transferred impedance of the shunt irises act as open circuit and does not interfere with the transmitted signal from port 1 to port 4 and from port 2 to port 3. Meanwhile, the actuator sets 2 & 4 are in a position that coincides with the inner

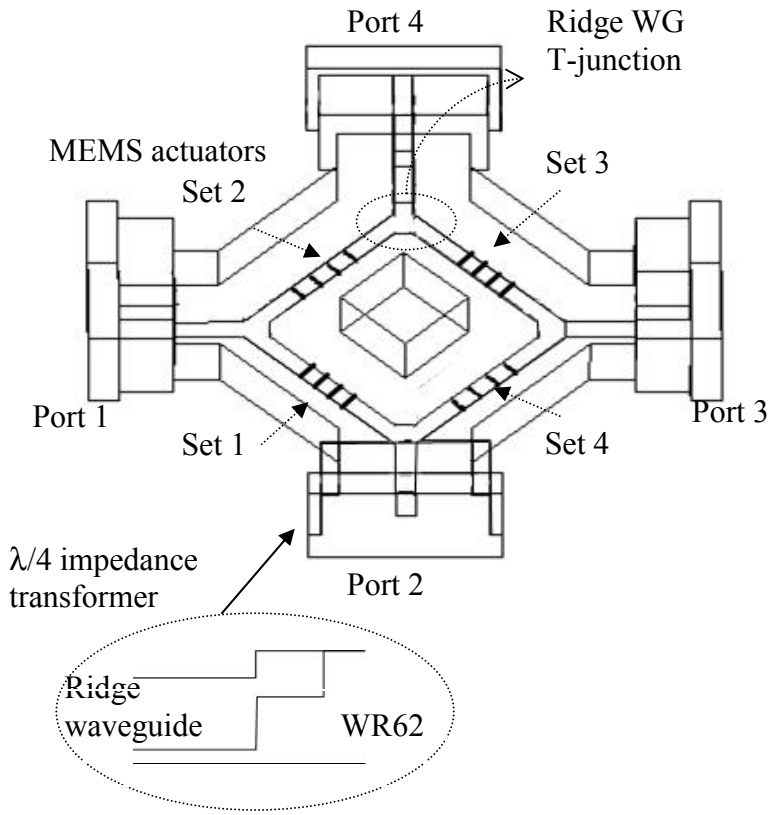

Figure 4.19. C-type switch conceptual schematic

wall of the waveguide providing a perfect ridge waveguide transmission line. A numerical analysis by using the FEM method realized by Ansoft HFSS [68] is performed and the results for state I are presented in Figure 4.21. It shows the ultimate achievable performance of the switch for the lossless MEMS actuators with ideal contact.

State II of the switch is realized by the application of a DC voltage to the actuator sets 1 and 3. This provides a through path from port 1 to 2 and port 3 to 4 and blocks the wave path between ports 1&4 and 2&3.

To prove the concept, a C-type MEMS waveguide switch is fabricated and tested. To realize the switch and facilitate MEMS device assembly, the waveguide structure is fabricated from two detached parts of the top and bottom. The top part includes the ridge waveguide channels as shown in Figure 4.22. The bottom plate incorporates the MEMS actuators and the required DC feed through pins. This structure is fabricated with the well established conventional machining process followed by gold electroplating. Although a

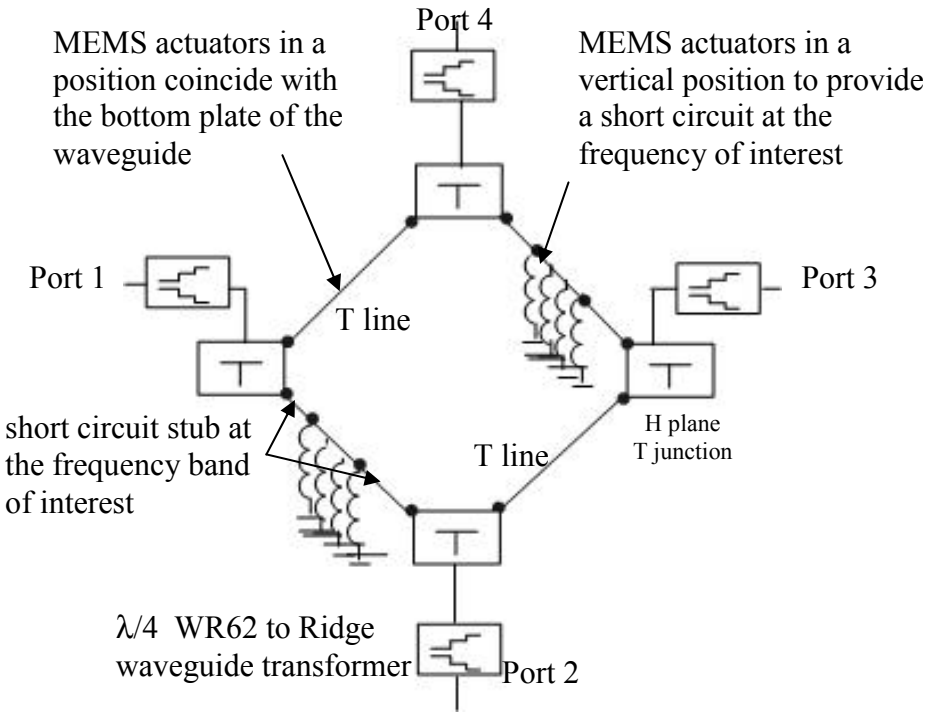

Figure 4.20. Operation diagram of the C-type switch shown in Fig. 3 in the state I.

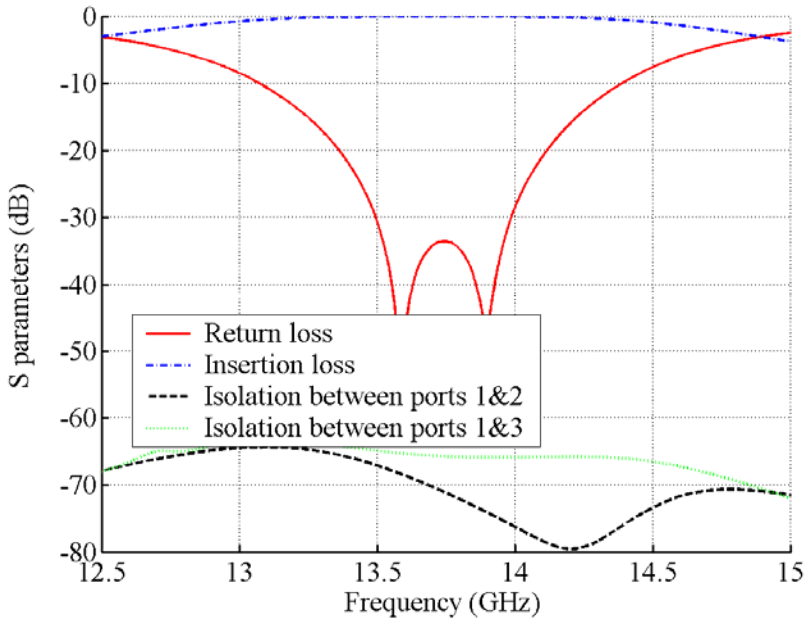

Figure 4.21. Simulation results for the proposed C-type switch with an ideal contact.

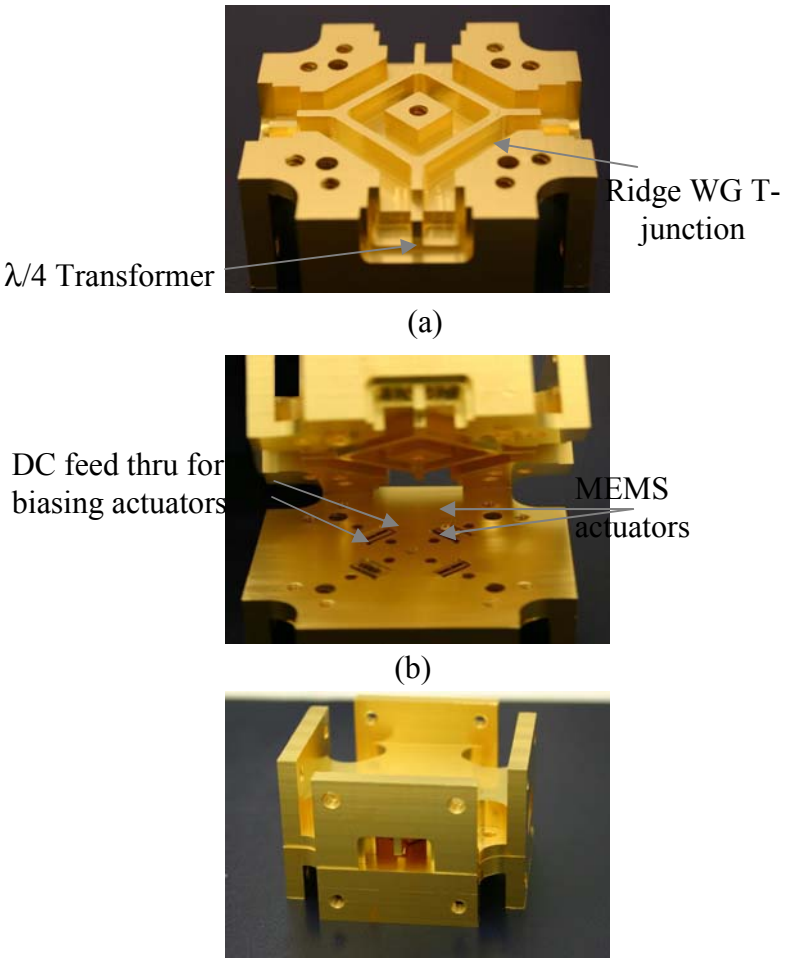

Figure 4.22: (a) Top plate including the ridge and the waveguide structures (b) Bottom plate that incorporates the MEMS actuators (c) Proposed C-type MEMS Waveguide Switch

waveguide interface is used for this prototype, the I/O interface can be easily implemented using co-planar lines.

After integrating the actuators inside the waveguide, a two-port measurement is performed while the other ports are matched. The results in Figure 4.23 indicate that a good return loss of better than -20dB has been achieved over 1 GHz bandwidth (13.3-14.3GHz). The measured insertion loss is about 1dB. This is principally attributed to the silicon substrate loss (actuators base substrate) underneath the beams they are in the vertical position and can be reduced by using a low loss alumina substrate. The measurement results show an excellent isolation of about 36-40dB. It is noteworthy

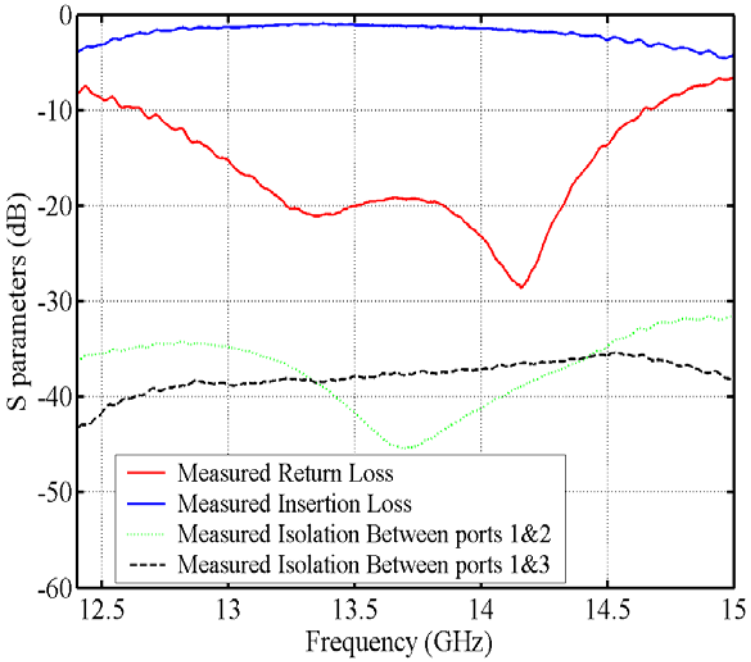

Figure 4.23. Measured results of the proposed C-type waveguide switch

that the deviation of the measured isolation with that of presented in Figure 4.21 is due to the fact that the simulation has been performed for an ideal contact with no resistivity. Nevertheless, due to the higher contact force of the novel actuators used in this switch, this is a tremendous improvement in comparison to the isolation achieved for the previously reported SPST MEMS waveguide Switch (15-17dB).

4.3. RF MEMS Coaxial Waveguide Switch

Although the proposed ridge waveguide switches indicate and excellent potential for high frequency and millimetre-wave applications, the switches have a very limited bandwidth mostly due to the quarter wavelength ridge to waveguide transformers. In addition, these switches are relatively large and smaller switch structures are desired.

In this section, we introduce a novel type of switch, based on coaxial lines integrated with MEMS actuators [70] is detailed. In comparison with the MEMS ridge waveguide switch, the MEMS-based coaxial switch exhibits a much larger bandwidth and is smaller in size.

Figure 4.24 shows a conceptual schematic of the proposed SPST coaxial MEMS switch where the MEMS actuators are integrated inside the coaxial structure on two sides of the line. For the ON state, the actuators are down coinciding with the inner wall of the outer conductor. For the OFF state, the actuators are in a vertical position shorting the inner conductor to the ground. The two sets of actuators on the top and the bottom, provides a very small parallel inductance and can offer good isolation.

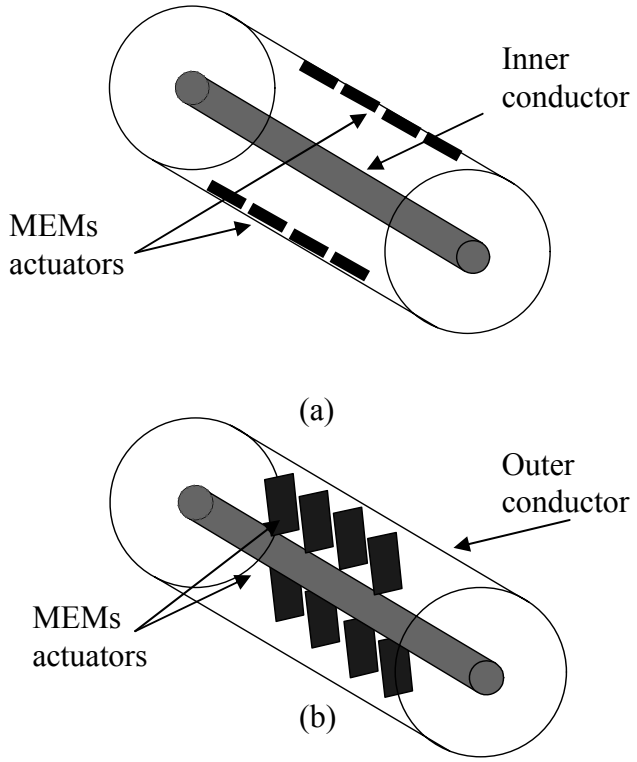

Figure 4.24. The conceptual schematic of the proposed coaxial switch (a) ON state, actuators coincide with the waveguide surface and (b) OFF state, actuators are in the vertical state.

4.3.1. Single-Port Single-Throw (SPST) RF MEMS Coaxial Waveguide Switch

To prove the concept, a rectangular coaxial switch is designed and is shown in Figure 4.25 (a). The rectangular coaxial line is picked because of ease of fabrication. An extensive effort is made to design a 50 Ω line and at the same time obtain a good isolation in the OFF state. This results in an outer conductor size of 8mm×1.8mm and the inner conductor has a size of 0.9mm×0.8mm. It should be noted that using a thickness of 0.8mm for the central line leaves about 0.5mm space on each side. The actuators at the OFF state curl up for 0.5mm and short the outer conductor to the central line. These

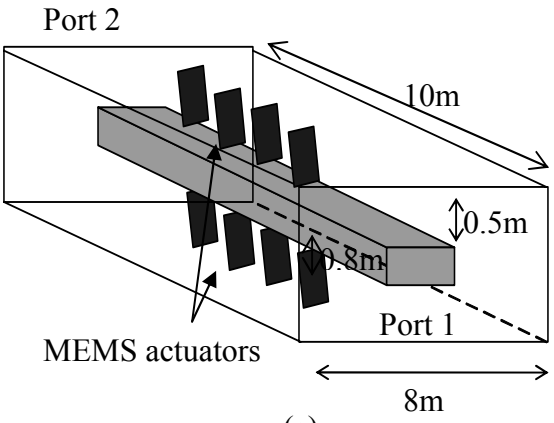

(a)

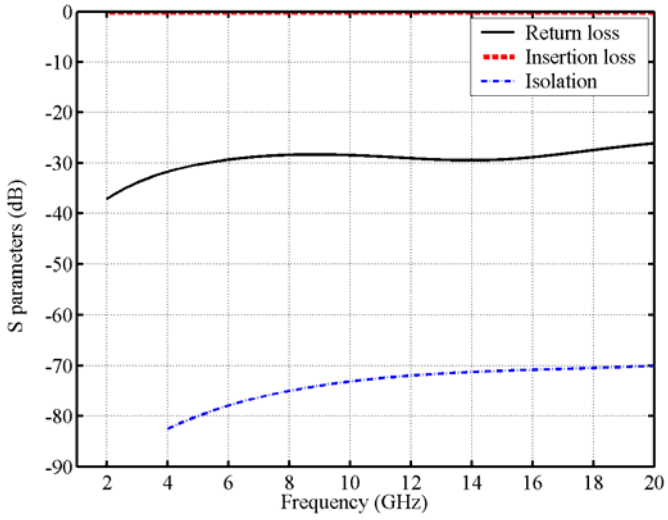

(b)

Figure 4.25: (a) Conceptual schematic and (b) simulation results for the proposed rectangular SPST coaxial switch.

actuators are entirely removed from the signal path for the ON state and provide a 50Ω coaxial through path.

By using HFSS© software the structure is analysed numerically and the results are given in Figure 4.25(b). It should be noted that the effect of the connectors and contact resistance is not considered and the given results reflected the ultimate performance of the proposed structure. To evaluate the concept, the switch is fabricated by a conventional machining process and gold electroplating. As seen in Figure 4.26(a), the outer conductor is constructed from two identical detached parts to facilitate the MEMS chip assembly. The DC voltage is applied through the DC pins at both sides of the MEMS chip and the inner conductor is attached to the SMA connectors at each port.

Figure 4.26(b) is a comparison on the proposed structure with that of the previously explained waveguide switch which clearly demonstrates that the SPST coaxial switch is much smaller in size. This is especially beneficial for satellite applications where mass reduction is an important issue.

Figure 4.27 records the two port measurement data for the proposed SPST MEMS-based coaxial switch. For the ON state when the actuators are in a position that coincides with the wall of the outer conductor, the return loss of the switch is less than -17dB from DC to 18 GHz. The measured isolation is 35dB for the lower frequencies and reduces to 20 dB at 17GHz. The insertion loss is less than 0.5dB up to 4GHz. The deviation of the measured results with those of the simulation with the HFSS is attributed to assembly imperfection and RF performance limitations of the SMA connectors employed in this prototype unit.

4.3.2. C-type or Transfer Coaxial Waveguide Switch

In this section, the idea of coaxial RF MEMS switches is expanded to a multi-port C-type switch. The conceptual schematic of the proposed C-type RF MEMS coaxial switch is shown in Figure 4.28. The switch uses the identical dimensions of the inner and outer conductors as the dimensions used in the proposed SPST switch. This leaves

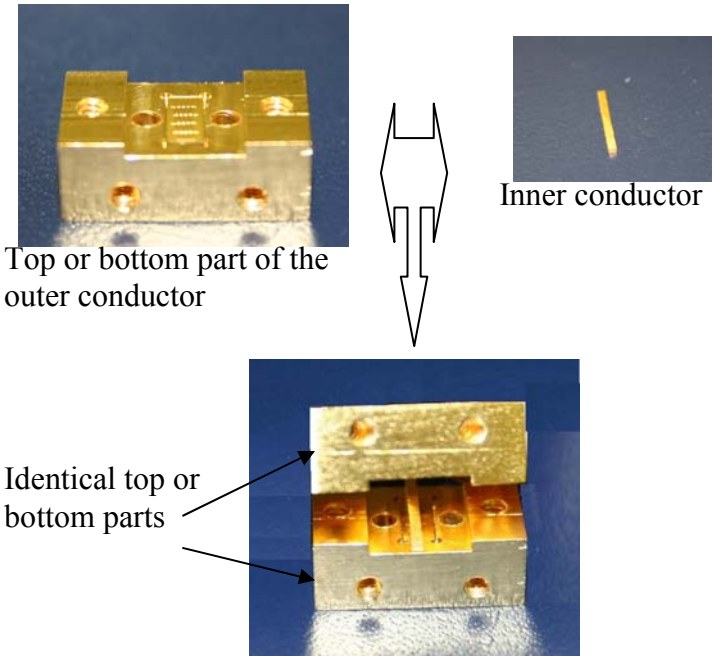

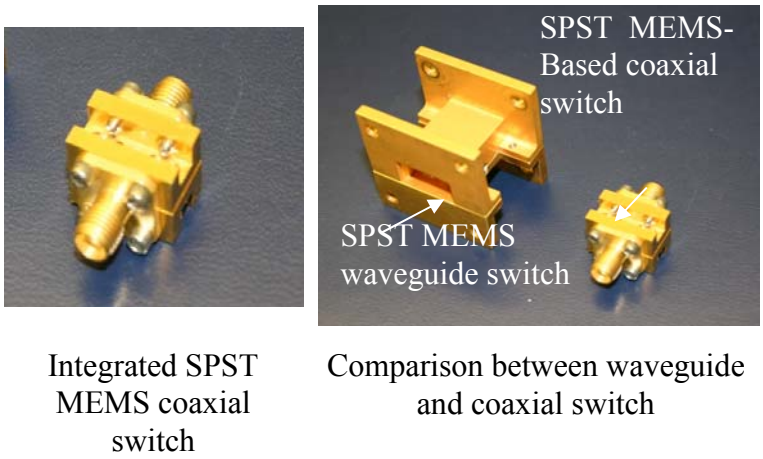

Figure 4.26 (a) Ground shielding and the central signal line of the switch and (b) integrated switch and comparison with the previously published SPST waveguide switch.

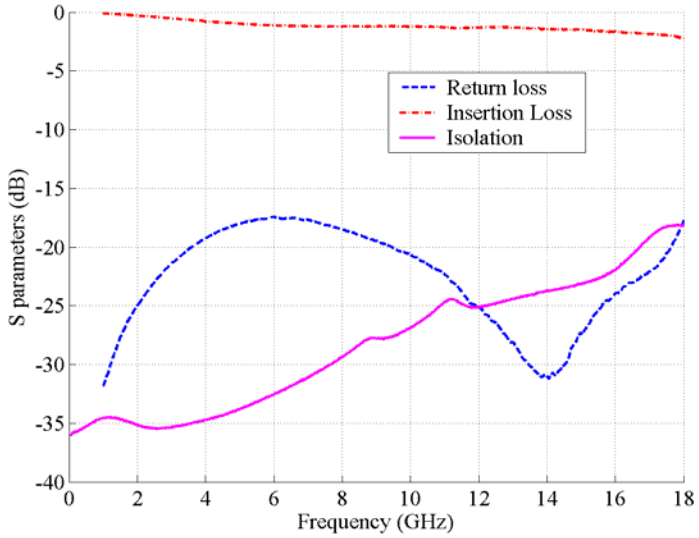

Figure 4.27: Measured results for the proposed RF MEMS coaxial SPST switch.

a 0.5mm space on each side between the central line and the ground, where the actuators are located.

For state I, the actuator sets 1&3 are in a vertical position perpendicular to the line and provide a short circuit between the signal line and the switch housing. Meanwhile, the actuator sets 2&4 are in the down position and are establishing a through path. To realize state II, actuators 1&3 are removed from the signal path whereas actuator 2&4 are rotated to a vertical position blocking wave propagation. Figure 4.29 depicts a simple circuit model of the proposed structure for the switch operating at state I. A coaxial T-junction is used to connect the input line to the two neighbouring ports. The vertical actuators (sets 1&3) behave as shunt inductive irises. These inductors are designed to make a good short circuit and provide a high isolation between ports 1 & 2 and ports 3 & 4 at the frequency band of interest. An extensive effort is made to design the discontinuities and the junctions in a way that the transferred impedance of the shunt irises behave as an open circuit and does not interfere with the transmitted signal from port 1 to port 4 and from port 2 to port 3.

After, a prototype unit of the proposed coaxial c-switch is constructed and tested. To facilitate the integration, the switch housing is fabricated from two identical detached parts by using the conventional machining process shown in Figure 4.30. After the

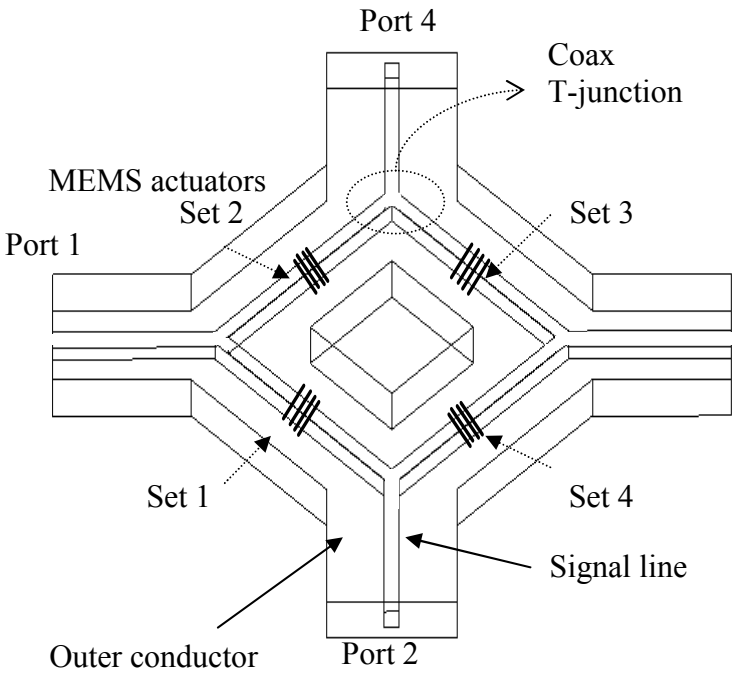

Figure 4.28: Proposed coaxial C-type switch

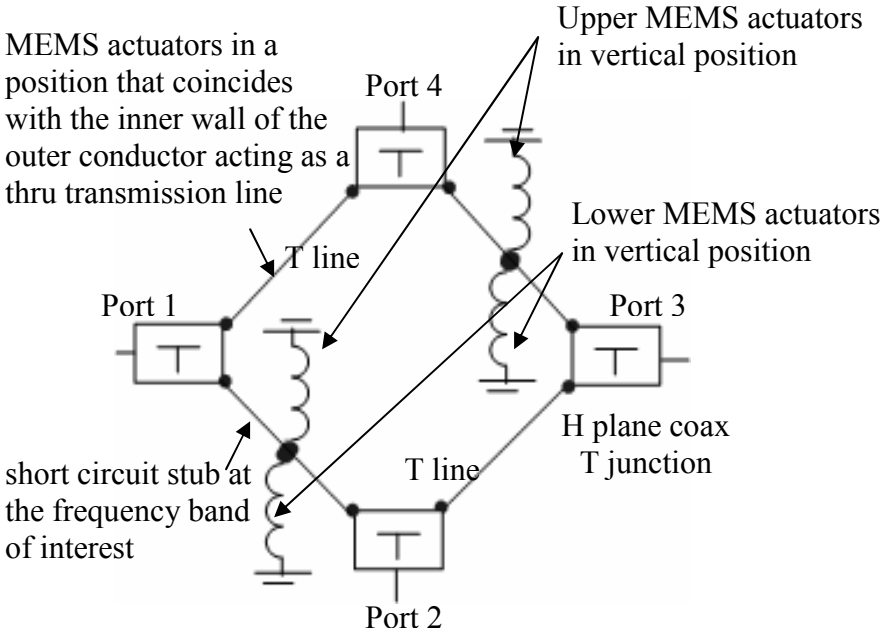

Figure 4.29. Operation diagram of the C-type switch shown in Figure 4.28 in state I

central signal line is also machined separately and it is gold plated. The MEMS actuators are integrated inside the ground housings, and a DC voltage is applied through the DC pins at both sides of each actuator set. The entire switch is assembled and connected to four SMA connectors for measurement.

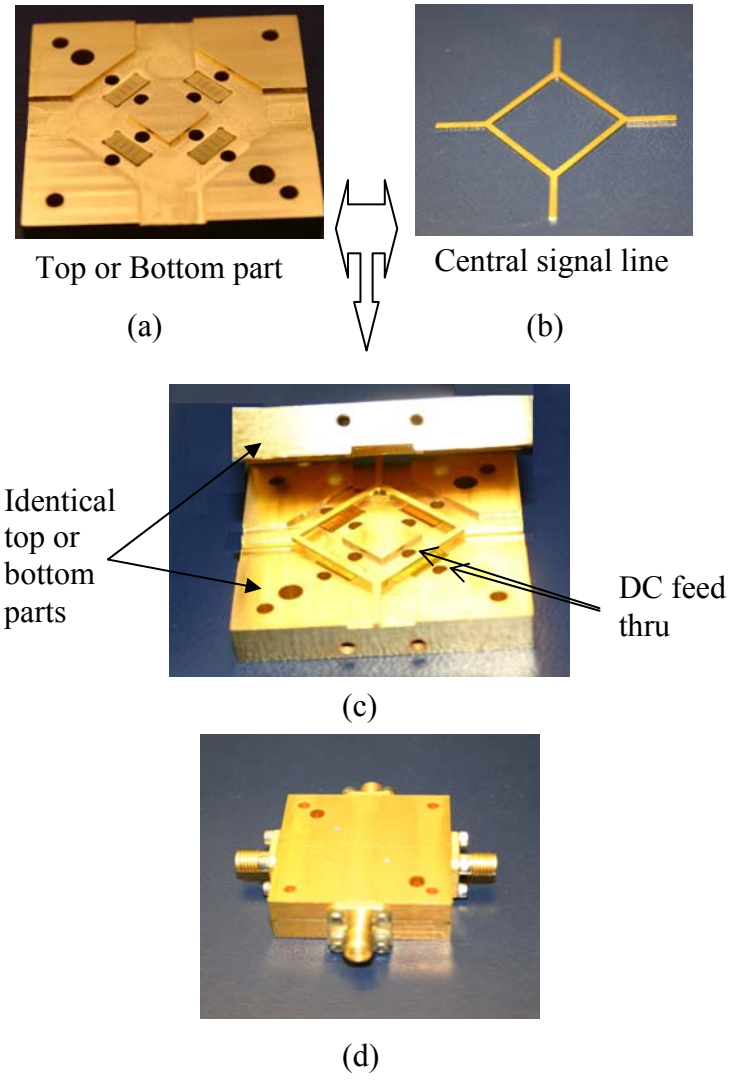

Figure 4.30: Fabricated coaxial c-type switch (a) top or bottom parts, (b) central signal line, (c) integration of the switch, and (d) integrated RF MEMS coaxial C switch.

The results of the two port measurement are revealed in Figure 4.31. A bandwidth of 65% for a return loss of less than -18 dB is measured (6-12 GHz). The insertion loss is between 0.9dB-1.2dB over the entire band which is mainly attributed to the connector loss and the silicon loss of the actuators base substrate. The isolation of the switch is better than -30 dB over the entire band. In a comparison of the measured data for the coaxial switch with that of the ridge waveguide switch in Figure 4.23, the coaxial switch offers a bandwidth that is nine times larger. This is achieved mainly because of the wideband nature of the coaxial lines compared to that of the ridge waveguide. In addition, unlike the ridge waveguide switch, there is no need to use any transformers for the MEMS coaxial switch.

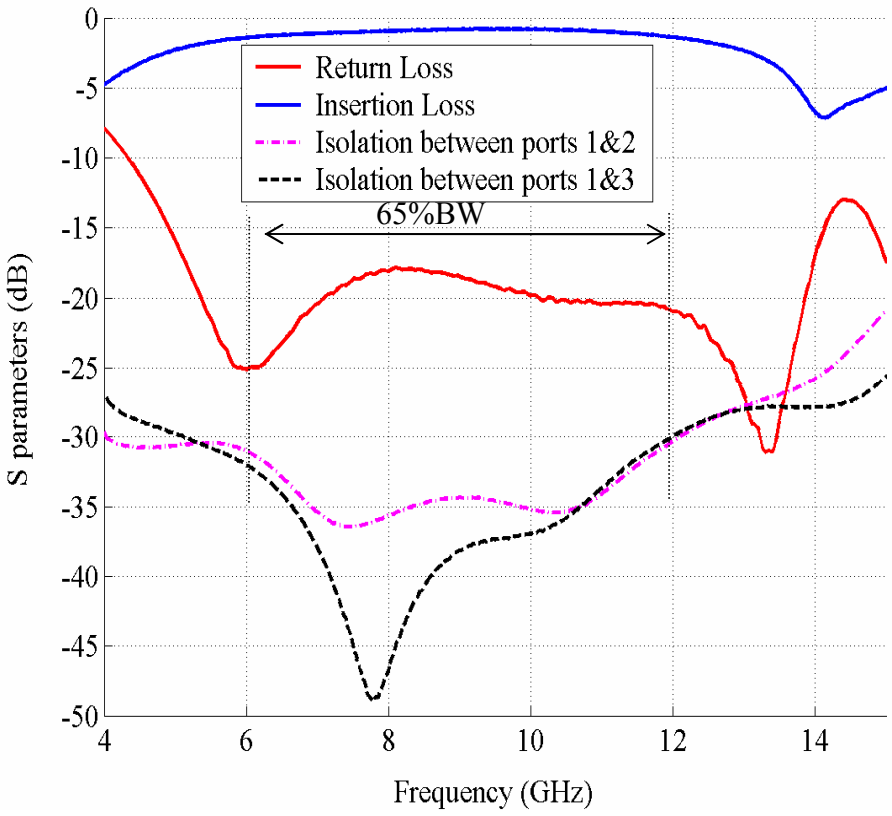

Figure 4.31: Measurement results for the proposed RF MEMS coaxial C-type switch shown in Figure 4.30.

4.4. Summary

In this chapter, for the first time, the concept of a 3D MEMS switch is explained in details. This type of switch is based on 3D transmission lines with incorporated MEMS actuators. Waveguide and coaxial MEMS switches are two different categories that have been investigated and various prototype units are fabricated and tested. These structures are promising to be extremely useful in high power and millimetre-wave application.

Initially, MEMS waveguide switches are presented where MEMS thermally plastic deformable actuators are integrated with a ridge waveguide to construct the switch. Simulation and experimental results are presented for the Ku- and K band MEMS waveguide switches. Also, an RF power measurement is performed to confirm the ability of the suggested switch to handle relatively high power levels (13W). In addition, the concept is expanded to multi-port 3D MEMS switch and a novel configuration for the C-type switch is presented. The ridge waveguide C-type switch incorporates unique sets of electrostatic bi-layer curled beams. The measured data proves the concept and shows a return loss of better than -20dB, insertion loss of 0.9-1.2dB, and an isolation of 40dB. According to the literature, this is the first time that a waveguide-based RF MEMS switch has been studied

Besides, an entirely new configuration of an RF MEMS coaxial switch is introduced offering a much larger bandwidth. To verify the idea, an SPST and a C-type MEMS-based coaxial switch is designed, fabricated and tested. The resultant bandwidth is nine times larger than that of ridge waveguide switch.

The 3D RF MEMS switches presented in the chapter are extremely useful in satellite redundancy switch matrix applications. Moreover, the switches can be realized monolithically for millimeter-wave applications and are expected to have a power handling capability much higher than that of traditional MEMS switches.

Chapter 5

Monolithic RF MEMS Switch Matrix Integration

5.1. Introduction

In telecommunication systems, microwave and millimeter wave switch matrices are essential components since these matrices enhance satellite capacity by providing full and flexible interconnectivity between the received and transmitted signals. The demand for more advanced switching systems has increased by the recent growth in multi-media, mobile and internet applications.

Satellite beam linking systems vastly rely on switch matrix functionality to manage traffic routing and for optimum utilization of system bandwidth [72]. Figure 5.1(a) is an example of a satellite payload, receiving six different beams from various locations and transferring them to their intended spots. The beam link system creates the sub-channels for each uplink beam where the switch matrix provides the flexibility to independently direct them to the desired downlink channel.

Figure 5.1 (b) and (c) illustrates the Multi-Media Pre-Processor (MMPP) as another type of beam linking system [72]. Its purpose is to provide an optimum balance between the amounts of analog and digital processing so that the payload power consumption and cost is minimized. The MMPP does this by adding the flexibility to share the available digital resources among the different beams. For example, typically the digital processor must be sized by assuming that every beam is completely full. In

reality this is not the case and the MMPP allows the digital processor to be smaller and to consume much less power by allowing the available digital resources to be flexibly assigned to the beams as required. There are two cases to consider: narrowband digital processing (Figure 5.1 (b)) and wide band digital processing (Figure 5.1 (c)). In the first case, the digital processing bandwidth capability is less than the bandwidth allocated to the beams. The purpose of the MMPP is to break the wide band uplink in to smaller bandwidth segments compatible with the digital capability and process only those segments carrying traffic. The switch matrix selects which digital chain will process which beams data. In the wide band case, the digital processing bandwidth capability is the same as or higher than the bandwidth allocated to the beams. In this case the purpose of the MMPP is to combine the bandwidth of underutilized beams into a wider bandwidth for the digital processor so as to reduce the number of the required digital processing chains [72].

Currently, the common microwave switch matrices employed in satellite payloads utilize mechanical and semiconductor switches. The MEMS technology provides the opportunity to substitute these switches by miniature MEMS counterpart that perform exceptionally at microwave and millimeter-wave frequencies including low insertion loss, high isolation, and low inter-modulation distortion. However, by reducing the size and increasing the system density, signal transmission and the isolation of the interconnect lines become an important issue. This highlights the fact that there is a need to develop a new planar MEMS compatible solution for network connectivity.

LTCC technology is a good solution to provide the switch matrix connectivity. The basic materials are ceramic tapes that are fired together at around 900 degrees. It allows usage of high conductivity materials such as gold and silver to provide multilayer structures. However, dimensional tolerances are still an issue especially at high frequency applications due to the material shrinkage during the firing process. Also, the achievable minimum dimensions for the lines and gaps in comparison with those of the conventional ceramic processes are considerably large. The fabrication process for LTCC is more expensive in comparison with the conventional fabrication processes for MIC circuits. To

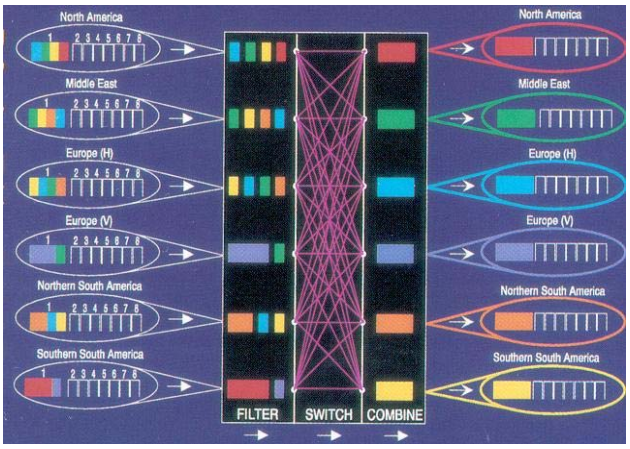

(a)

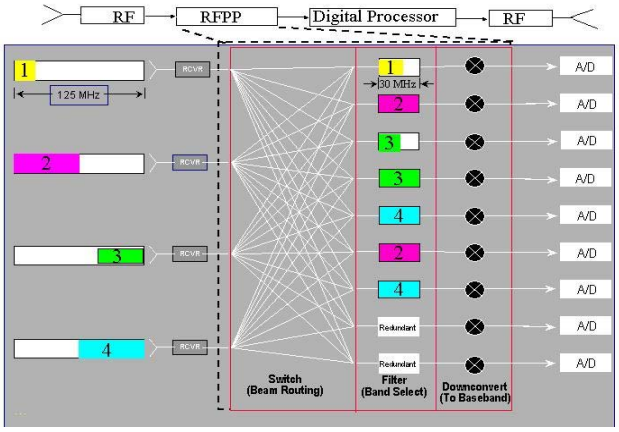

(b)

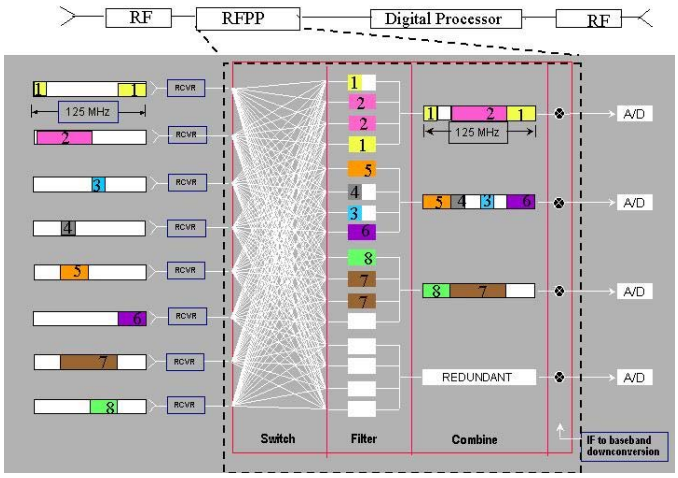

(c)

Figure 5.1: Switch Matrix application in beam linking for (a) full functionality of satellites, and (b) MMPP for narrow band, and (b) for wide band digital processors [72]

our knowledge, up to now, the only published MEMS switch matrix is reported in 2004 by B. Yassini et al.[32] and is based on hybrid integration of an LTCC interconnect network with the SP4T Michigan/ Rockwell MEMS switch [57]. This switch matrix exhibited in Figure 5.2, not only suffers from the common existing problems of LTCC, but also exhibits very limited -15dB bandwidth (0-7GHz) due to the hybrid assembly and use of wire-bonds. This highlights the need for a new solution to provide matrix connectivity monolithically and maintain precise miniaturized MEMS compatible dimensions.

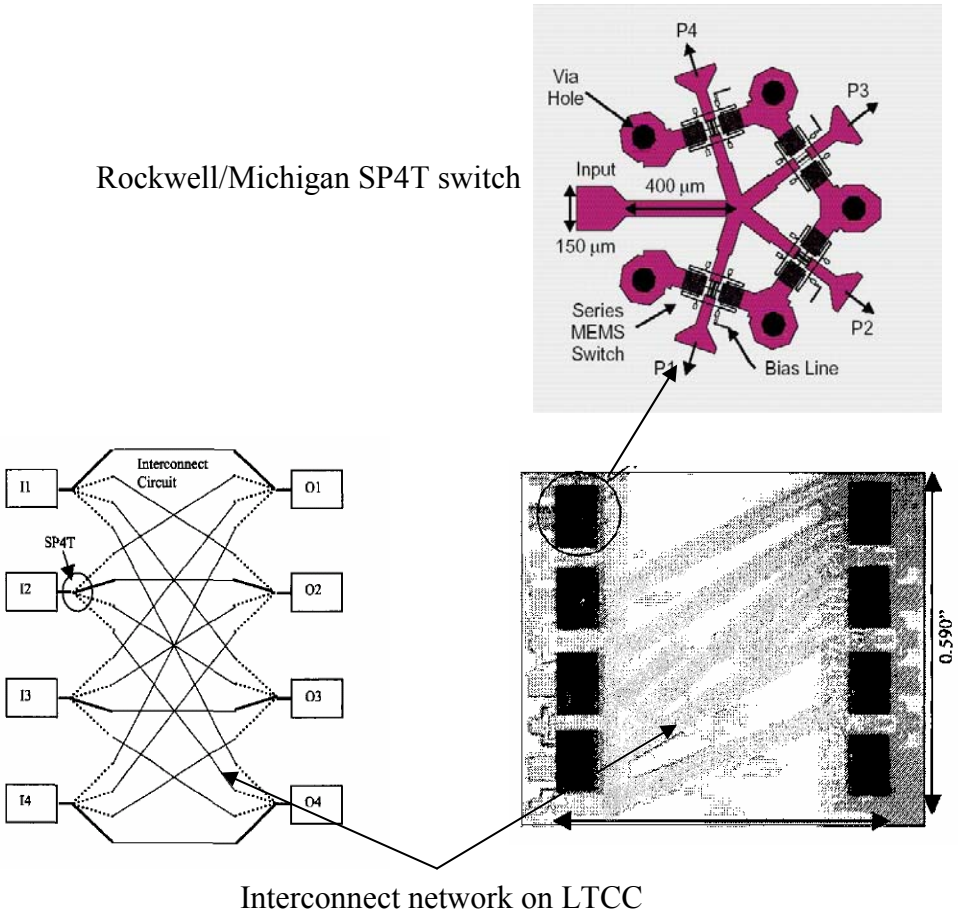

Figure 5.2: Previously published hybrid RF MEMS switch matrix based on Rokwell/Michigan switches integrated with the LTCC interconnect network [57]

In this chapter, novel compact interconnect networks amenable to MEMS technology are presented. The proposed concept eliminates the need for a multilayer manufacturing process and provides excellent RF performance by using well established microwave printed circuit technology. In addition, the characterization of the interconnect lines and required vertical junctions are detailed. Two different 3×3 interconnect networks; the broadband interconnect network and vialess interconnect network are built and tested to verify the proposed concept. The interconnect network is integrated monolithically with multiport RF MEMS switches to construct a switch matrix on a single chip.

5.2. Proposed Double-Sided Interconnect Network Principles

Typically, the MEMS fabrication of switch matrices would usually require a planar interconnect structure with several lines to provide the system connectivity. Appropriate integration techniques not only offer size reduction and add flexibility to the system design, but also minimize loss of the distribution network. One promising solution, using alumina substrate, is to pattern the main circuit on one side of the substrate and use the other side for the crossover transitions. This idea takes advantage of the planar nature of the coplanar transmission lines (CPW) and it is well-compatible with the previously proposed MEMS switches. A precise design to prevent parasitic coupling along with appropriate layout design and relative placement of the lines, vias and vertical transitions, is necessary in order to optimize the performance.

When several transmission lines are printed on a common substrate, surface waves and radiation tend to induce parasitic currents on the neighboring interconnects and circuits leading to unwanted crosstalk. This parasitic coupling becomes more problematic since the circuits are printed on two opposite sides of one substrate. In coplanar waveguides with infinite ground planes, the first higher order mode after the CPW mode is TM_0 [74]. The major advantage of the finite ground coplanar (FGC) waveguide is that the lowest surface wave mode is TE_0 and the leakage occurs at higher frequencies compared to the infinite ground plane CPW line [74]. We propose to use FGC lines to

design the entire interconnect circuit for the switch matrices. It is believed that due to the nature of the FGC and the thin substrate thickness (10mil), the surface wave mode and any additional substrate modes can have no effect on the switch matrix RF performance over the operating frequency band of interest (up to 30GHz).

As it is known, increasing the overlapping area of two lines printed on two layers results in higher cross coupling [75]. Consequently, the two parallel lines structure shown in Figure 5.3 is expected to have more coupling than that of the two orthogonal lines. To optimize the design, the effect of the substrate thickness on the coupling of the two parallel lines is investigated. The results of the MOM simulation implemented by Sonnet software [76] for the ground strip width of w_g= 120µm, central line width of w=60µm, gap space of s=24µm, and length L=1mm are recorded in Figure 5.4. As illustrated, the thicker substrate yields less coupling. However, it leads to a higher inductance loading of the vertical transitions, which will be discussed in the next section. A 10mil substrate is a good candidate to obtain a higher than 35 dB isolation up to 30GHz while maintaining reasonable performance for the vertical transitions.

Figure 5.5 illustrates the effect of the centre line width w and gap spacing s on the coupling. To obtain this graph, three different 50Ω lines with various w's and s's on a 10mil alumina substrate with a w_g of 120µm are considered. For $w+2s$ equal to 58, 112, and 184 µm, w is 32, 64 and 105 µm, respectively. Note that for the smaller $w+2s$, better isolation is achieved as the electric field is more confined within the gaps. However, from a fabrication point of view, it is not desirable to use line widths of very small dimensions. To achieve a good isolation while accommodating a reasonable insertion loss we selected w= 64µm and s=24µm. For our preliminary design, both the MOM implemented by Sonnet® and FEM realized by HFSS® confirm that an isolation of higher than 35 dB can be achieved [76]-[77].

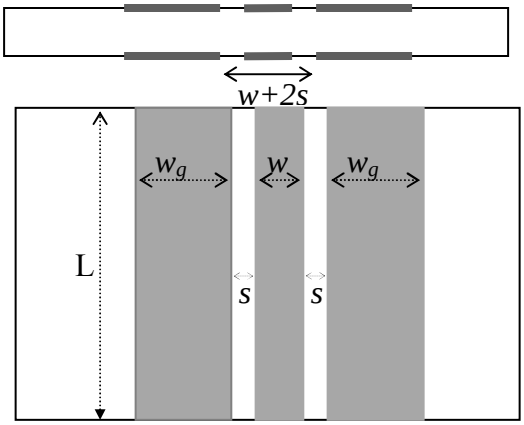

Figure 5.3: Schematic of FCG lines printed on both sides of the substrate.

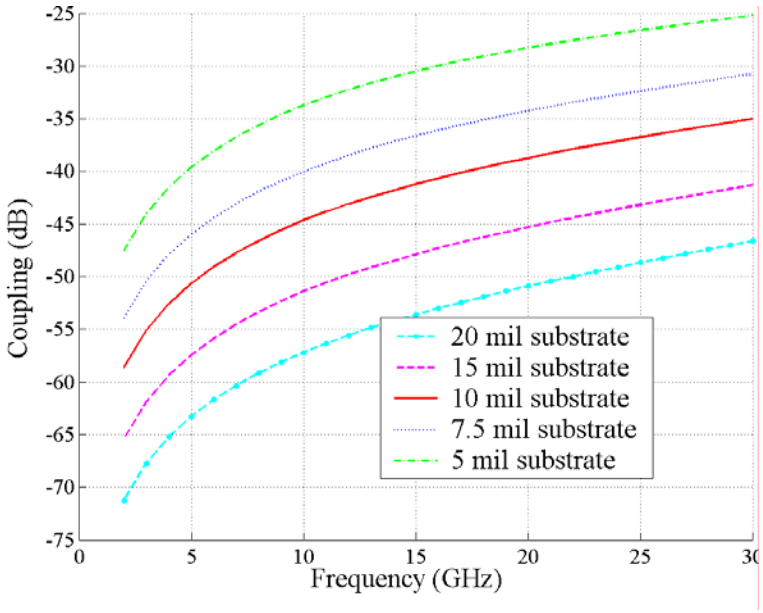

Figure 5.4: Numerical results for the two lines on both sides of the alumina substrate for various substrate thicknesses.

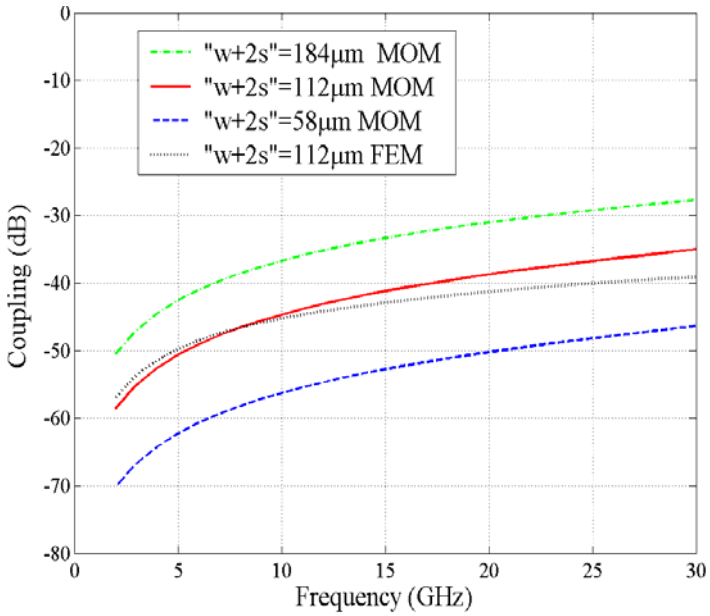

Figure 5.5: Coupling of two lines on different sides of the alumina substrate for 50Ω lines with various w+2s.

Additionally, cross coupling between two perpendicular FGC lines is examined and the schematic and FEM simulation results are shown in Figure 5.6. The results are obtained for the optimized dimensions of w= 64µm, s=24µm, w_g=120µm on 10 mil (254µm) substrate. The isolation of the lines are better than -45dB for frequencies up to 30 GHz. As expected, the coupling is considerably less than that of parallel lines. The field distribution inside the substrate is also illustrated in the figure. It is evident that the field concentrates mainly around the gaps and thus the use of a smaller gap results in better isolation.

5.3. Broadband Planar Interconnect Network

The main goal of this section is devise a technique to design and fabricate broadband planar integrated RF switch matrices [79]. The initial focus is on single and double conducting vertical transitions with minimizing the parasitic coupling. Then the entire switch matrix architecture including the vertical transitions is considered.

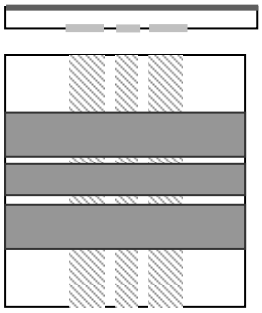

(a)

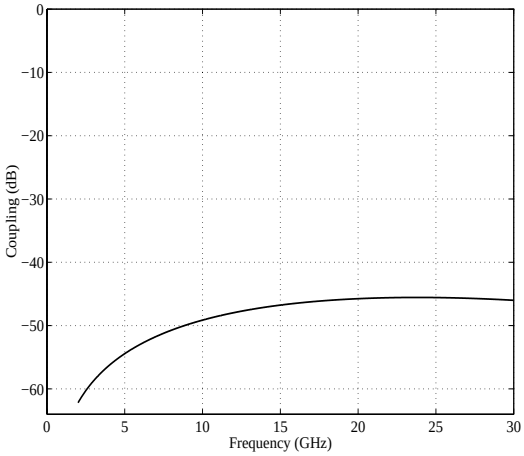

(b)

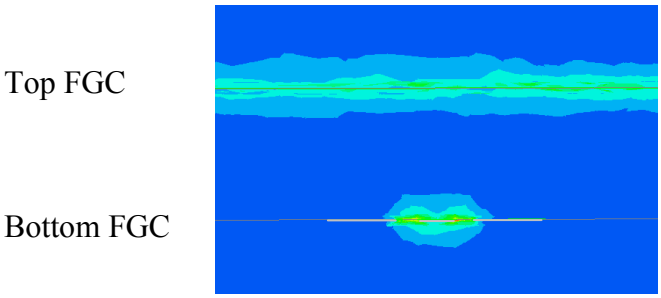

(c)

Figure 5.6: Two perpendicular FGC lines on opposite sides of the substrate (a) schematic, (b) FEM simulation results, and (c) electric field distribution.

5.3.1. Three Via Interconnect

Although the design of vertical transitions in microstrip lines, strip lines and conventional coplanar lines are well established in the literature, very limited work has been reported on vertical transitions of FGC lines [78]-[80]. This section addresses the concept of vertical system integration by developing a three-via interconnect between the FGC lines.

A conceptual schematic of the three-via vertical interconnect is given in Figure 5.7. The cylindrical vias form a three conductor transmission line through the substrate which minimizes the radiation entering the substrate. To optimize the performance of the transition, the choice of the via separation and junction dimensions are critical.

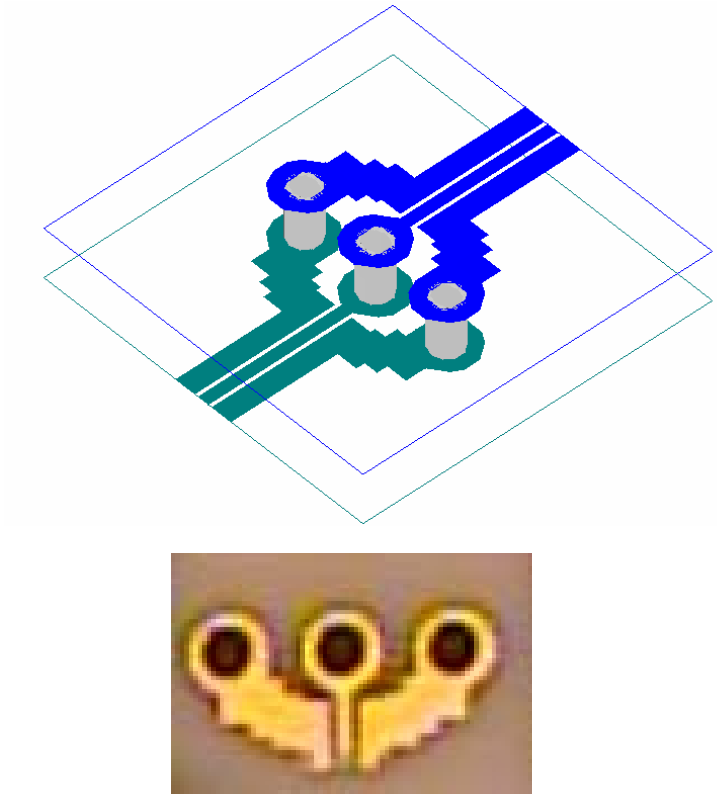

Figure 5.7: A vertical interconnect employing three via holes. The vias permeate the substrate to connect the upper and lower finite ground coplanar transmission lines.

For the preliminary interconnect network the dimensions of the vias in a 10mil alumina substrate are optimized. The vias are attached to the FGC lines with a signal line width of 64μm, a spacing between the signal and ground lines of 24μm, and a ground line width of 120μm. The inner via diameter is ρ_v=180μm, and the outer diameter of the via annular ring ρ_o is 320μm. The three-via vertical interconnect is matched to a 50ΩFGC lines through an optimized junction. Figure 5.8 illustrates the HFSS simulation results of the optimized transition with a return loss of better than -30 dB up to 30GHz. To confirm

the results, the via is matched to a 50Ω line on one side and a one port measurement is performed from the other side. The measured return loss agrees well with those of the simulation. Insertion loss of the system is also optimized to better than 0.25dB up to 30GHz.

As it was previously mentioned, the three vias act as a three conductor transmission line. The electric field distribution proves this concept while the field extends from the central line to both outer ground lines. The field is well confined between the vias and vanishes at the outside of the outer lines as detailed in Figure 5.9. Thus it is expected to have the minimum parasitic coupling to the neighboring lines.

Wideband modeling of a three-via structure is very difficult in terms of the RLC discrete elements due to the intertwining and interrelating of the vias, tapered bends and surrounding transmission lines. In general, the vias are significantly inductive. To obtain a precise insight, the three-via junction is shorted from one side while one port measurement is performed from the other side. The measured input impedance shown in

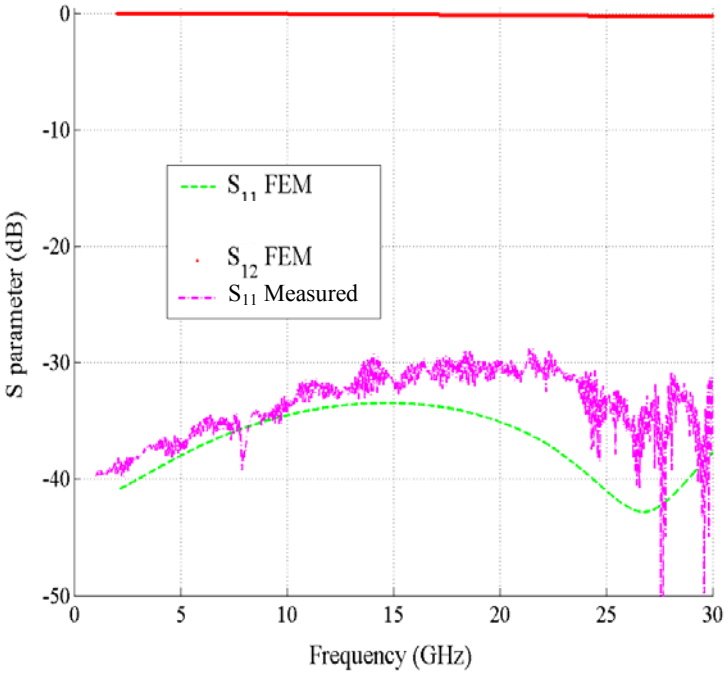

Figure 5.8: Performance of three- via junction.

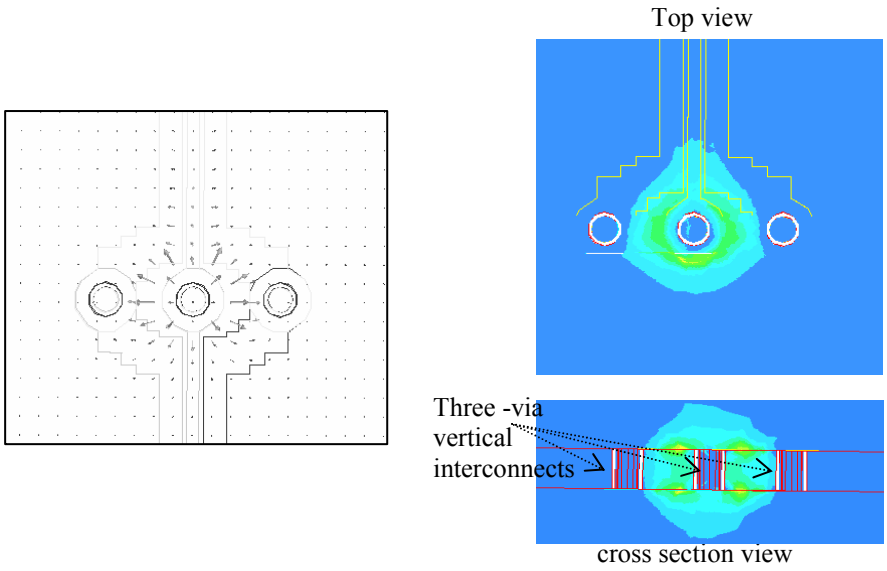

Figure 5.9: Electric field distribution for vertical three-via interconnect (a) magnitude and (b) vector.

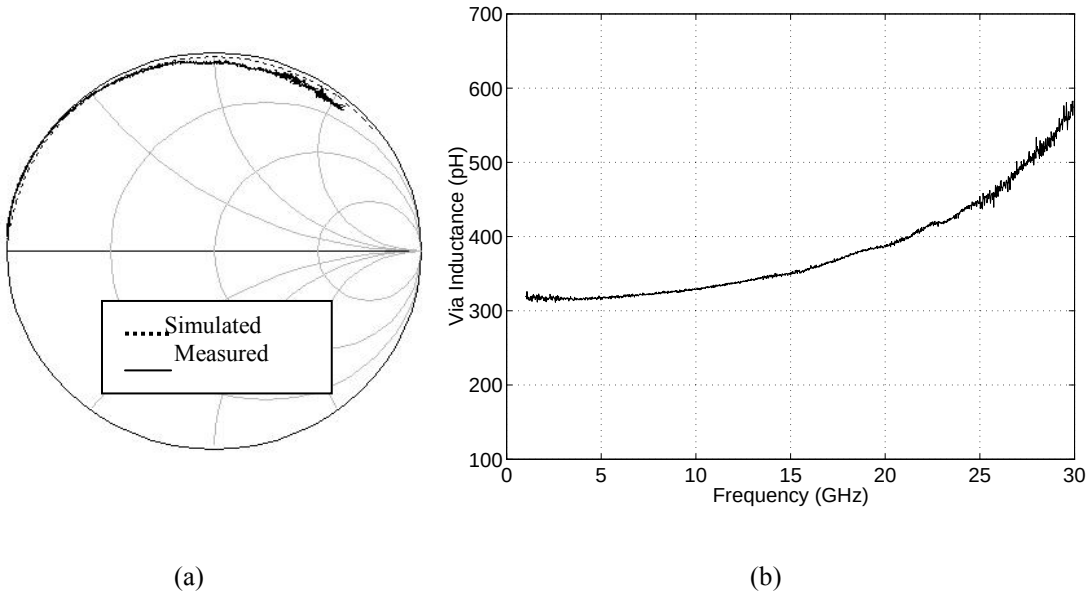

Figure 5.10. (a) Measured and simulated via input impedance and (b) measured via inductance.

Figure 5.10 indicates that the vias have inductive effect of about 350pH up to 15GHz which increases to 580pH for the higher frequencies.

5.3.2. Double Three-Via Vertical Interconnect

A double three-via transition can be used to establish a crossover of two FGC lines printed on the same layer as shown in Figure 5.11 (a). The vias penetrate through the substrate and are connected together by using a coplanar waveguide at the back side of the substrate. The total junction is optimized to prevent from parasitic interaction of the vias and to minimize the parasitic coupling to the crossing line of the top layer. At the back side, a coplanar waveguide with a central signal line width w=72μm, gap space $s=32\mu m$, and ground plane width $w_g=520\mu m$ is used. The application of the CPW on the backside instead of the FGC lines improves the return loss and prevents the need to use tapers at the back side of the substrate.

Significant effort is made to optimize junction dimensions up to 30GHz. The Sonnet© results are shown in Figure 5.11 (c). FEM analysis (implemented by HFSS©) is also used to verify the performance of the double three-via configuration and the results are illustrated in the same figure. In both simulations, the structures are identical except that in the MOM analysis (implemented by Sonnet) the thickness of the conductor is ignored which contributes to a slight deviation in the results of the two EM simulators. The insertion loss is less than 0.5 dB at 30GHz. Almost half of this radiation can be attributed to radiation loss of each three-via vertical interconnect.

The parasitic coupling of the transition on the top crossing line is expected to be better than -45dB as depicted in Figure 5.11(c). A comparison of these results with those in Figure 5.6 proves that the three-vias interconnect does not add extra parasitic coupling to the other line.

The proposed double 3-via structure is fabricated by using alumina substrate and a gold coating of 3.5 μm, as shown in Figure 5.11 (b). A two-port S parameter measurement is performed and the results are plotted in Figure 5.11(c). It is observed that

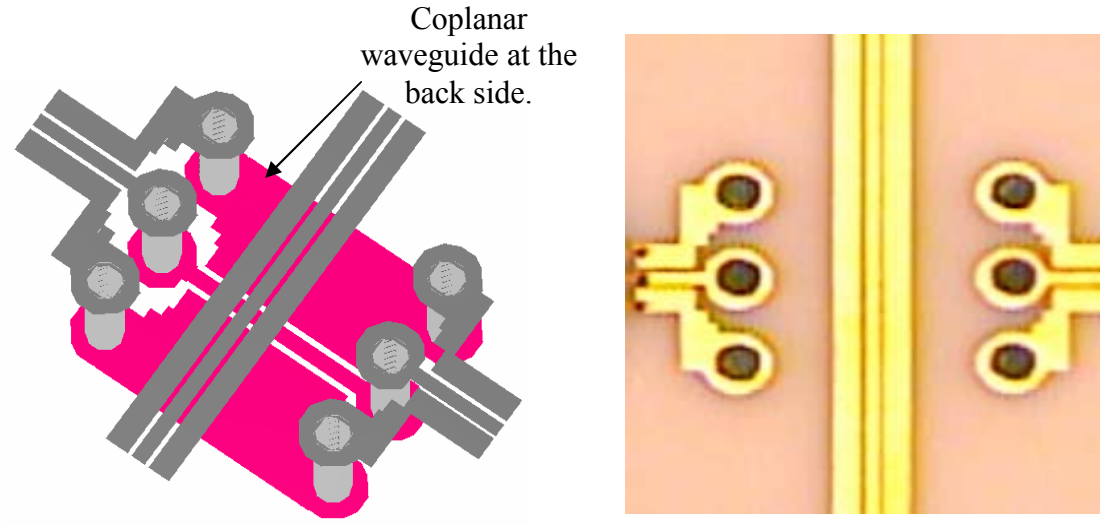

(a) (b)

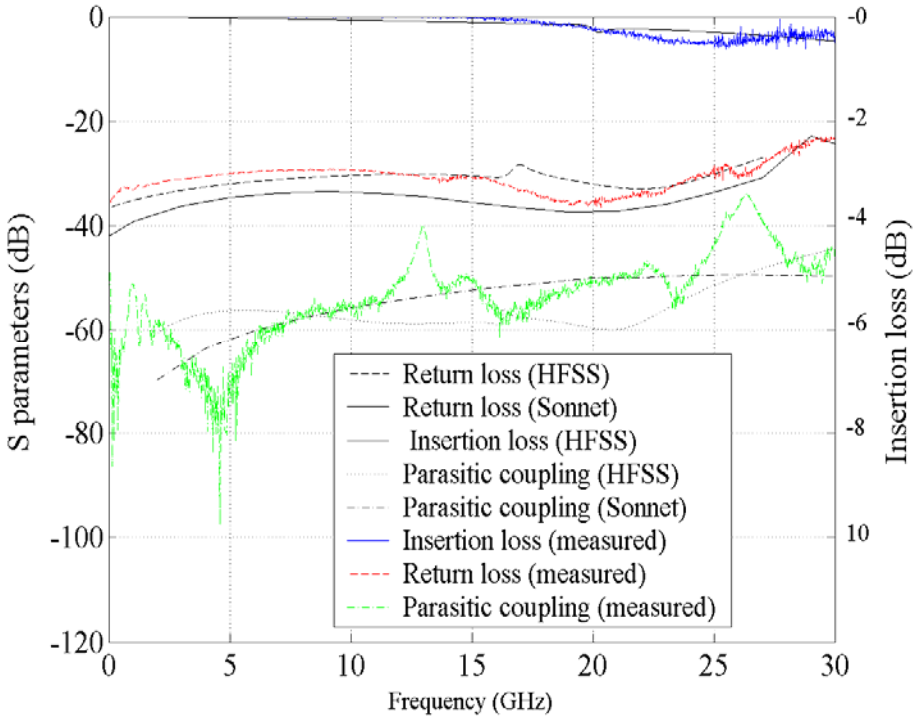

(c)

Figure 5.11 (a) Conceptual schematic, (b) fabricated unit, and (c) simulated and measured results of double three-via vertical transition over alumina substrate

the measured data agrees well with that of the simulation. It indicates a less than -30dB return loss up to 25 GHz and -25 up to 30GHz. The insertion loss is 0.5 as was predicted. The isolation of two double three-via structure with the crossing line is better than -45 dB.

5.3.3.Switch Matrices Interconnect Architecture

In conventional systems, switch matrices are employed to provide a connection between a set of inputs and a set of outputs through the switch elements and a set of signal paths. One approach, for connecting *N* input ports to *N* output ports is to use SPNT switches and make pairwise connections between each input and each output switch, as shown in Figure 5.12(a). Although the concept can be theoretically used for any size switch matrix, in practical applications, small matrices are employed as basic building blocks to create larger structures. There are several topologies that can be used in this regard [81]-[82]. Figure 5.12 (b) illustrates a Clos interconnect network that is constructed of several N×N building blocks to form an M×M matrix [82]. It is a rearrangeable network that has the capability of connecting any input to any output while one or more existing links may need to be rearranged for each new set of connections.

The objective is to build an N×N switch matrix with N as large as the technology allows to be used as the building blocks for the large switch matrices required in beam link satellite payloads. To verify the idea of double sided architecture, an interconnect circuit for a basic building block of N=3 is designed and fabricated. Alumina is used as the main substrate to fabricate the interconnect lines and to incorporate MEMS beams monolithically or in hybrid-form. As it is illustrated in Figure 5.13, the main circuit is patterned on the top side of the substrate whereas the back side is used for cross over transitions. This configuration utilizes 9 lines connecting three SP3T switches at the input to three other SP3T switches at the outputs. It is noteworthy that in any given state, only three of these lines are carrying on RF signal. Throughout the design, the intention is to maximize the distance between the lines carrying the signals to reduce unwanted couplings. For instance, two adjacent lines from two neighboring switches which can carry signals simultaneously are patterned in two different layers to increase the pitch.

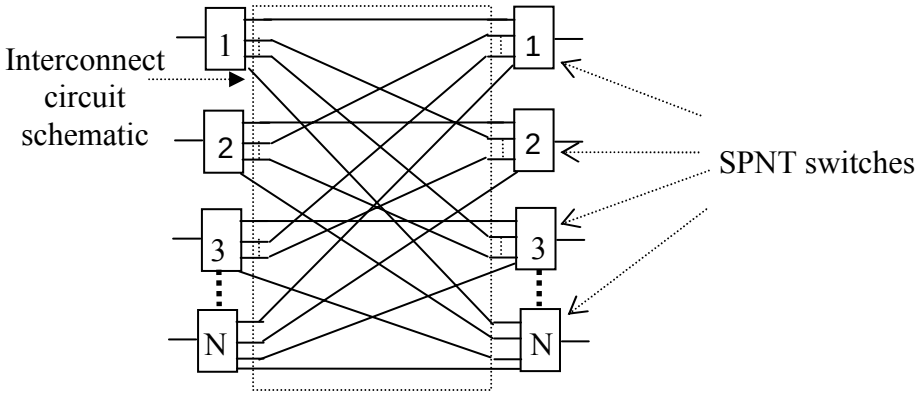

(a)

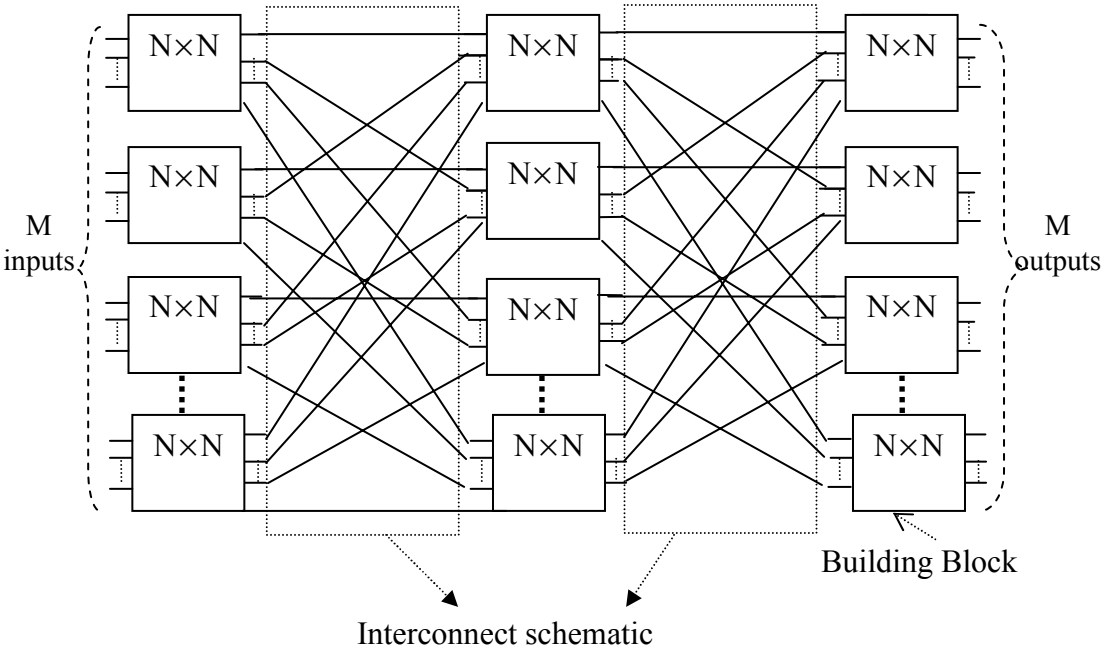

(b)

Figure 5.12: (a) Small N×N matrix as building block and (b) bigger networks composed of several small building blocks (three stage Clos rearrangeably interconnect network [82]) .

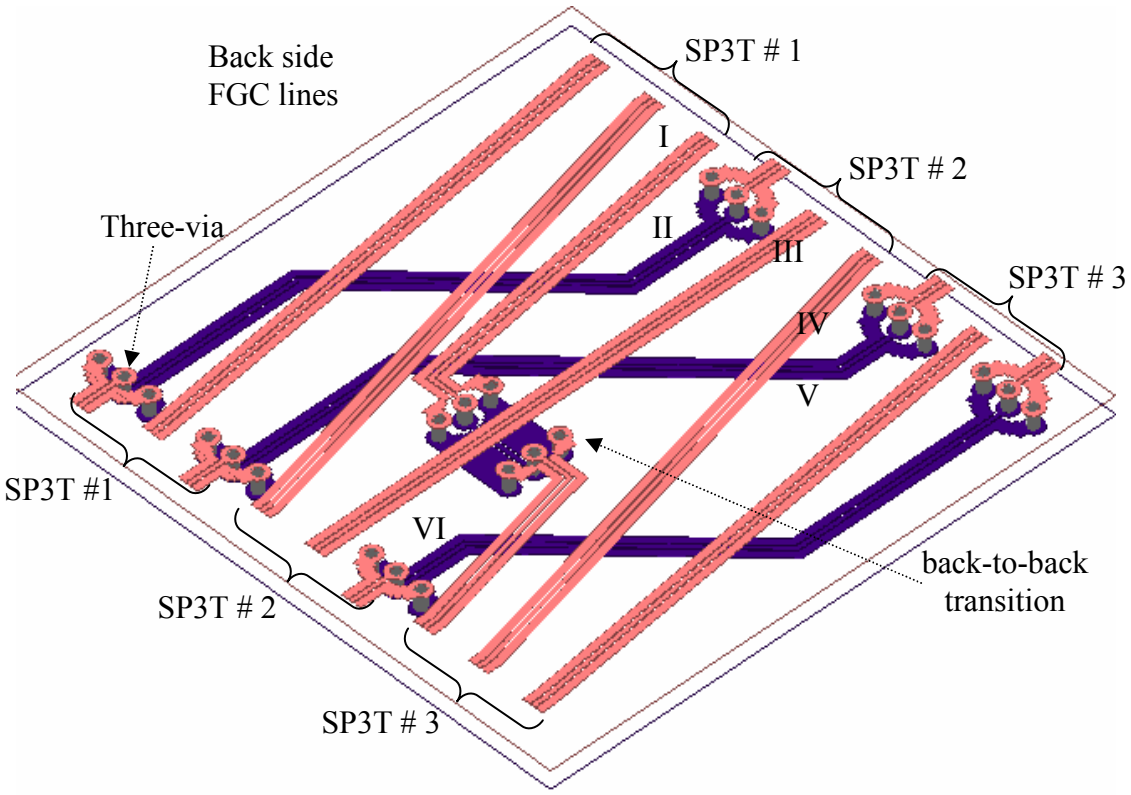

Figure 5.13: Proposed double sided interconnect circuit for 3×3 switch matrix structure.

The lines are 50 ohm FGC with w= 64µm, s=24µm, and w_g=120 µm on 10mil (254µm) substrate. The previously optimized dimensions of the vertical interconnects are used for the connection of the signal lines from one side to the other. To predict the interconnect lines performance, they are subdivided and analyzed by using full wave techniques and then linked through net list coding. All the lines are optimized and show less than -20dB return loss up to 30GHz. The performance of the interconnect lines *I, II*, and *III* shown in Figure 5.13 is demonstrated in Figure 5.14.

The structure is fabricated with using a gold coated alumina substrate, as it is evident in Figure 5.15. The return loss and insertion loss of all the lines are measured and some of them are shown in Figure 5.16. All the lines show a return loss of better than -20dB up to 30GHz. Overall, the interconnect lines without back-layer transition exhibit a 0.5dB loss at 15GHz and a 1dB loss at 30GHz. The two three-vias of back transitions add

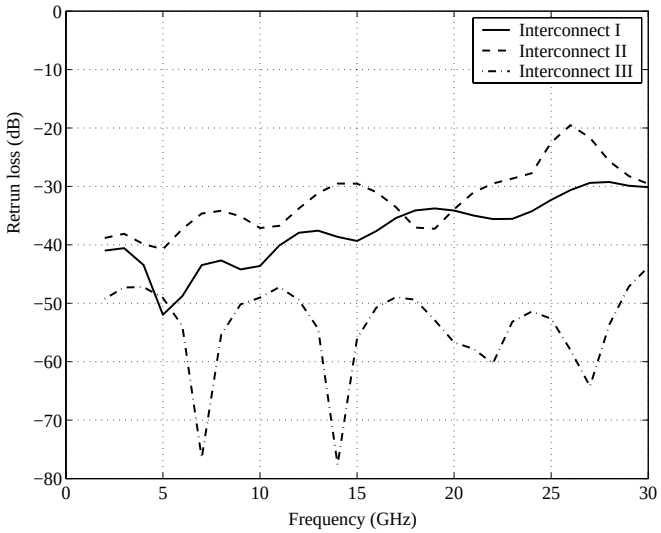

Figure 5.14: Total return loss of interconnect lines I, II, III shown in Figure 5.13 obtained using modified MOM.

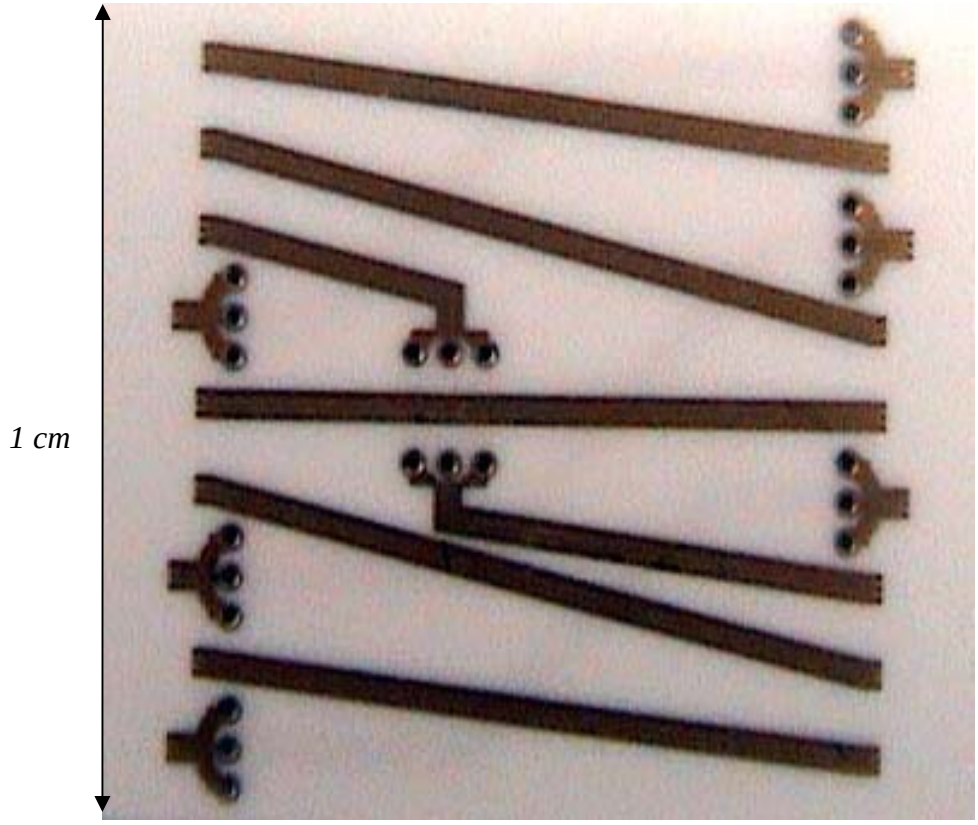

Figure 5.15: Fabricated interconnect network

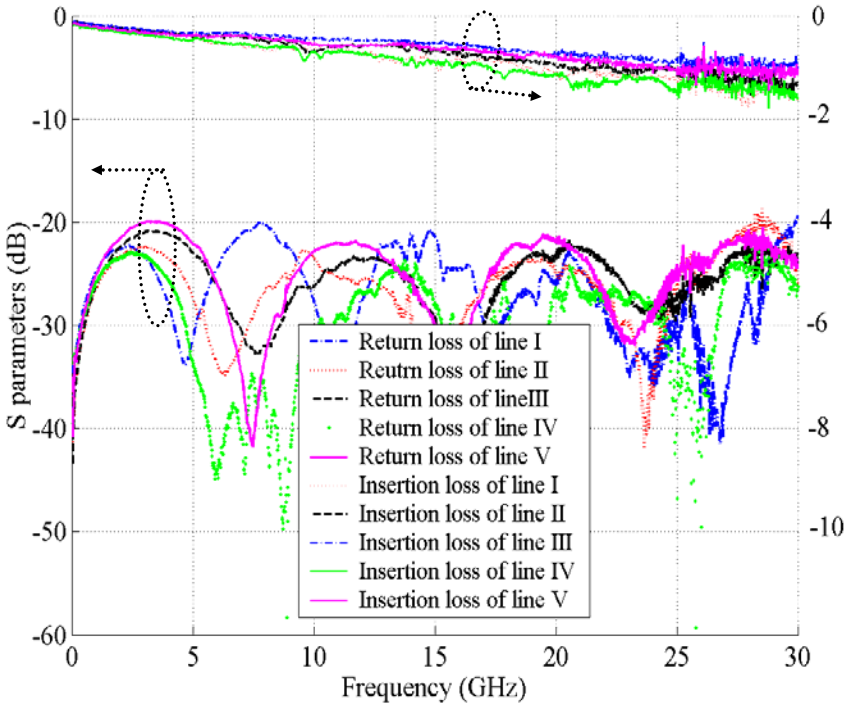

(a)

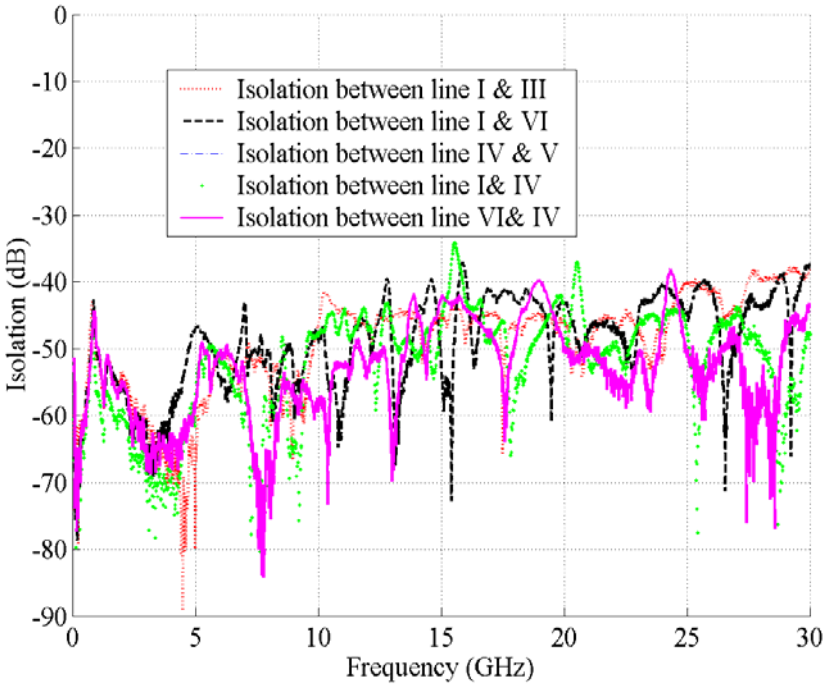

(b)

Figure 5.16: Measured S-parameters of the interconnect network shown in Fig. 9 (a) return loss and insertion loss, and (b) isolation.

0.5dB to these values. These results are in good agreement with those predicted. Also, the isolation between the lines is measured and demonstrated in Figure 5.16 (b). For measurement purposes, the lines are matched to 50Ω thin film resistors. The isolation of about 40dB is measured between any two interconnect lines.

5.4. Via-less Planar Interconnect Network

In spite of the fact that the proposed interconnect network exhibits an extremely good performance, the elimination of the vias is always beneficial. This not only further simplifies the fabrication process but also increases the production yield. Moreover, temperature variation and aging of the circuit can generate some cracks in the vias, resulting in some difficulties in full functionality of the system. In order to solve these problems, we introduce another new interconnect network [83]. In this technique, the vias are eliminated and the entire network is simply fabricated by front and back side metallization. This technique is fully compatible with MIC and MEMS fabrication techniques and can be easily integrated with solid state and MEMS switches [84] and [85].

5.4.1. Coupled CPW Vertical Interconnect

In this technique, a double-sided electromagnetically coupled CPW circuit is used to replace the three-via transitions. It consists of an overlay of two FGC lines at each side of the substrate while electromagnetic coupling transfers the RF signal from one side to the other [86]-[87].

Although the feeding FGC lines carry only even mode, this transition supports both even and odd modes. The dimensions of the overlay region are designed so that the even and odd mode impedances produce a perfect match at the frequency of interest. This results in a quarter wavelength λ/4 long transition, which is shown in Figure 5.17(a). For the 10 mil alumina substrate with ε_r=9.8, the signal line width is w=224μm and the ground line width is w_g=184μm. The spacing between the central line and the ground

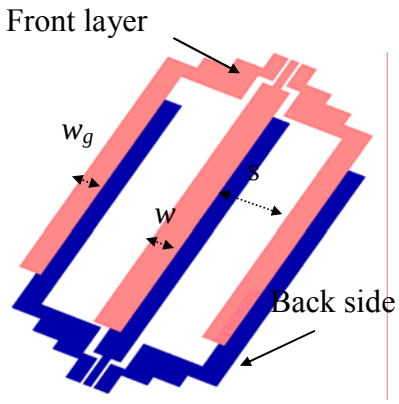

(a)

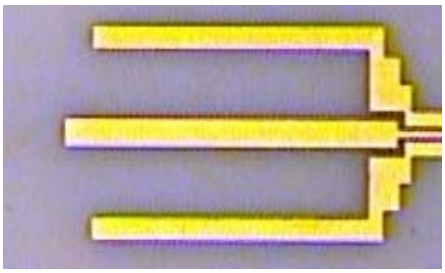

(b)

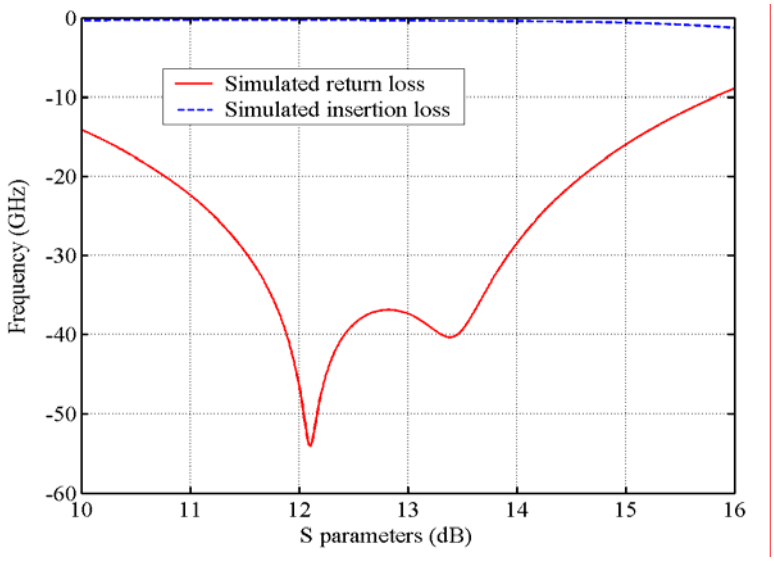

(c)

Figure 5.17: Vertical coupled CPW transition: (a) conceptual schematic, (b) fabricated unit, and (b) measured and simulated S parameters.

planes is one of the most effective parameters in controlling the coupling which is *s*=550μm. This parameter increases by enlarging the substrate thickness. The vertical CPW coupled interconnects are matched to 50Ω FGC lines through an optimized junction.

A full wave analysis using HFSS© is performed to optimize the transition for the

satellite Ku band and the results are given in Figure 5.17(c). It indicates a return loss of better than -20dB between 11-14GHz. The insertion loss is about 0.5dB, which includes the conductor loss and any parasitic radiation.

Discrete RLC modeling of such a transition is not simple due to the lots of interactions in between the lines. Overall, in the frequency range of interest, the common area of the top and back lines creates a large capacitor that couples the top circuit to the backside. By enlarging the overlay area the capacitance increases leading to a better signal coupling.

5.4.2. Double Coupled CPW Vertical Interconnect

In this circuit, the backside of the substrate is used for the crossovers. The double coupled CPW vertical interconnect is utilized to couple the RF signal from the topside of the substrate to the back lines and after the crossover, transfer it again to the top layer. A conceptual schematic of this transition is denoted in Figure 5.18(a).

The focus is to optimize the performance and prevent from any interaction between the vertical coupled interconnects. The parasitic coupling of the coupled CPW lines to the top layer crossing line is also minimized. Each vertically coupled transition individually is similar to that denoted in Figure 5.17(a) which are connected together by a FGC with a signal line width of w=64μm, spacing of s=24μm, and the ground line width of w_g=120μm.

A full wave analysis by HFSS© is applied to design the transitions. The optimized distance of 1200 μm between the vertical transitions results in an isolation of better than -40dB with the crossing line. To confirm the idea, the vertically coupled FGC transition shown in Figure 5.18 (b) is fabricated over a double-sided 10-mil alumina substrate with a gold coating of 4μm. A two port on wafer probe measurement is performed and the results are demonstrated in Figure 5.18(c). It can be seen that a return loss of better than -15dB is obtained from 9.5GHz to 13GHz. The measured insertion loss is close to 0.6dB, and the measured isolation is more than 40 dB.

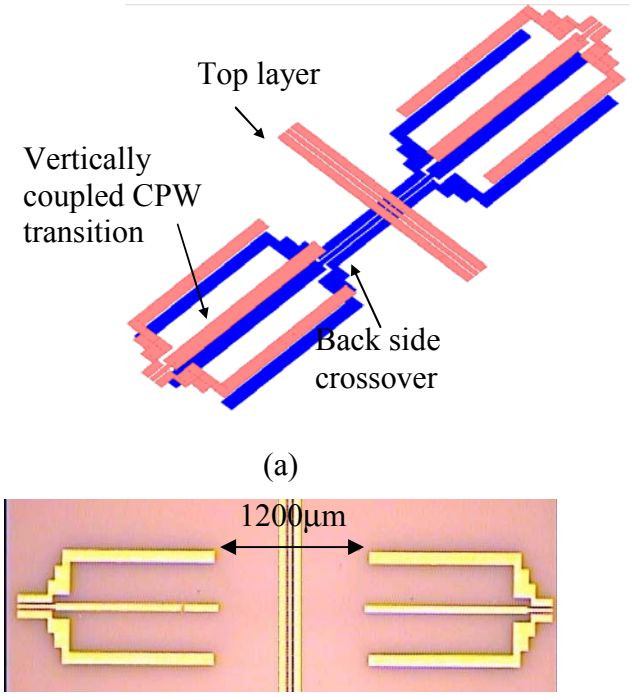

Figure 5.18: Double vertically coupled FGC transitions: (a) conceptual schematic and (b) fabricated unit from top view.

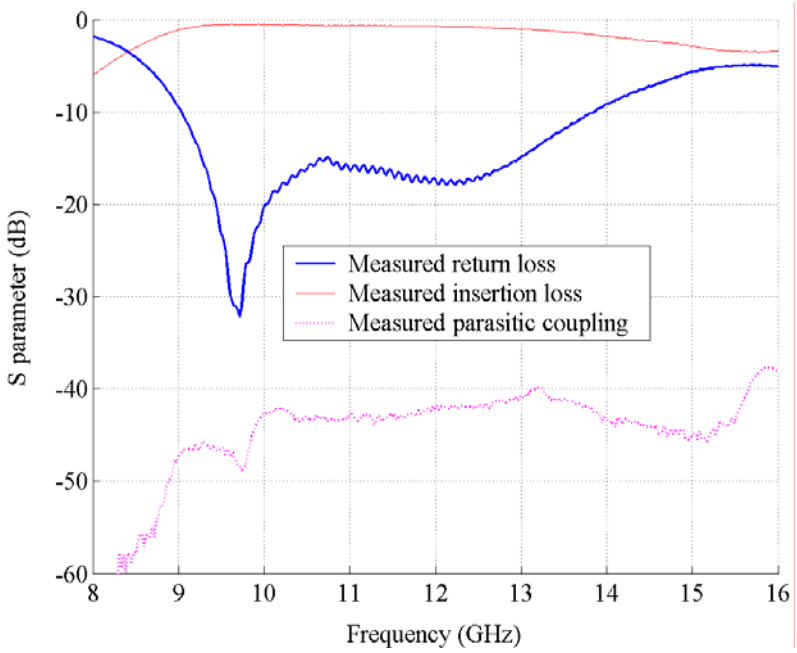

Figure 5.19: Measured results for the vertical coupled CPW interconnect.

5.4.3. Switch Matrix Interconnect Architecture

When several coupled CPW interconnects are printed on a common substrate, electromagnetic waves can induce extra parasitic coupling to the other transitions. This issue can become more problematic when the interconnects are placed in a double-sided network with several transmission lines. To verify this, a 3×3 switch matrix interconnect network is investigated.

Figure 5.20(a) shows the entire interconnect network schematic, which includes the top lines and the back crossovers. It is designed based on pairwise connection for a 3×3 switch matrix. This structure is 1.7cm by 1.8cm and can be easily integrated with CPW SP3T switches [84] and [85]. By avoiding the vias in this configuration, it is well suited for high yield mass production.

The FGC lines are designed to be 50Ω with a signal line width of w=64μm, spacing of s=24μm, and ground line width of w_g=120μm. The transition shown in Figure 5.17(a) is used to transfer the RF signals from one side of the substrate to the other side. For abrupt crossovers, double CPW coupled vertical transition is used. To optimize the entire system, it is divided into several subsections and analyzed using an EM simulator. Then the results are linked together by netlist coding. The optimized configuration is fabricated over a 10mil gold-coated alumina substrate and is depicted in Figure 5.20 (b).

A two port on-wafer probe measurement is performed to evaluate the interconnect network performance and the results are plotted shown in Figure 5.21. For the frequency range of 12-13GHz, the measured results of all the lines indicate a return loss of better than -20dB except for line III, which is -17dB. The insertion loss of the top lines is approximately 0.9dB, which increases about 0.6dB for each vertical transition. Figure 5.21(b)) confirms that an isolation of –45 dB is obtained over the band of interest.

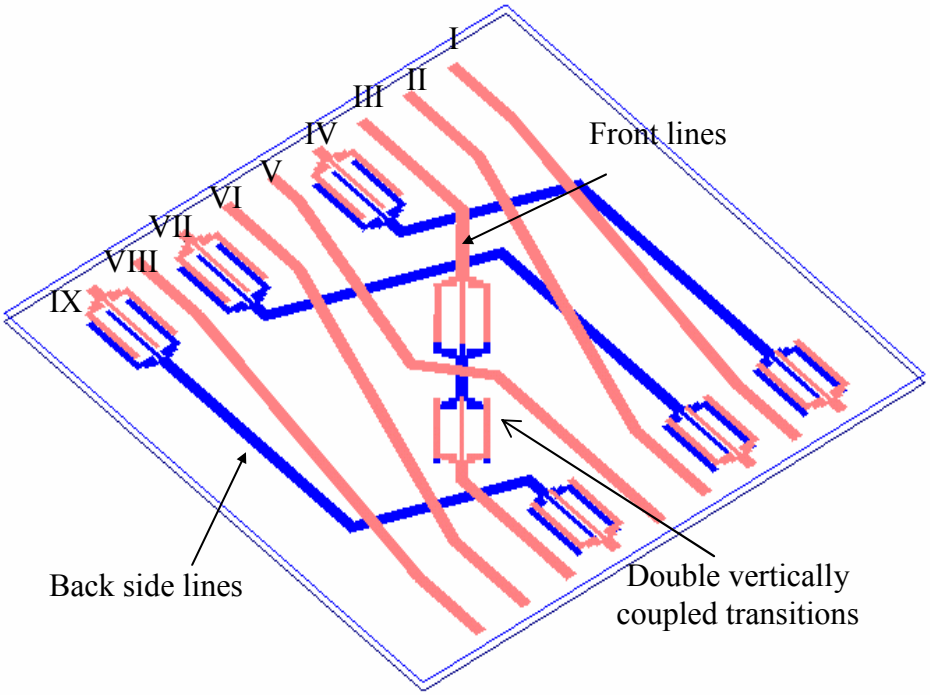

(a)

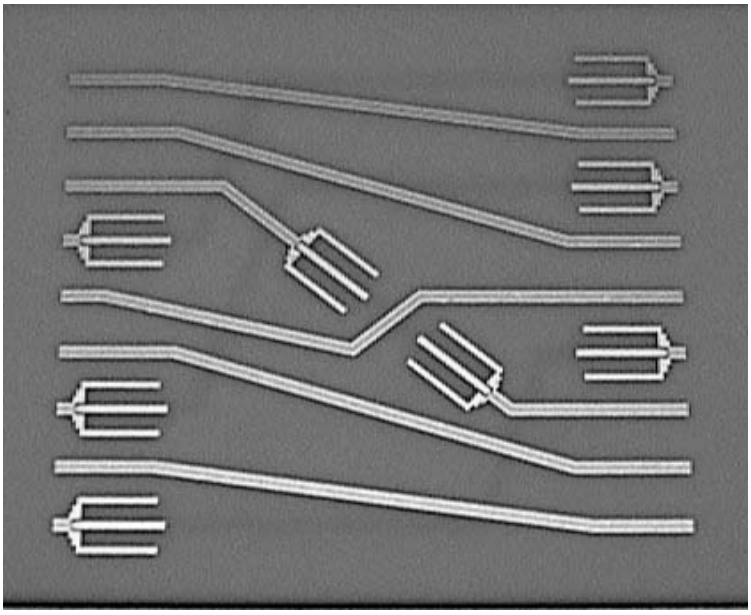

(b)

Figure 5.20 (a) Conceptual schematic and (b) the fabricated unit of the proposed vialess interconnect network.

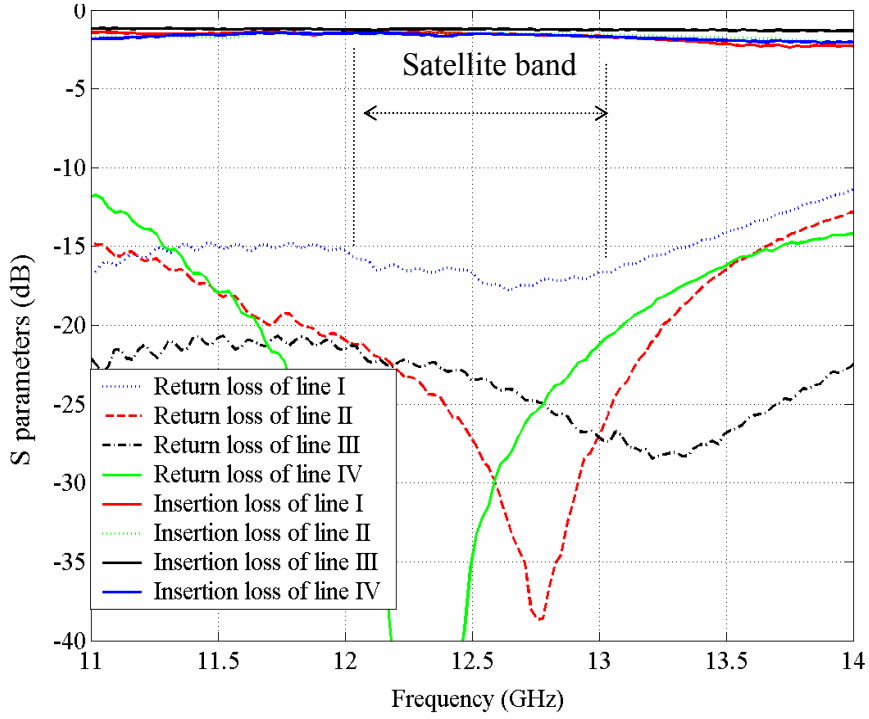

(a)

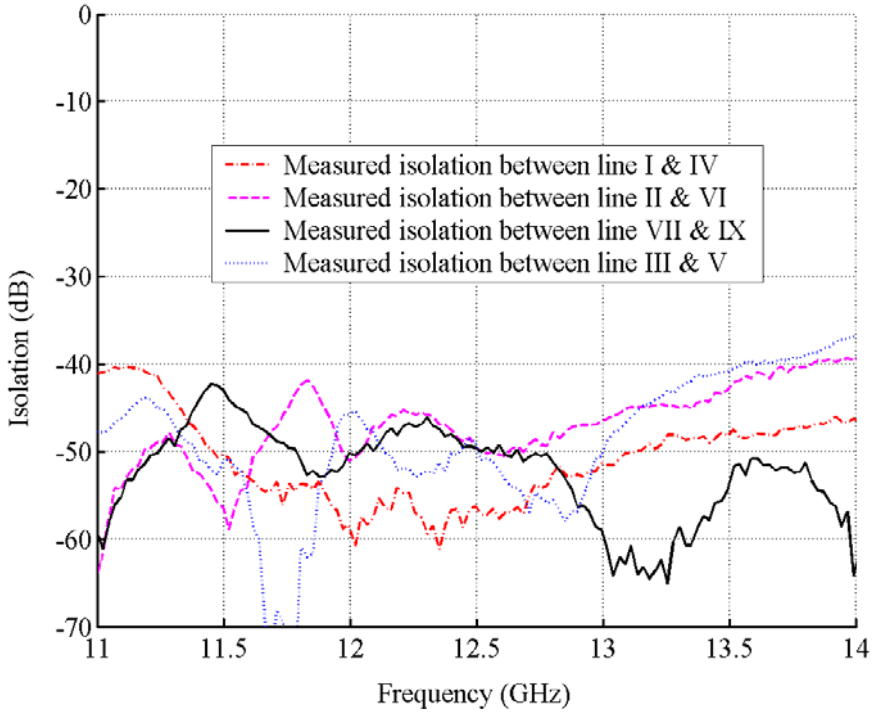

(b)

Figure 5.21: Measured results for the proposed interconnect network shown in Figure 5.20 (a) return loss and insertion loss and (b) isolation.

5.5. Switch Matrix Integration

Incorporating the interconnect circuit with SP3T switches results in the 3×3 RF MEMS switch matrix as shown in Figure 5.22(a). The function of the switch matrix is to route the three input signals to the three output signals in all possible permutations. The compatibility of the interconnect circuit with the newly devised switches provides the facility to fabricate the entire interconnect lines and the switches, monolithically, on one common substrate.

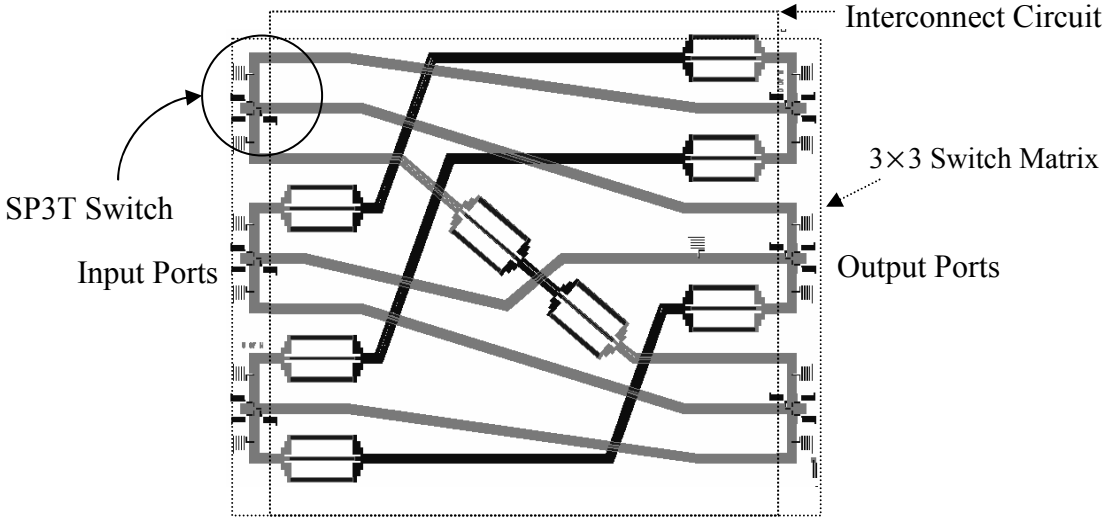

(a)

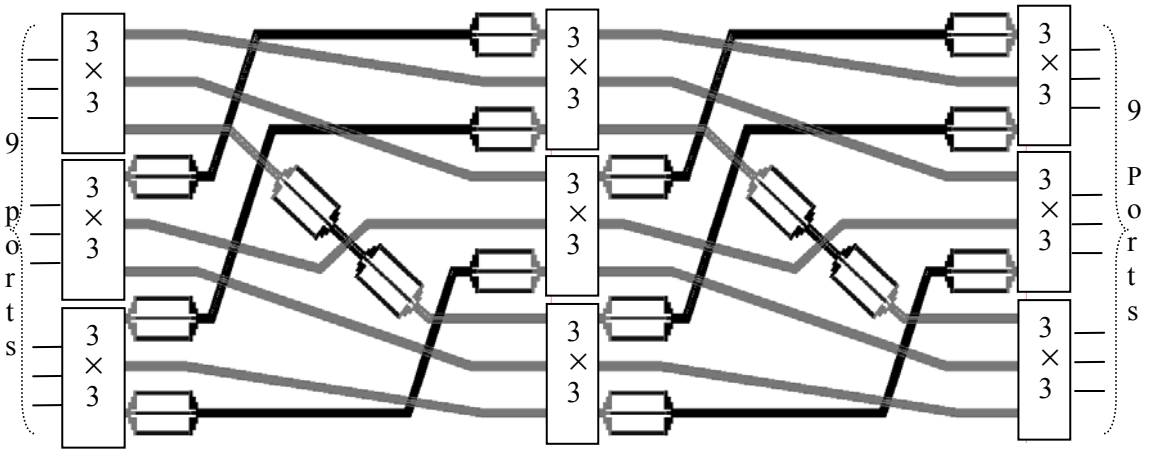

(b)

Figure 5.22: Switch matrix building blocks of (a) 3×3 and (b) 9×9.

Fabrication of the switch matrix is comprised of the simultaneous processing of all the interconnect lines and the MEMS switches within one chip and with only one type of process. To prove the concept, a 3×3 matrix prototype unit is fabricated. An alumina wafer is selected as the base substrate since it can retain its intrinsic properties during the process. Also alumina substrate exhibits a good RF performance at high frequencies. Monolithic fabrication by adopting the thin film process requires a total of seven mask levels to pattern the different layers.

A summary of the fabrication procedure is shown in Figure 5.23. Initially, a gold film is deposited at the back side of the substrate. This film is patterned for the transitions and crossovers. Afterwards, a Kapton tape is used to protect the backside while processing the switches and the interconnect network on the front side. The rest of the process follows the procedure similar to that of explained in section 3.3.1 [90]. The front side of the interconnect network is patterned on the first gold layer simultaneously with the SP3T switches.

Figure 5.24 illustrates the fabricated 3×3 monolithic switch matrix in the CIRFE lab at the University of Waterloo. SP3T switches (details on the SP3T switch are given in section 3.3.1) are integrated with the interconnect lines monolithically. Figure 5.24 (b) shows one of the switches and the vertically coupled transitions from a close view. The back side of the matrix is shown in Figure 5.25.

The entire switch matrix performance is measured and presented in Figure 5.26 and Figure 5.27. The -15dB return loss bandwidth of the switch matrix is from 9.5GHz to 13.5 GHz which is much wider than the presented interconnect network in section 5.4.3. This is accomplished with a better alignment of the top and the back side of the vertically coupled transitions. The insertion loss between the input port 1 to output port 1, input port 2 to output port 2, and input port 3 to output port 3 is 2.2dB that includes the effect of the switches at each end. For instance, at 12GHz, each switch has 0.6dB loss which leaves a 1dB loss for the CPW lines. The other few paths that utilize

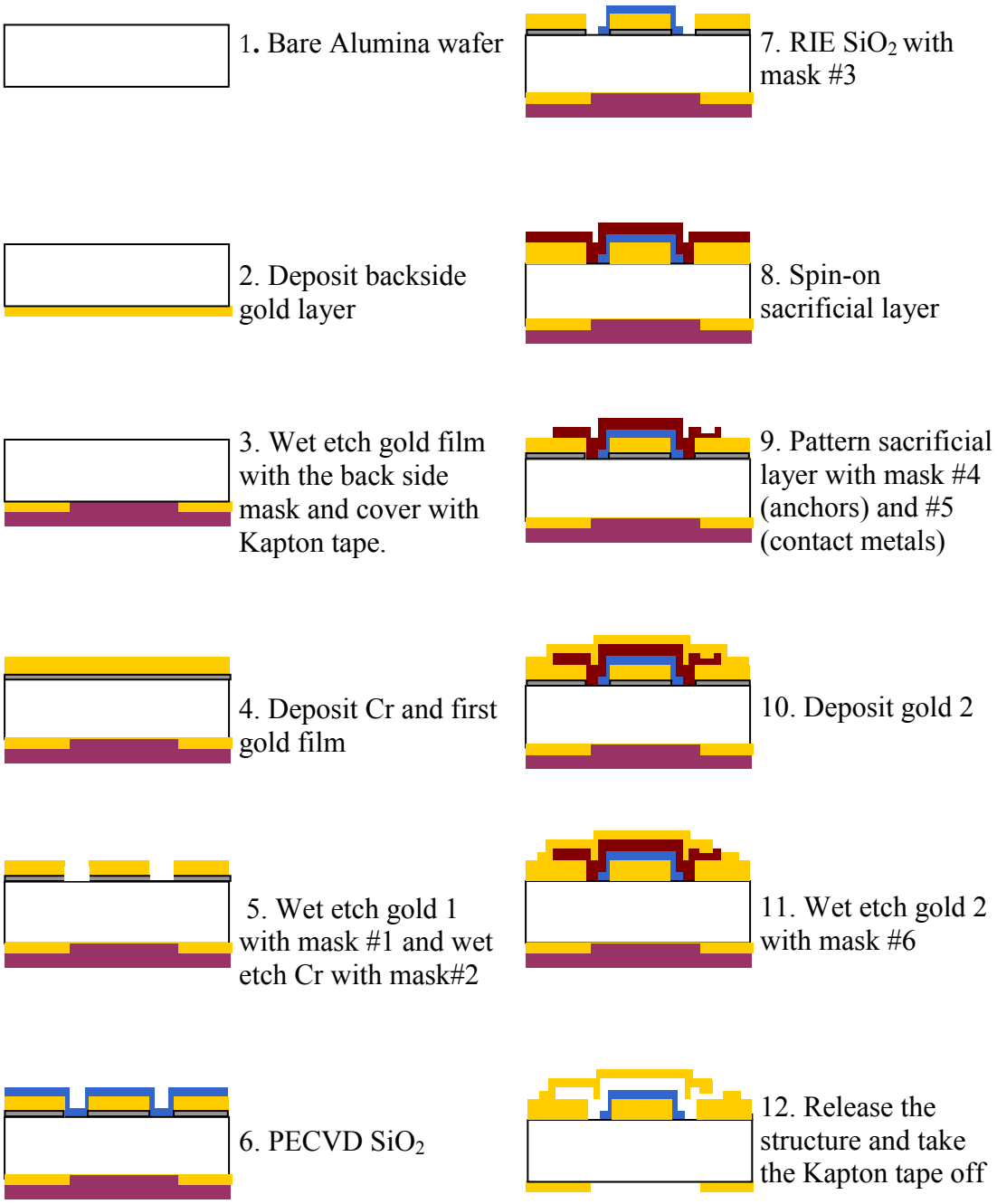

Figure 5.23: Fabrication process for the proposed monolithic switch matrix shown in Figure 5.22(a).

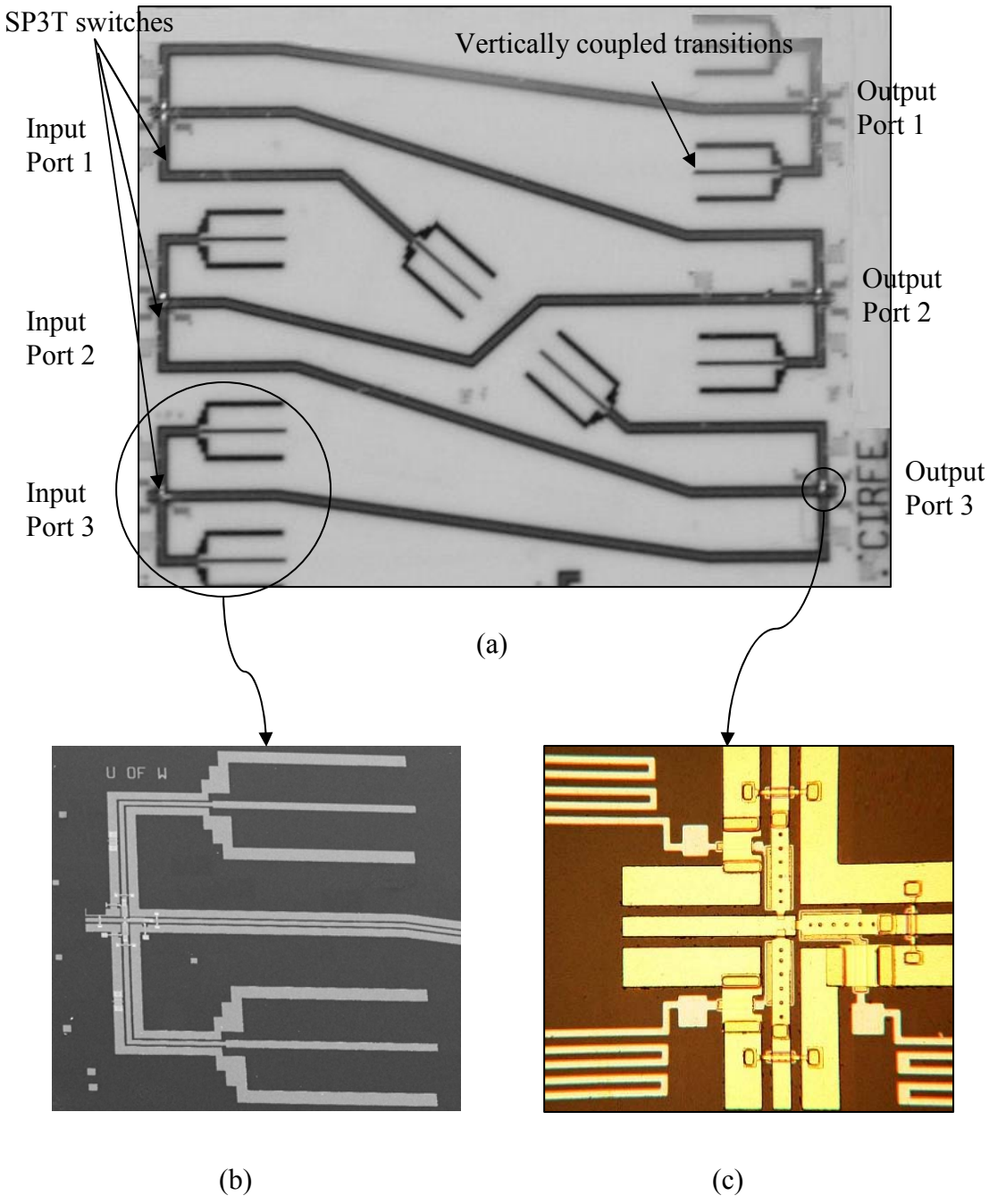

Figure 5.24: (a)Fabricated 3×3 monolithic switch matrix at the CIRFE lab at the University of Waterloo, (b) One of the switch matrix input ports including the switch and the vertical coupled transitions, (c) SP3T switch.

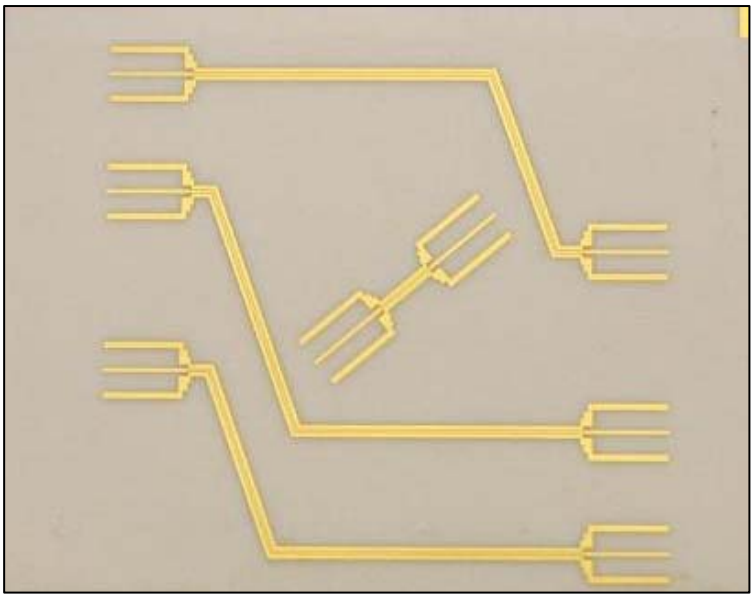

Figure 5.25: Back side pattern of the fabricated monolithic switch matrix at the CIRFE lab at the University of Waterloo

electromagnetically coupled transitions demonstrate about 1dB increase in insertion loss. The isolation of the switch matrix is also investigated and the measured results are presented in Figure 5.27. It illustrates an excellent isolation of better than 45dB for the frequency band of interest. It should be noted that the isolation is measured while all switches are in the off state.

In comparison with the only previously reported switch matrix [32], the proposed network operates over a much higher frequency range and offers a much better isolation. This matrix structure can be packaged and used as a basic building block for larger structures. Alternatively, Clos network (shown in Figure 5.22 (b)) can be used to expand it to bigger structures over one common substrate. For instance, Figure 5.22 (b) shows a 9×9 switch matrix configuration which is made of the same type of interconnect architecture and 3×3 swtich matrices as building blocks.

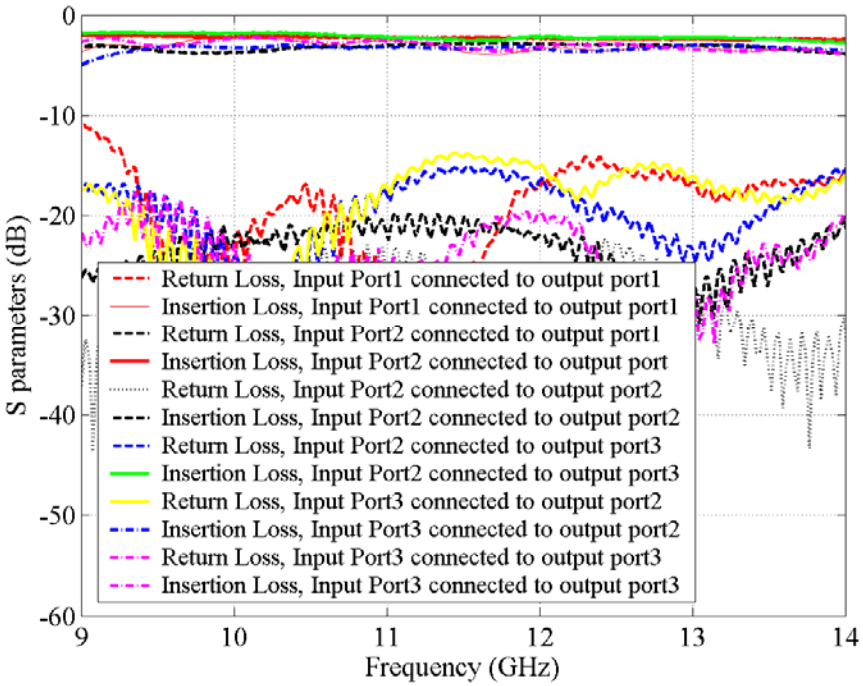

Figure 5.26: Measured return loss and insertion loss of the fabricated switch matrix shown in Figure 5.24.

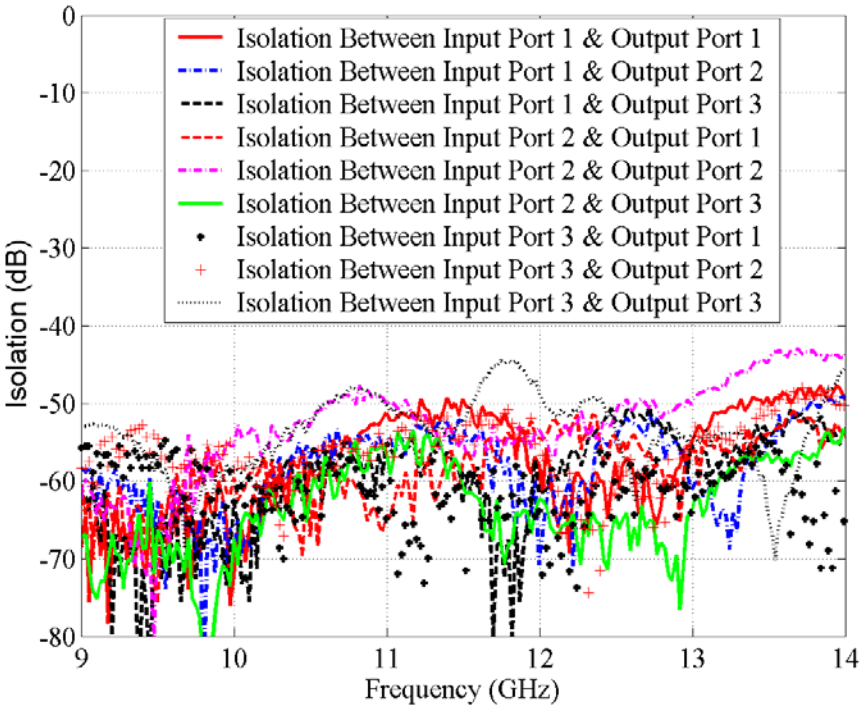

Figure 5.27: Measured isolation of the fabricated switch matrix shown in Figure 5.24.

5.6. Conclusion

In this chapter, for the first time, a monolithic RF MEMS switch matrix has been developed and studied in details. This involves simultaneous fabrication of the switches and interconnect network. Two different networks that are amenable to MEMS fabrication process and the SP3T switches have been proposed and confirmed both theoretically and experimentally.

Primarily, a broad band interconnect network is proposed that employs FCG lines integrated with 3-vias vertical transitions. The parasitic couplings and vertical transitions have been investigated both theoretically and experimentally. Single and double 3-via vertical transitions are designed and optimized to provide a return loss of 30dB up to 30GHz. A complete 3×3 interconnect network has been fabricated and tested. It exhibits a measured return loss of better than -20dB and isolation of better than 40dB up to 30GHz.

In addition, another novel interconnect network is introduced that utilizes FGC lines and single and double coupled CPW vertical transitions. This network avoids the use of vias and is very suitable for high yield mass production. A complete 3×3 interconnect network is fabricated and measured. The results for the individual transitions and for the whole interconnect networks demonstrate the validity of the concepts recommended in this chapter.

The coupled interconnect network is monolithically integrated with the SP3T RF MEMS switches proposed in Chapter 3. A thin film fabrication process exclusively for switch matrix fabrication is developed and fine tuned. A prototype unit of 3×3 switch matrix is fabricated and tested. The measured results show a good RF performance for the frequency range of 9.5GHz to 13.5GHz.

Chapter 6

Conclusions

6.1.Thesis Contributions

The major contributions of the thesis can be summarized as follow:

Novel multi-port RF MEMS switches such as SP3T, C-type and R-type switches have been proposed and investigated. The switches have been realized using three different approaches. Initially, cantilever beams were fabricated by the Poly MUMPs process. Then they were integrated with alumina substrate by using flip chip technology resulting in low insertion loss and good isolation. The hybrid integration can be employed to circumvent the losses of the silicon based Poly MUMPs process. The process is costly and the yield is substantially low. To overcome this problem, the second approach was considered and a new in-house monolithic fabrication process has been developed and fine tuned using six different mask layers. In addition, thermally actuated multi-port switches are investigated. These switches that include SPST, SP2T and C-type configurations are based on lateral contact and fabricated monolithically by using the Metal MUMPs process.

The thesis has introduced a novel concept for 3D RF MEMS switches based on integrating MEMS actuators with waveguide structures. Fabricated prototype units of rectangular ridge waveguide and coaxial lines with integrated thermal and electrostatic rotary MEMS actuators have been analyzed. Prototype units for both ridge and coaxial MEMS based SPST and C-type switches have been fabricated

and tested. The measured results verify the concept demonstrating a good return loss of -20dB and a high isolation of 35-40dB over band of interest. High power test and analysis reveal no major change in the switch performance up to 13W. These switches are not only extremely useful for high power applications but also promise to be useful for high frequencies and millimetre-wave applications.

The proposed planar multi-port switches in this thesis, have been monolithically integrated with an interconnect network to construct a switch matrix on a single chip. A fabrication process for the monolithic fabrication of the entire switch matrix has been proposed. Furthermore, innovative amenable interconnect networks based on patterning the interconnect circuit on both sides of an alumina substrate have been introduced. The interconnect networks employ finite ground CPW lines that are optimized to avoid crosstalk. Three-via and electromagnetically coupled vertical transitions are employed to transfer the signal from one side of the substrate to the other side. The approach provides the opportunity to implement the entire switch matrix structure monolithically by using a thin-film process and also avoiding the need for hybrid integration with thick-film multi-layer substrates.

Overall, the focus of this thesis has been on multi-port switches and switch matrices for redundancy and signal routing in satellite communication. These switches are compared in Table 7.1. We believe that MEMS technology has a great potential to replace the existing switch matrix technology in satellite payloads. However, there are many hurdles to overcome in order to achieve this goal. This list includes packaging and reliability which is addressed in section 7.2 under future work. A successful qualification of RF MEMS devices for space applications requires collective efforts from RF, Mechanical, and Material Engineering.

Table 7.1: Comparison of the proposed switches in this research

	2D Electrostatic RF MEMS Switches	2D Thermal RF MEMS Switches	3D Electrostatic Waveguide MEMS Switches	3D Electrostatic Coaxial MEMS Switches
Power Handiling	Low	Low	High	Meduim
Size	small	small	Large	Meduim
Bandwidth	Wide	Wide	Narrow	Wide
Power Consumption	~0	590 mW	~0	~0

6.2.Future Work

Although the research for this thesis has been extensive, there are still several unexplored issues that can be summarized as follow:

- The presented planar switches are prototype units that prove the concept. Optimizing the switching time and performing reliability test may be the next step toward producing a steady high quality switch. A low cost packaging technique must be also investigated as ultimately this step determines the cost and reliability of the switch. Contact MEMS switches are very sensitive to humidity and contaminations and therefore, they must be packaged using hermetic seals and in nitrogern or dry air environment. Substrate transfer or localized heating are two possible solutions [57].

- The novel 3D MEMS devices open the door for revolutionary MEMS-based waveguide switches. The proposed prototype units demonstrate the concept yet there are still several unsolved matters. The power test analysis is only performed up to 13W and higher power analysis and experiments are recommended as future work. Monolithic realization of the switches especially for millimetre-waves is

one of the main subjects that require a thorough study. For final packagin of the switches and itegration in a system, the top and the bottom parts of the waveguide swtich should be attached using a conductive solder bonding and hermatically sealed. The bonding material should be chosen in a way to minimize the outgassing of the package.

- The novel switch matrix is a new technique to avoid thick-film substrates and fabricate the entire switch matrix monolithically using a thin film MEMS process. The monolithic 3×3 switch matrix has demonstrated the concept. Further study of the concept and expansion of that to larger matrices using Clos or other well known networks is useful. Hermetic RF packaging of the entire matrix to prevent the swtiches from humidity and organic materials must be also considered. The integration of DC control board is the next necessary step toward having a fully functional switch matrix.

- In general, the reliability of RF MEMS devices has not been proven in space environment. Most have been only demonstrated with lifetime tests which often do not accurately replicate typical operating conditions in targeted space systems. Packaging is another key chanllenge that needs to be considered at the development stage. Failure to do that would generally results in inferior RF MEMS devices with poor yield [91]. Overll, reliability and packaging are the most two common issues of the existing RF MEMS switches.

Appendix A

Electrostatic Cantilever Actuator

Figure A.1 illustrates a cantilever actuator anchored to a 50Ω CPW signal line. The actuator is suspended over a discontinuity followed by the second CPW signal line. The electrode is incorporated on the ground plane under the beam and the beam is fabricated using the Multi-User MEMS Processes (MUMPs) surface micro machining. Each beam is made of a Polysilicon layer of 1.5μm coated by a gold layer of 0.5 μm. Then, the beam is flipped on top of the substrate. The design dimensions are optimized leading to the beam length L=240μm, beam width W=60μm and electrode length L_e=120μm.

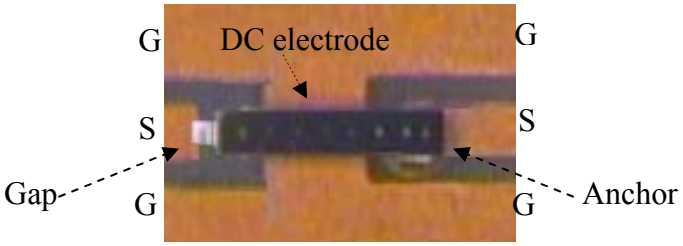

Figure A.1 : Cantilever electrostatic beam

To obtain a better insight into the beam functionality, the beam's electromechanical modeling is studied [89]. As shown in Figure A.2 , the cantilever beam can be simply modeled by a movable plate and a basic electrostatic actuator with a spring constant of k and a mechanical damping of b. Electric potential between the beam and the electrode is also represented by a voltage source, V_{in}.

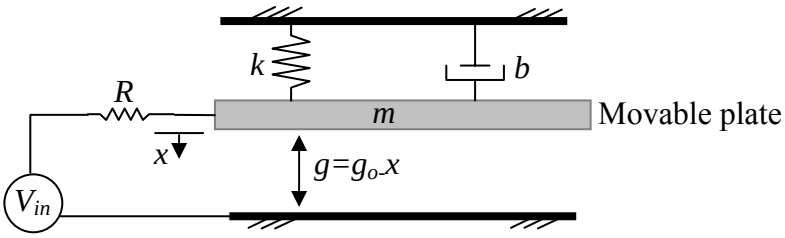

Figure A.2 : Electrostatic actuator electromechanical model

The electrostatic force F_e generated by the attraction between the movable plate and the electrode is related to the geometry by:

$$F_e = \frac{\varepsilon_o A V_{in}^2}{2(g_0 - x)^2} \tag{A.1}$$

where A is the area of the bias electrode, g_o is the initial gap between the electrodes, ε_o is the dielectric constant of the material (the air in this case) between the electrodes, and V_{in} is the applied voltage. This is the force that stretches the spring and pulls the actuator down. Consequently, the generated spring force, which pulls the beam up, can be obtained from the following equation:

$$F_m = kx \tag{A.2}$$

where x is the plate displacement.

By using equations (A.1) and (A.2), the electrostatic and mechanical forces for the initial gap $g_o = 4\mu m$ are calculated and presented in Figure *A.3*. Considering stability of the equilibrium, electrostatic force must be equal to the spring force. Additionally, at the stable point, by perturbing the position slightly the overall force must tend to return to the equilibrium position. This situation is satisfied only at the first intersections of the electrostatic forces and the mechanical force. Clearly, since the equilibrium gap decreases with increasing the voltage, there is a particular voltage at which the stability of the equilibrium is lost. This is called the pull in voltage of the actuator and is specified when

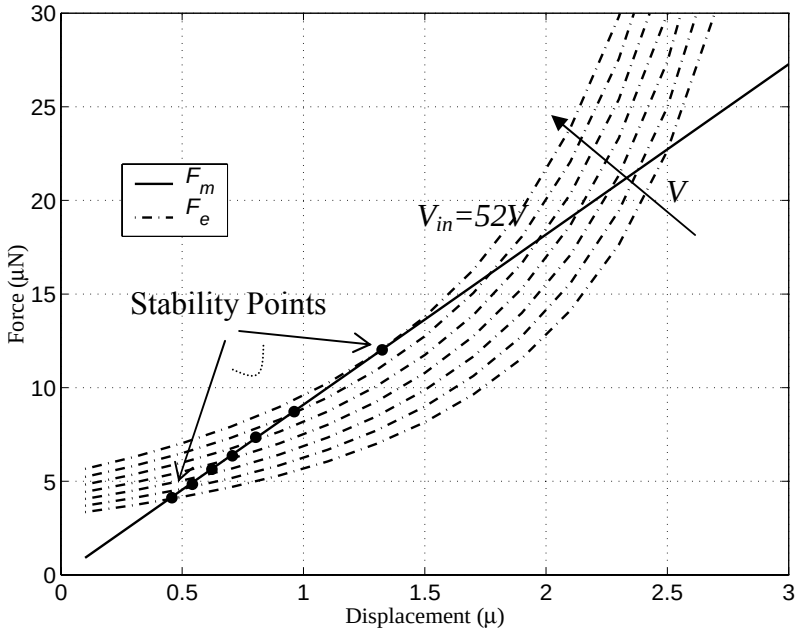

Figure A.3: Mechanical forces F_m and electrostatic force F_e for various input voltage in terms of displacement for the beam model shown in Figure A.2 .

the electrostatic force is tangent to the mechanical force. As is depicted in this figure, the pull in voltage is equal to 52 volts and happens at $x=1.34\mu m$ equivalent to one third of g_o.

Figure A.4 (a) and (b) illustrate the realized beam cross section. 2μm of polysilicon is added at the beam tip to prevent it from reaching to the pull-in condition (this will be explained later). Assuming that the electrostatic force has uniform distribution along the electrode, it can be substituted by a point force in the middle. Then, x and θ that are the displacement and the rotation angle of the beam at point $L_o+L_e/2$ respectively can be obtained:

$$x = \frac{F_e(L_o + \frac{L_e}{2})^3}{3EI} \tag{A.3}$$

$$\theta = \frac{F_e (L_o + \frac{L_e}{2})^2}{2EI} \tag{A.4}$$

where E is the polysilicon Young's modulus, and I is the inertia moment of the cantilever beam. Geometrical approximation along with equations (A.3) and (A.4) are used to acquire the beam deflection under the electrostatic load. Figure A.5 illustrates the beam displacement at the tip and $L_o+L_e/2$ versus the electrostatic force. It is evident that for the tip deflection of 2μm, equivalent force of 5.7μN is required. It leads to a 0.63μm deflection at $L_o+L_e/2$ which is much less than that of the pull-in state 1.34μm. With this force and equation (A.1), a turn ON voltage of 45 volts is calculated.

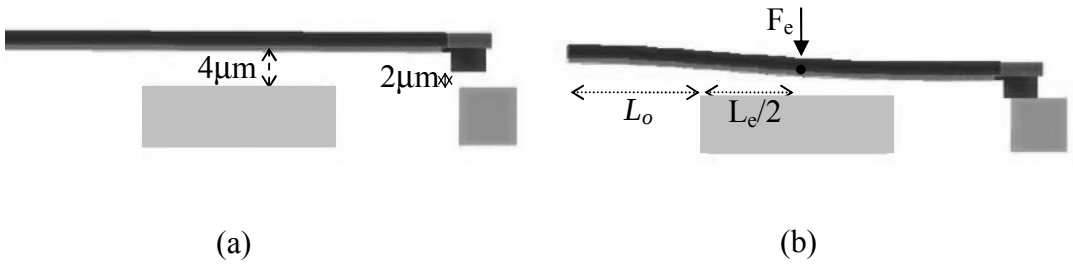

Figure A.4: Designed cantilever beam from crosssection at (a) OFF and (b) ON states.

As an alternative, a full wave FEM analysis by using Coventorware software is performed to confirm the results. As denoted in Figure 3.5, a turn ON voltage of 40 volts is predicted. Figure A.4 (b) portrayed the beam deformation at 70V including the tip blockage effect indicating a good margin above the turn on voltage that the beam does not collapse to the electrode. Contact force of the tip is also simulated leading up to 10μN at 80 volts, as denoted in Figure A.6.

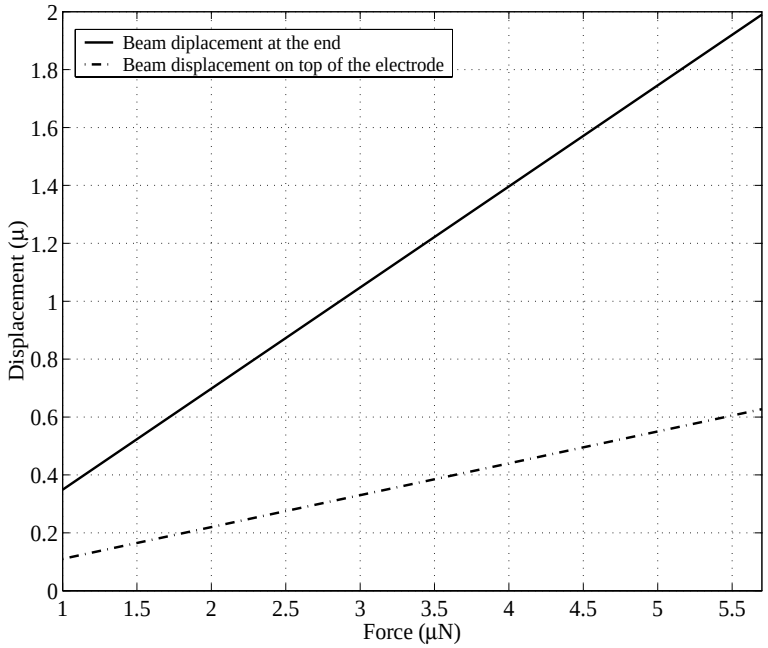

Figure A.5 : Deflection of the beam in Figure A.4

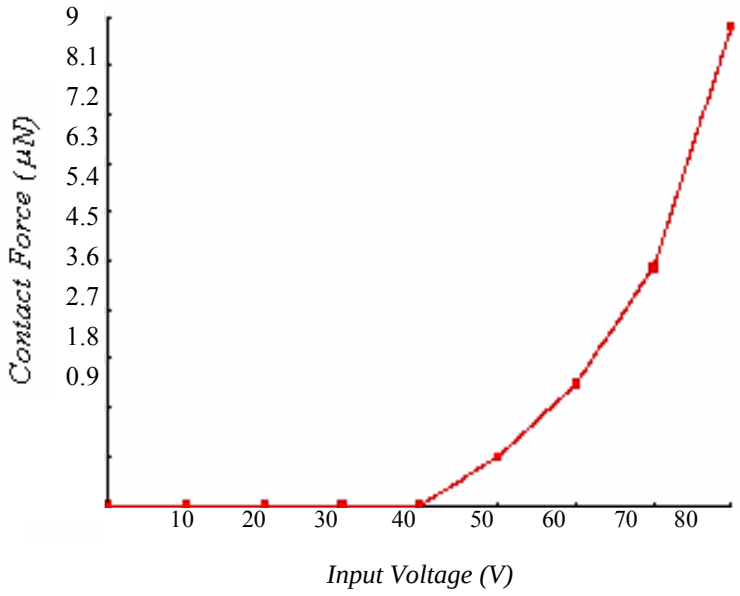

Figure A.6: Contact force at the tip of the beam.

Appendix B

Vacuum and Low Temperature Performance of the Proposed Thermally Actuated 2D Switch

Here, in this section, the proposed switch performance in low temperatures (77K degrees) as well as at room temperatures under vacuum is investigated and analyzed. Low temperature functionality of these switches facilitates their integration with superconductor devices which are the dominant components in extremely low loss satellite systems.

As it is known, at room condition, there are three mechanisms of heat flow: conduction, convection and radiation. According to [55], the heat dissipation through radiation to the ambient can be neglected in comparison with the heat losses through conduction to the anchors which are considered as heat sinks and the heat losses through air due to convection. Therefore, it can be said that under steady state conditions, the resistive heating power generated in the element is equal to the heat conduction and convection from the element. This can be written as [56]:

$$q_j - q_c - q_h = 0 \tag{B.1}$$

where q_j is the generated heat from the electric current, and q_c is the dissipated conduction heat through the anchors. q_h is the lost power through the convection and is equal to

$$q_h = Ah(T - T_o) \tag{B.2}$$

A is the exposed area to air, h is the thermal conductivity of the ambient, T and T_o are the actuators and the ambient temperature respectively. At room temperature, not only the generated heat in the thick arm is much less than that in the thin arm due to less resistance, but the convection is also much higher because of its bigger composed area "*A*" (See Equation (B.2)). Therefore, the thin arm temperature gets much higher and it expands more while the thick arm is acting as a rigid solid. This produces a forward movement.

In vacuum, the scenario is different since there is no convection ($q_h=0$). Initially, in the existence of a high resistance in the thin arm and the absence of convection in the surrounding area, the thin arm heats up and consequently undergoes plastic deformation. When the DC bias is removed it is newly configured and is longer than the original length. However, the thick arm only undergoes elastic deformation and returns to its original length at the rest condition. Therefore, the actuator assumes a new geometry and the longer length of the thin arm produces a forward movement and thus, the switch enters the contact mode (ON state) as drawn in Figure B.1.

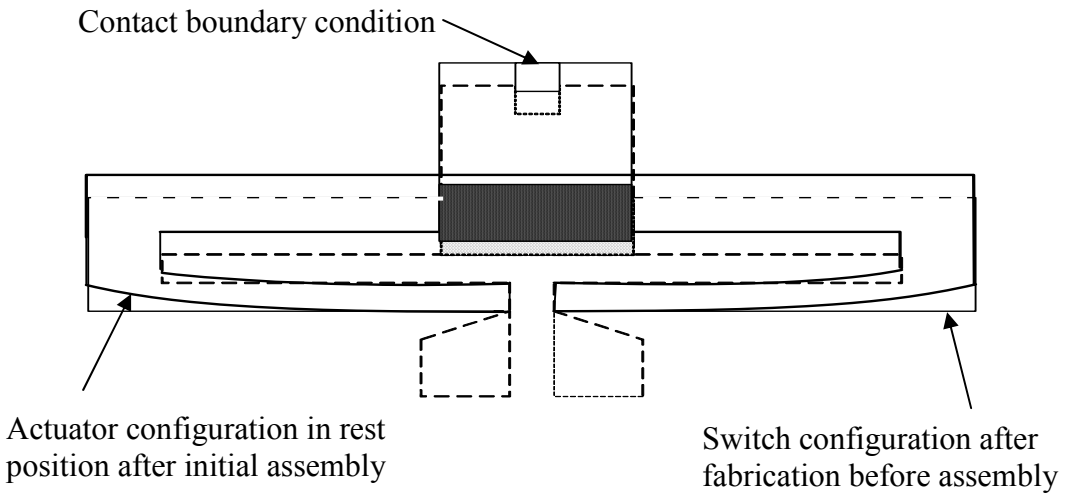

Figure B.1: The proposed switch configuration after initial assembly in Vacuum only and in 77 K degree.

The movement of this type of actuators in vacuum is analyzed in [55] in details. As it is predicted, by the application of the current in the absence of convection (vacuum), the generated heat results in a temperature distribution that initiates a backward movement. In other words, for the thin arm as well as the thick arm, the temperature increases and both arms expand. This leads to a backward movement of the actuator and thus, the switch turns OFF. When the DC bias is removed the switch turns back ON to its rest position.

In a vacuum and the absence of convection, the efficiency of the switch is enhanced and dissipated loss is drastically reduced. Several experiments are carried in the Cryo vacuum prober, pictured in FigureB.2. The results reveal that the required voltage for the switch operation is 0.8V and the current is 170mA. This represents a 136mW power consumption which is 75% less than that at room condition (590mW).

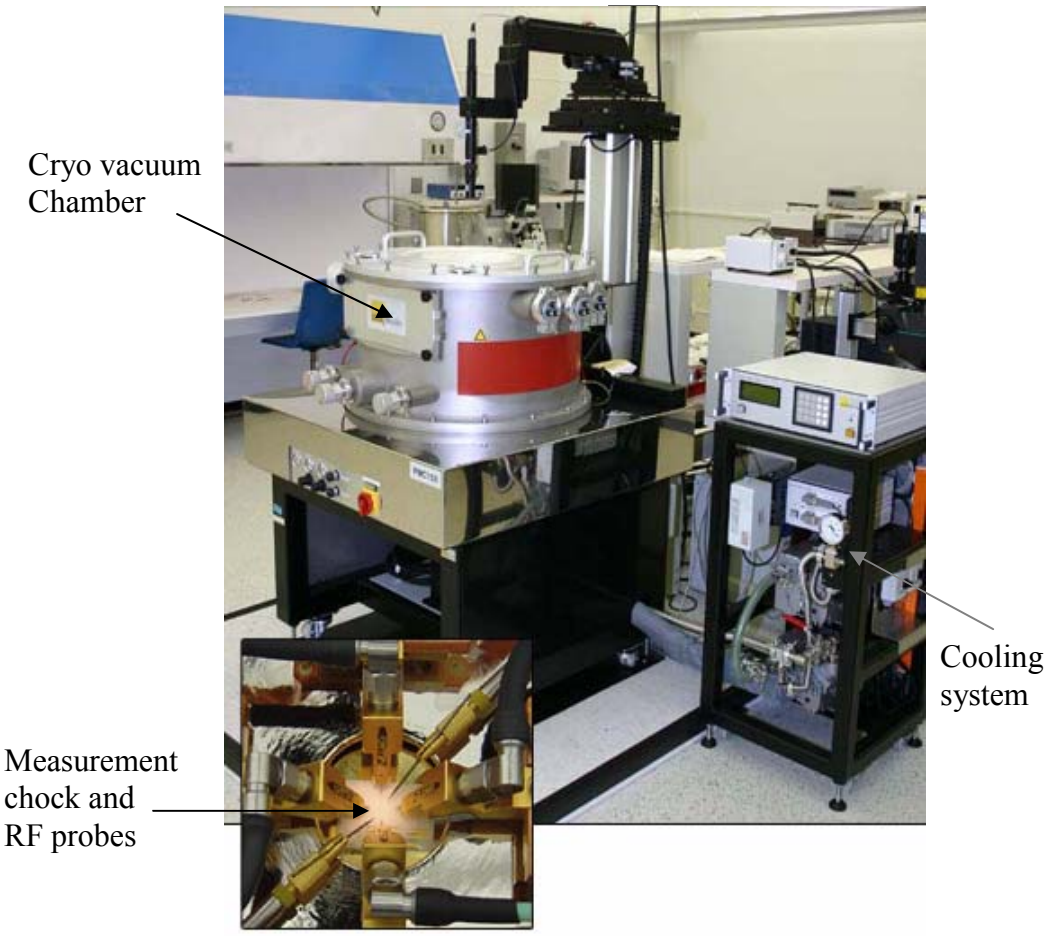

FigureB.2: The SUSS Cryo RF prober in the CIRFE lab.

Here, the switch performance at temperatures of as low as 77K degree is investigated and several experiments were carried out. It is demonstrated that the operation of the switch is similar to that in the vacuum. This is due to the fact that in the vacuum, the actuator is isolated from the surrounding area except at the anchor points where the temperature is much lower. Therefore, the only difference with the vacuum is the consumed power which is slightly higher. The required voltage is measured around 1.1V for a 220mW consumption of power. Nevertheless, it is still much less than that at room condition.

Additionally, RF performance of the switch is evaluated and the results are recorded in Figure B. As it is expected, both in the vacuum and at room temperature, the switch has identical RF performance. By reducing the temperature, the resistivity of the silicon increases which leads to a lower substrate loss. The measured data for the proposed switch exhibit an improved performance of 0.8dB insertion loss at 20GHz for the temperature of 77K degrees. However, the isolation is degraded slightly at high frequencies due to the increase in parasitic coupling through the ground planes.

The mechanical and RF analysis of the proposed switch, contemplated in this section, highlights the suitability of this type of MEMS switches for space applications where it must operate in extremely low temperatures.

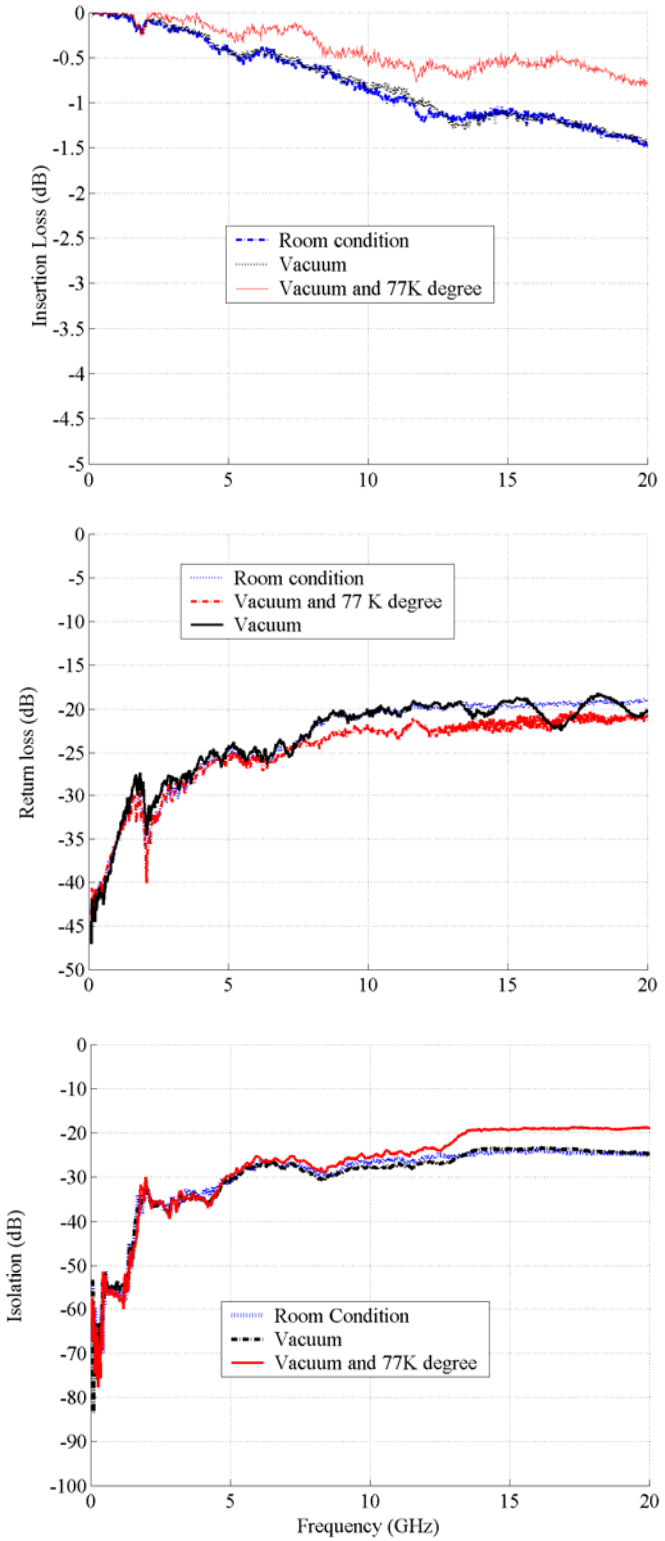

Figure B.3: Proposed switch performance at room condition, vacuum, and 77K degree

Thesis Publication List (As of Nov. 2005)

Journal Papers:

[P1] M. Daneshmand, and R.R. Mansour, "Multi-port MEMS-Based Waveguide and Coaxial Switches", *IEEE Transactions on Microwave Theory and Techniques*, p.1-7 Nov. 2005.

[P2] M. Daneshmand, R. R. Mansour, P. Mousavi, S. Choi, B. Yassini, A. Zybura, and M. Yu, "Integrated Interconnect Networks for RF Switch Matrix Applications", *IEEE Transactions on Microwave Theory and Techniques*, January 2005.

[P3] M. Daneshmand, R. R. Mansour, and N. Sarkar, "RF MEMS Waveguide Switch", *IEEE Transactions on Microwave Theory and Techniques*, Vol.52, issue 12, pp.2651-2657, Dec. 2004

[P4] M. Daneshmand and R. R. Mansour, "Hybrid Integration of Multi-port RF MEMS Switches", Canadian Journal of Electrical and Computer Engineering, Nov. 2005 (submitted).

Conference Papers and Poster Presentations

[P1] M. Daneshmand, R. R. Mansour, "RF MEMS Waveguide C-switch", Canadian Workshop of MEMS (CWMEMS), August 2005, **(Best Paper Award)**.

[P2] M. Daneshmand, and R. R. Mansour, "Multi-port Waveguide Switches", IEEE IMS 2005, IEEE MTT-S Int. Microwave Symp. Digest, Long beach, CA, June 2005.

[P3] M. Daneshmand, R. R. Mansour, "RF MEMS Switches for Wireless Communication Applications", CITO Innovators Showcase, Toronto, Ontario, Nov. 2004, **(Best Student Presenter Award).**

[P4] M. Daneshmand, R. R. Mansour, N. Sarkar, "RF MEMS Waveguide Switch", 2004 IEEE MTT-S Int. Microwave Symp. Dig. Jun. 2004.

[P5] M. Daneshmand, R. R. Mansour, P. Mousavi, S. Choi, B. Yassini, A. Zybura, and M. Yu, "A Novel Integrated Interconnect Network for RF Switch Matrix Applications", 2004 IEEE MTT-S Int. Microwave Symp. Dig. Jun. 2004.

[P6] M. Daneshmand, and R.R. Mansour, "Fabrication and Modeling of an SP3T RF MEMS Switch", 2003 IEEE Antennas and Propagation Symposium and URSI Radio Science Meeting Dig. Vol.1, pp. 391-394, 2003.

[P7] R. R. Mansour, M. Bakri-Kassem, M. Daneshmand, and N. Messiha, "RF MEMS Devices", The 2003 International Conference on MEMS, NANO, and Smart Systems, Proc. of ICMENTS2003, Banff, Ab, Canada, July 2003.

[P8] M. Daneshmand, R. R. Mansour, "RF MEMS Mulit-Port Switches", Third Canadian Workshop on MEMS, Ottawa, ON., Canada, August 2003.

[P9] M. Daneshmand and R.R.Mansour, "An Integrated SP3T RF MEMS Switch", Proc. of ANTEM 2002, Montreal, Qc, Canada, August 2002.

References

[1] K. S. Lazaris-Brunner, G. Beauchamp, B. Tailor, "The Multi Media Pre Processor, A Saw Based Analog Processing Technique to Optimize Digital Demultiplexing Requirements in Wideband Digital OBP Satellites" *Comdev catalogue*. Comdev Space group, Cambridge, Ontario, Canada

[2] M. Daneshmand, and R.R. Mansour, "Fabrication and Modeling of an SP3T RF MEMS Switch", 2003 *IEEE Antennas and Propagation Symposium and URSI Radio Science Meeting Dig*. Vol. 1 pp. 391-394, 2003.

[3] Advance Switch Technology, "*http://www.astswitch.com*", Kingston, Ontario, Canada.

[4] DowKey Microwave Corporation, "*http://www.dowkey.com/*".

[5] F. X. Pitschi, G. Spinner, "Coaxial RF Switch Matrix", *United States Patent*, Patent No: 4829271, May 9,1989.

[6] M. Hosogai, S. Kojima, H. Yokemura, R. Takada, H. Otaguro, T. Ashida, and T. Abe, "Matrix Switch Board Used to Connect/Disconnect Switching System and Subscriber-Side Line", *United States Patent*, Patent No.6116912, Sep.12, 2000.

[7] V. K. Varadan, K. J. Vinoy, K. A. Jose, "RF MEMS and Their Applications", *John Wiley & Sons*, 2003.

[8] A. Romano, "Apparatus and Method for Enhancing the Isolation of an MMIC Cross-Point Switch", *United States Patent*, Jul.24, 2001.

[9] B. Dov Geller, "Integrated RF MxN Switch Matrix", *United States Patent*, Patent No.6346744 , Feb. 12 2002.

[10] G. M. Rebeiz, and J. B. Muldavin, "RF MEMS Switches and Switch Circuits", *IEEE Microwave Magazine*, Dec. 2001.

[11] J. J. Yao, "Micro Electromecahnical RF Switch", *United States Patent*, Patent Assignee: Rockwell International Corporation, Patent No.5578976, Nov.1996.

[12] M. Duelli, D. M. Friedrich, and B. P. Hichwa, "Method of Actuating MEMS Switches", *United States Patents*, Patent No.6388359, May 14, 2002.

[13] L.E. Larson, R.H. Hachett, R.F. Lohr, "Microactuators for GaAs-Based Microwave Integrated Circuits", *Digest of technical papers; Solid State Sensors and Actuators*, P.743-746, June 1991.

[14] L. P. B. Katehi , F. Harvey, and E. Brown, "MEMS and Si Micromachined Circuits for High-Frequency Applications", *IEEE Transactions on Microwave Theory and Techniques*, Vol. 50, No.3, March 2002.

[15] S. Duffy, C. Bozler, S. Rabe, J. Knecht, L. Travis, P. Wyatt, C. Keast, and M. Gouker, "MEMS Microswitches for Reconfigurable Microwave Circuitry", *IEEE Microwave and Wireless Components Letters*, Vol.11, No.11, March 2001.

[16] E. R. Brown, "RF-MEMS Switches for Reconfigurable Integrated Circuits", *IEEE Transactions on Microwave Theory and Techniques*, Vol. 46, No.11, Nov. 1998.

[17] J. J. Yao, "RF MEMS from a device perspective", *Journal of Micromech. Microeng.*, printed in UK, p.R6-R38, April 2000.

[18] X. Q Sun, "Folded Spring Based Micro Electromechanical (MEM) RF Switch", *United States Patents*, Motorola Incorporation, Patent No.6307452, October 2001.

[19] R. E. Mihailovich, M. Kim, J. B. Hacker, E. A. Sovero, F. Studer, J. A. Higgins and J.F. DeNatale, " MEM Relay for Reconfigurable RF Circuits", *IEEE Microwave and Wireless Components Letters*, Vol.11, No.2, Feb. 2001.

[20] J. B .Muldavin, and G. Rebeiz "All-Metal High –Isolation Series and Series Shunt MEMS Switches", *IEEE Microwave and Wireless Components Letters*, Vol.11, No.9, Sep.2001.

[21] V. Milanovic, M. Maharbiz, and K. S. J. Pister, "Batch Transfer Integration of RF Microrelay", *IEEE Microwave and Guided Wave Letters*, Vol.10, No.8, Aug. 2000.

[22] G. L. Tan, R. E. Mihailovich, J. B. Hacker, J. F. DeNatale, and G. M. Rebeiz, "Low-Loss 2-and 4-bit TTD MEMS Phase Shifters Based on SP4T Switches", *IEEE Transactions on Microwave Theory and Techniques*, Vol. 51, No.1, January 2003.

[23] D. Peroulis, S. Pacheco, K. Sarabandi, and L .P. B, Katehi, "MEMS Devices for High Isolation Switching and Tunable Filtering", *IEEE MTT-S Digest*, p.1217-1220, 2000.

[24] J.B. Muldavin, G. M. Rebeiz, "Inline Capacitive and DC Contact MEMS Shunt Switches", *IEEE and Wireless Components Letters*, Vol.11, No.8, August 2001.

[25] J. B. Muldavin, and G. M. Rebeiz, "High Isolation Inductively-Tuned X Band MEMS Shunt switches", *IEEE MTT-S Digest*, p.169-172, 2000.

[26] J. Rizk, G. L. Tan, J. B. Muldavin, and G. M. Rebeiz, "High-Isolation W-Band MEMS Switches", *IEEE Microwave and Wireless Components Letters*, Vol.11, N.1, January 2001.

[27] D. Girbau, A. Lazaro, L. Pradel, "RF MEMS Switches Based on the Buckle-Beam Thermal Actuator", *33rd European Microwave Conference*, pp. 651-654, 2003.

[28] L. Qu, K. Udeshi, J. Par, and Y. B. Gianchandani, "A Bi-Stable Electro-Thermal RF Switch for High Power Applications", IEEE International Conference on MEMS, pp. 797-800, 2004.

[29] P. Pons, K Grenier, D. Dubuc, A. Boukabache, F. Flourens, B. Ducarouge, S. Melle, H. Aubert, L. Bary, J. Graffeuil, and R. Plana "MEMS Technologies for Milimeterwave Space Applications", *IMS 2004 Confernece, Workshop on Reconfigurable MEMS for Optimum RF/Microwave Transceivers*, Jun. 2004.

[30] Y. Kwon, Y. K. Kim, J. H. Park, S. Lee, H. T. Kim, "Reconfigurable Front-End Passive Components For High Frequency Applications", *Workshop on*

Reconfigurable MEMS for Optimum RF/Microwave Transceivers, IMS 2004 Conference, Jun. 2004.

[31] C. D. Nordquist, "RF MEMS For Reconfigurable Filters at Sandia National Laboratories", *Workshopt on MEMS, BAW and micromachined Filters, IMS 2004 Conference*, June 2004.

[32] B. Yassini**,** S. Choi, A. Zybura, M. Yu, R. E. Mihailovich and Jeffrey. F. DeNatale "A Novel MEMS LTCC Switch Matrix*", IEEE MTT-S Digest*, p.721-724, 2004.

[33] C. Goldsmith, J. Ehmke, A. Malczewski, B. Pillane, S. Eshelman, A. Yao, J. Brank, and M. Eberly, "Lifetime Characterization of Capacitive RF MEMS Switches", *IEEE MTT-S Digest*, p.227-230, 2001.

[34] K. J. Herrick, J. G. Yook, L. P. B. Katehi, "Microtechnology in the Development of Three Dimensional Circuits", *IEEE Transactions on Microwave Theory and Techniques*, Vol.46, No.11, p.1832-1844, 1998.

[35] J. G. Kim, E. T. Kee, D. H. Kim, J. H. Lee, S. Y. Lee, H. S. Kim, J. S. Park, and C.Y.Cheon, "Analysis of coupling Characteristics between Transmission Lines with a Buried Meshed Ground in LTCC-MCMs*", IEEE MTT-S Digest*, p.825-828, 2002.

[36] A. Margomenos, S. Valas, M.I.Herman, L.P.B.Katehi, "Isolation in Three Dimensional Integrated Circuits", *IEEE MTT-S Digest*, p.1875-1878, 2000.

[37] T. Ishikawa, E. Yamashita, "Characterization of Buried Microstrip Lines for Constructing High-Density Microwave integrated Circuits", *IEEE Transactions on Microwave Theory and Techniques*, Vol.44, No.6, p.840-847, June 1996.

[38] R. N. Simons, K. Goverdhanam, and L. P. B. Katehi, "Novel Low Loss Wide-Band Multi-Port integrated Circuit technology For RF/Microwave Applications", *Digest of Silicon Monolithic integrated Circuits in RF Systems*, p.60-63, 2001.

[39] A. Margomenos, K. J. Herrick, M. I. Herman, S. Valas, and L. P. B. Katehi, "Insolation in Three-Dimensional Integrated Circuits", *IEEE Transactions on*

Microwave and Techniques, Vol. 51, No.1, January 2003.

[40] G. E. Ponchak, E. Tentzeris, "Development of finite ground coplanar waveguide90 degree cross over junctions with low coupling conductor" *2000 IEEE MTT-S Digest*, p. 386-392, June 2000.

[41] R. Abhari, G. V. Eleftheriades, and D. V. Deventer-Perkins, "Physics-Based CAD Models for the Analysis of Vias in Parallel-Plate Environments", *IEEE Transactions on Microwave Theory and Techniques,* Vol.49, No.10, October 2001.

[42] A. Margomenos, D. Peroulis, J.P. Becker, and L. P. B. Katehi, "Silicon Micromachined Interconnects for On-Wafer Packaging of MEMS Devices", *Digest of Silicon Micromachined Interconnects for On-Wafer Packaging of MEMS Devices*, p.33-36, 2001.

[43] N. Huynh, and W. Heinrich, "Optimized Flipchip Interconnect For 38GHz-Thin Film Microstrip Multichip Modules*", IEEE MTT-S Digest*, p.69-72, 2000.

[44] W. Heinrich, A. Jentzsch, G. Baumann, "Millimeterwave Characteristics of Flip-Chip Interconnects for Multi-Chip Modules", *IEEE MTT-S Digest,* p.1083-1086, 1998.

[45] H.S. Hinton, "An Introduction to Photonic Switching Fabrics", *Plenum Press*, New York, 1993.

[46] F. T. Assal, J. V. Evans, C. E. Mahle, A. I. Zaghloul, R. K. Gupta, "Switch Matrix Including both B Switching Elements and Crossbar Switch Matrices", *United States Patent*, Patent No.5220320, June1993.

[47] A. Jentzsch, and W. Heinrich, "Optimization of Flip-Chip Interconnects for Millimeter-Wave Frequencies", *IEEE MTT-S Digest*, p.637-640, 1999.

[48] D. A. Koester, R. Mahadevan, B. Hardy, and K. W. Markus, "PolyMUMPs Design Handbook", *Cronos Integrated Microsystems*, A JDS Uniphase Company, 2000.

[49] D. Peroulis, S. P. Pacheco, K. Sarabandi, and L. P. B. Katehi, "Electromechanical Considerations in Developing Low-Voltage RF MEMS Switches", *IEEE Transactions on Microwave Theory and Techniques*, Vol.51, No.1, January 2003.

[50] S. D. Senturia, "Micro-system Design", *Kluwer Academic Publisher*, Massachusetts Institute of Technology, Boston, 2001.

[51] N. H. Huynh, W. Heinrich, K. Hirche, W. Scholz, M. Warth, and W. Ehrlinger, "Optimized Flip-Chip Interconnect for 38GHz, Thin-Film Microstrip Multichip Modules", *IEEE MTT-S Digest*, p.69-72, 2000.

[52] R. Cragun, L. L. Howell, "A Constrained Thermal Expansion Micro-Actuator", *DSC Micro-Electro Mechanical Systems (MEMS) ASME*, Vol. 66 p.365-371, 1998.

[53] A. Cowen, B. Dudley, E. Hill, M. Walters, R. Wood, S. Johnson, H. Wynads, "Metal MUMPs Design Handbook", *Cronos Integrated Microsystems*, A JDS Uniphase Company, 2002.

[54] A. Hammoud, S. Gerber, R. L. Patterson, T. L .MacDonald, "Performance f Surface-Mount Ceramic and Solid Tantalum Capacitors for Cryogenic Applications", *IEEE Conference on Electrical Insulation and Dielectric Phenomena*, Annual report, p. 572-576, Vol. 2, 1998.

[55] N. D. Mankame, and G. K. Ananthasuresh, "Comprehensive thermal modeling and characterization of an electro-thermal-compliant micro-actuator", *J. Micromech. Microeng. 11*, p. 452-462, 2001.

[56] F. P. Incropera, D. P. DeWitt, "Fundamentals of Heat and Mass Transfer", *Jogn Wiley & Sons*, 1985.

[57] G. M. Rebeiz, "RF MEMS, Theory, Design, and Technology", *Wiley Interscience*, John Wiley and Sons, 2003.

[58] J. Robinson, D. K. Paul,J.Bird, D. Dawson, T. Brown, D. Spencer, D. Prime, "A milimeteric car radar front end for automotive cruise control", *Automotive Radar and Navigation Techniques*, IEE colloquium on 9 Feb 1998.

[59] K. Y. Lin, Y. J. Wang, D. C. Niu, and H. Wang, "Millimeter-Wave MMIC Single-Pole-Double-Throw passive HEMT Switches Using Impedance-Transformation Networks", *IEEE Transactions on Microwave and Techniques*, Vol.51,No.4, April 2003.

[60] http://www.millitech.com, "Millitech; Millimeter-Wave Technology & Solutions", Millitech Incorporation, Northampton, MA.

[61] M. Daneshmand, R. R . Mansour, N. Sarkar, "RF MEMS Waveguide Switch", *2004 IEEE MTT-S Int. Microwave Symp. Dig*. Jun. 2004.M.

[62] M. Daneshmand, R. R. Mansour, and N. Sarkar, "RF MEMS Waveguide Switch", *IEEE Transactions on Microwave Theory and Techniques*, Vol.52, issue 12, pp.2651-2657, Dec. 2004

[63] A. Geisberger, Jungen, N. Sarkar, M. Ellis, G. Skidmore, "Modeling Electro Thermal Plastic Deformation Self-Assembly", *Nanotech 2003 Conference*, vol.1 pp. 482-487, Feb. 2003

[64] J. Muldavin, R. Boisvert, C. Bozler, S. Rabe, and C. Keast, "Power Handling and Linearity of MEM Capcitive Series Switches" , *2003 IEEE MTT-S Int. Microwave Symp. Dig,* p.1915-1918, Jun. 2003.

[65] D. Peroulis, S. P. Pacheco, and L. P. B. Katehi, " RF MEMS Switches with Enhanced Power-Handling Capabilities", *IEEE Transactions on Microwave and Theory and Techniques*, Vol. 52, No. 1, p.59-68, 2004.

[66] N.E. McGruer, P.M. Zavracky, R. Morrison, S. Majumder, D.Potter, and M. Schirmer, "RF and current handling performance of electrostatically actuated microswitches", *in Sensors Exposition*, Sept. 1999.

[67] www.memscap.com, "Memscap, the power of a small world",

[68] www.Ansoft.com, High Frequency System Simulator (HFSS)

[69] M. Daneshmand, and R. R. Mansour, "Multi-port Waveguide Switches", IEEE IMS 2005, *IEEE MTT-S Int. Microwave Symp. Digest*, Long beach, CA, June 2005.

[70] M. Daneshmand, and R.R. Mansour, "Multi-port MEMS-Based Waveguide and Coaxial Switches", *IEEE Transactions on Microwave Theory and Techniques*, p.1-7 Nov. 2005.

[71] P. Blondy, A. Crunteanu, C. Champeaux, A. Catherinot, P.Tristant, O. Vendier, J. L. Cazaux, and L. Marchand, "Dielectric Less Capacitive MEMS Switches", *IEEE MTT-S Int. Microwave Symp. Dig*., p. 573-576, June 2004.

[72] Comdev Space group, "Beam Link™ ,… a COM DEV Technology", Cambridge, Ontario, Canada.

[73] B. Yassini**,** S. Choi, A. Zybura, M. Yu, R. E. Mihailovich and Jeffrey. F. DeNatale "A Novel MEMS LTCC Switch Matrix", *IEEE MTT-S Digest*, pp.721-724, 2004.

[74] M. Tsuji, H. Shigesawa, and A. A. Oliner, "New Interesting Leakage Behavior on Coplanar Waveguides of Finite and Infinite Widths", *IEEE Transcations on microwave Theory and Techniques*, Vol.39, No.12 , p.2130-2137, 1991.

[75] A. Margomenos, K. J. Herrick , M. I. Herman, S. Valas, and L. P. B. Katehi, "Isolation in Three-Dimensional Integrated circuits", *IEEE Transactions on Microwave Theory and Techniques*, Vol.51, No.1, January 2003.

[76] Sonnet Software, High Frequency Planar Structure Simulator, http://www.sonnetusa.com/support/index.asp, 1983-2003.

[77] High Frequency Structure Simulator (HFSS), Ansoft verstion 3.1.04, 2002.

[78] R. N Simons, R. Q. Lee, K. A. Shalkhauser, J. Owens, J. Demarco, J. Leen, and D. Sturzebecher, " Finite Width Coplanar Waveguide Patch Antenna with Vertical Fed Through Interconnect", *IEEE AP-S Int. Symposium and URSI Radio Science meeting Dig*. VOl.2, pp.1138-1341, 1996.

[79] M. Daneshmand, R. R. Mansour, P. Mousavi, S. Choi, B. Yassini, A. Zybura, and M. Yu, "A Novel Integrated Interconnect Network for RF Switch Matrix Applications", *2004 IEEE MTT-S Int. Microwave Symp*. Dig. Jun. 2004.

[80] K. J. Herrick, "W-Band Three-Dimensional Integrated Circuits Utilizing Silicon Micormachining", Ph.D dissertation, *University of Michigan*, 2000.

[81] H. S . Hinton, "An Introduction to Photonic Switching Fabrics", *Plenum Press*, 1993.

[82] H. Y. Lee, F. K. Hwang, and J. D. Carpinelli, "A New Decomposition Algorithm for Rearrangeable Clos Interconnection Networks", *IEEE Transactions on Communications,* Vol.44, No.11, 1996.

[83] M. Daneshmand, R. R. Mansour, P. Mousavi, S. Choi, B. Yassini, A. Zybura, and M. Yu, "Integrated Interconnect Networks for RF Switch Matrix Applications", *IEEE Transactions on Microwave Theory and Techniques*, January 2005.

[84] Triquint Semiconductor Incorporation, http://www.triquint.com, Oregon, US.

[85] M. Daneshmand, R. R. Mansour, "An Integrated SP3T RF MEMS Switch", Proc. of ANTEM 2002, Montreal, Qb, Canada, August 2002.

[86] R. W. Jackson and D. W. Matolak, "Surface to surface transition via electromagnetic coupling of coplanar waveguide", *IEEE Transactions on Microwave Theory and Technique*, Vol. 35, pp. 1027-1032, November. 1987.

[87] J. P. Raskin, G. Gauthier, L. P. Katehi, and G. M. Rebeiz, "W-Band Single-Layer Vertical Transition", *IEEE Transactions on Microwave Theory and Techniques*, Vol. 48, No. 1, pp.161-164, January 2000.

[88] J .J. Yao, and M. F. Chang, "A surface micromachined miniature switch for telecommunications applications with signal frequencies from DC up to 4 GHz", *The 8th international conference on solid state sensors and actuators*, 1995.

[89] E. P. Popov, "Engineering Mechanics of Solids", *Printice_Hall Inc*., University of California-Berekely, in collaboration with T.A.Bala, 1999.

[90] Mojgan Daneshmand, " 7 Mask Process", *Center For Integrated RF Engineering Lab*, University of Waterloo, Waterloo, Ontario, Canada, 2005.

[91] Micro and Nanotechnology Commercialization Education Foundation, MANDEF 2002 Roadmap, Mancef 2004 Roadmap.